# THE CORRELATION OF MICROSTRUCTURE WITH STRENGTH AND FRACTURE TOUGHNESS IN PEARLITIC RAIL STEELS

FRANK PAUL LEMAMA KAVISHE
*BSc(Eng), MSc, DIC, MIET, AMIM*

A thesis submitted for the Degree of
DOCTOR OF PHILOSOPHY
of the University of London

Imperial College of Science and Technology
Department of Metallurgy and Materials Science
Prince Consort Road
London SW7 2BP

JANUARY, 1986

*TO MY DARLING WIFE DEVOTA*

*AND OUR CHILDREN*

# A B S T R A C T

The influence of prior austenite grain size $\gamma$ and pearlite interlamellar spacing $S_t$ on the strength and fracture toughness of a eutectoid and hypoeutectoid rail steel has been investigated and the micromechanisms of cleavage fracture in pearlite identified. Specimens were machined from rail sections and heat treated to produce a wide variation in austenite grain size and pearlite interlamellar spacing. Mechanical properties measured included tensile strength and ductility, cleavage fracture stress and plane strain fracture toughness $K_{IC}$. Most tests were performed at -80 and -100 °C, but others were performed in the range -25 to -196 °C.

The proof stress $\sigma_{0.2}$, ultimate tensile stress $\sigma_u$ and the cleavage fracture stress $\sigma_f$ increase with decreasing interlamellar spacing. The proof stress is related to the ferrite mean free distance by a Hall-Petch equation. No simple relationship is observed between $\gamma$ grain size and the strength parameters. The tensile ductility $\delta$ decreases progressively with increasing $\gamma$ grain size. The ductility is interpreted as the strain necessary to develop an internal microcrack which causes quasi-brittle fracture in the tensile test. The size of the microcrack is related to the pearlite nodule size, which in turn is related to $\gamma$ grain size.

In lower strength pearlite, associated with coarse interlamellar spacings and high test temperatures, $\sigma_f$ increases with decreasing test temperature in the same manner as $\sigma_{0.2}$. Metallographic and fractographic evidence suggests that under these conditions cleavage fracture is nucleation-controlled and involves the nucleation of a microcrack by shear-stress-controlled fibrous cracking of the pearlite. In higher strength pearlite, associated with fine interlamellar spacings or low test temperatures, $\sigma_f$ is temperature independent. For this condition cleavage fracture is interpreted as being propagation-controlled with crack nucleation occurring as a result of fibre loading of the cementite lamellae.

In the eutectoid steel, $K_{IC}$ first decreases with decreasing interlamellar spacing $S_t$ and then increases for the finest spacing . This is attributed to the change in the micromechanism of cleavage fracture. The tensile

ductility shows an opposite effect to that of $K_{IC}$. The hypoeutectoid steel shows similar behaviour to that of the eutectoid steel for volume fractions of proeutectoid ferrite less than about 10 %. In both steels, changes in austenitising conditions have little influence on $K_{IC}$. This is attributed to the fact that the process zone in a sharply notched specimen is much smaller than the prior austenite grains, and as such the grain boundaries are unlikely to influence the fracture process.

# ACKNOWLEDGEMENTS

I am greatly indebted to my Supervisor, Dr. T. J. Baker, for his tireless guidance and critical comments when undertaking this research. I acknowledge the financial support of the Swiss Development Cooperation, Berne, Switzerland, who paid my allowances and some of my college fees. I must also mention the British Overseas Research Students Committee (ORS Awards) for paying the remainder of my college fees.

My very sincere thanks are due to the British Steel Corporation who kindly donated the rail steels, and to Dr. R. R. Preston of BSC Swinden laboratories for his interest in the project. Many thanks are also due to Dr. D. R. F. West, (Imperial College) and Dr. F. B. Pickering, (Sheffield Polytechnic), for their very useful discussions. My thanks are also due to the Vice Chancellor of the University of Dar es Salaam in Tanzania for granting me study leave to undertake PhD research, and to Professor D. W. Pashley, FRS, for providing the research facilities at Imperial College, London.

Lastly, but not least, I wish to acknowledge the cooperation and help which I received from the Technical and Administrative Staff of the Department of Metallurgy and Materials Science, Imperial College, and from fellow research students.

FPLK

# C O N T E N T S


ABSTRACT 3

ACKNOWLEDGEMENTS 5

CONTENTS 6

LIST OF SYMBOLS 8

LIST OF TABLES 10

LIST OF FIGURES 11

1. INTRODUCTION 17

2. PEARLITIC STEELS 19

2.1 Pearlitic steels for rails 19

2.2 The nature of pearlite 20

2.3 Pearlite interlamellar spacing 23

2.4 The yield strength of pearlitic steels 26

2.5 The tensile deformation of pearlitic steels 30

2.6 The toughness of pearlitic steels 33

2.7 Ferritic/pearlitic steels for rails 35

2.8 Objectives of the present research 36

3. CLEAVAGE FRACTURE IN STEELS 39

3.1 Modes of fracture in metals 39

3.2 Cleavage fracture in mild steels 40

3.3 Cleavage fracture in bainitic steels 45

3.4 Cleavage fracture in a martensitic steel 48

3.5 Factors affecting $\sigma_f$ in low carbon mild steels 50

3.6 Cleavage fracture in fully pearlitic steels 52

3.7 Aspects of cleavage fracture covered by the present research 55

4. EXPERIMENTAL TECHNIQUES 55

4.1 Materials used 55

4.2 Heat treatment 55

4.3 Plane strain fracture toughness 56

4.3.1 Specifications for the test 56

4.3.2 Procedures used to determined $K_{IC}$ 59

4.4 Cleavage fracture stress 59

4.5 Proof stress and ultimate tensile stress 60

4.6 Quantitative metallography 63

4.6.1 Prior austenite grain size 63

4.6.2 Pearlite nodule size and colony size 66

4.6.3 Pearlite interlamellar spacing and ferrite mfd 66

4.7 Fractography 67

**5. RESULTS FROM THE EUTECTOID STEEL** 68

5.1 The microstructure 68

5.2 Mechanical properties 76

5.3 The effect of austenitising conditions on mechanical properties 76

5.4 The effect of pearlite interlamellar spacing on mechanical properties 83

5.5 The effect of test temperature on $\sigma_{0.2}$ and $\sigma_f$ 83

5.6 Fractography 90

**6. RESULTS FROM THE HYPOEUTECTOID STEEL** 98

6.1 The microstructure 98

6.2 Mechanical properties 104

6.3 The effect of austenitising conditions on mechanical properties 104

6.4 The effect of pearlite interlamellar spacing on mechanical properties 108

6.5 The effect of test temperature on $\sigma_{0.2}$ and $\sigma_f$ 111

**7. DISCUSSION OF RESULTS** 114

**7.1 THE EUTECTOID STEEL** 114

7.1.1 The microstructural parameters 114

7.1.2 Proof stress and ultimate tensile stress 116

7.1.3 The cleavage fracture stress $\sigma_f$ 123

7.1.4 The micromechanisms of cleavage fracture in pearlite 125

7.1.5 Plane strain fracture toughness $K_{IC}$ 131

7.1.6 Tensile ductility 133

**7.2 THE HYPOEUTECTOID STEEL** 137

7.2.1 The microstructural parameters 137

7.2.2 Proof stress and ultimate tensile stress 137

7.2.3 The cleavage fracture stress $\sigma_f$ 141

7.2.4 Plane strain fracture toughness and tensile ductility 143

**8. CONCLUSIONS AND RECOMMENDATIONS** 147

**REFERENCES** 150

**APPENDIX 1** 155

**APPENDIX 2** 156

# LIST OF SYMBOLS

| | |
|---|---|
| $a$ | crack length |
| $B$ | specimen thickness |
| $c$ | cementite |
| $C$ | pearlite colony size |
| $C_o$ | carbide particle size |
| $C_s$ | carbon content of steel |
| $d$ | grain size |
| $D$ | distance between active slip planes |
| $D_p$ | pearlite dilution factor |
| $E$ | Young's modulus |
| $F$ | cleavage facet size |
| $G$ | shear modulus |
| $k_y$ | Hall-Petch constant |
| $K$ | stress intensity factor |
| $K_{IC}$ | plane strain fracture toughness |
| $K_{ID}$ | dynamic fracture toughness |
| $K_Q$ | provisional value of $K_{IC}$ |
| $l$ | length |
| $L$ | half loading span of specimen |
| $N$ | pearlite nodule size |
| $p$ | pearlite |
| $P$ | load |
| $P_Q$ | load to calculated $K_Q$ |
| $r$ | radius |
| $r_p$ | plastic zone size |
| $R$ | stress intensification factor |
| $S_a$ | apparent interlamellar spacing |
| $S_o$ | minimum interlamellar spacing |
| $S_r$ | random interlamellar spacing |
| $S_t$ | true interlamellar spacing |
| $t$ | thickness of cementite lamellae |
| $U$ | energy |
| $V_\alpha$ | volume fraction of proeutectoid ferrite |
| $V_p$ | volume fraction of pearlite |
| $W$ | specimen width |
| $X$ | characteristic distance for fracture |
| $Y$ | compliance for a 4-point bend geometry |

| | |
|---|---|
| $Y_1$ | compliance for a 3-point bend geometry |
| $\alpha$ | ferrite |
| $\gamma$ | austenite and austenite grain size |
| $\delta$ | % elongation at fracture (tensile ductility) |
| $\Delta T$ | degree of undercooling |
| $\epsilon$ | elastic strain |
| $\epsilon_f$ | strain at fracture |
| $\epsilon_p$ | plastic strain |
| $\epsilon_y$ | yield strain |
| $\lambda$ | ferrite mean free distance (mfd) in pearlite |
| $\lambda_\alpha$ | ferrite mfd in the hypoeutectoid steel |
| $\sigma_{0.2}$ | 0.2% proof stress |
| $\sigma_1$ | principal stress |
| $\sigma_f$ | cleavage fracture stress |
| $\sigma_F$ | fibre loading stress |
| $\sigma_i$ | lattice friction stress |
| $\sigma_o$ | flow stress |
| $\sigma_u$ | ultimate tensile stress |
| $\sigma_y$ | yield stress |
| $\tau$ | shear stress |
| $\tau_i$ | lattice friction shear stress |
| $\nu$ | Poisson's ratio |

# LIST OF TABLES


Table 2.1 Specifications for commercial rail steels in the UK 19

Table 2.2 AREA specifications for rail steels 19

Table 4.1 Chemical composition of rail steels 55

Table 4.2 Heat treatment sequences 57

Table 5.1 Microstructural parameters measured from the eutectoid steel 75

Table 5.2 Mechanical properties of the eutectoid steel determined at −80 °C 77

Table 5.3 The variations of $\sigma_f$ and $\sigma_{0.2}$ with test temperature for coarse (C) and fine (F) pearlite 87

Table 6.1 Microstructural parameters measured from the hypoeutectoid steel 103

Table 6.2 Mechanical properties of the hypoeutectoid steel determined at −100 °C 105

Table 6.3 The variations of $\sigma_f$ and $\sigma_{0.2}$ with test temperature for coarse pearlite in the hypoeutectoid steel. 112

Table 7.1 Calculated values of the plastic zone size $r_p$ and the characteristic distance for fracture X in the eutectoid steel 134

Table 7.2 Calculated values of the critical crack size (2a) for cleavage fracture in the tensile specimens (eutectoid steel) 136

Table 7.3 Calculated values of the plastic zone size $r_p$ and the characteristic distance for fracture X in the hypoeutectoid steel. 146

# LIST OF FIGURES


| | | |
|---|---|---|
| Figure 2.1 | Nucleation and growth of pearlite colonies after Mehl and Hagel (1956). | 21 |
| Figure 2.2 | Schematic diagram of a pearlite colony formed on an austenite grain boundary and growing hemispherically into the neighbouring austenite grain $\gamma_2$ (Honeycombe 1980). | 21 |
| Figure 2.3 | The classification of spacings in a geometrically ideal lamellar structure after Underwood (1970) | 25 |
| Figure 2.4 | The probable distribution of true spacings in a commercial eutectoid steel after Pellisier et al (1942). | 25 |
| Figure 2.5 | The dependence of the minimum interlamellar spacing of pearlite on transformation temperature (Ridley 1984). | 27 |
| Figure 2.6a | The effect of cooling rate on the minimum interlamellar spacing of pearlite after Marder and Bramfitt (1975). | 27 |
| Figure 2.6b | The effect of undercooling ($\Delta T$) on the minimum interlamellar spacing of pearlite after Marder and Bramfitt (1975). | 28 |
| Figure 2.7 | The dependence of the lower yield stress of mild steel on grain size (Honeycombe 1981). | 28 |
| Figure 2.8 | The effect of carbon content (pearlite volume fraction) on the impact transition temperature and shelf energy value of normalized steels (Pickering, 1978). | 34 |
| Figure 2.9 | The effect of pearlite volume fraction on contributions of various strengthening mechanisms on the yield stress of ferrite-pearlite steels (Pickering, 1978). | 34 |
| Figure 2.10 | The effect of minimum interlamellar spacing $S_o$ and thickness of cementite lamellae t on contribution to impact transition temperature (Pickering, 1978). | 34 |

Figure 2.11 Charpy transition temperature as a function of the prior austenite grain size for rail steels after Bouse et al (1978). 38

Figure 2.12 The effect of interlamellar spacing on the yield strength of a 0.6% and 0.8% C steel after Gladman et al (1972). 38

Figure 2.13 The effect of interlamellar spacing on the tensile strength of a 0.6% C steel after Gladman et al (1972). 38

Figure 3.1 The grain size dependence of yield stress ($\sigma_y$) and cleavage fracture stress ($\sigma_f$) in mild steel at -196 °C. 41

Figure 3.2 Cleavage fracture nucleation ahead of a dislocation pile up according to the Zener/Strohl model. 41

Figure 3.3 Model for cleavage fracture nucleation in a bcc metal after Cottrell. 43

Figure 3.4 Smith's model for cleavage fracture in mild steels. 43

Figure 3.5 Critical fracture stress $\sigma_f$ as a function of size of microstructural units separated by high-angle boundaries in steels (Brozzo et al, 1977). 47

Figure 3.6 Correlation between cleavage fracture stress $\sigma_f$ and yield stress $\sigma_y$ in a Mn-Mo-Ni bainitic steel after Curry (1984). 47

Figure 3.7 The prior austenite grain size ($d\gamma$) dependence of proof stress in a 0.1% C, Ni-Cr-Mo steel in martensitic/bainitic condition after Tomita and Ikabayashi (1985). 49

Figure 3.8 The variation of proof stress, ultimate tensile stress and cleavage fracture stress with temperature in A 533 B pressure vessel steel after Bowen and Knott (1984). 49

Figure 3.9 Variation in cleavage fracture stress $\sigma_f$ with ferrite grain size d (Curry and Knott,1976) 51

Figure 3.10 Variation in cleavage fracture stress $\sigma_f$ with ferrite grain size d (several workers) from Knott (1976) 51

| | | |
|---|---|---|
| Figure 3.11 | Variation in cleavage fracture stress $\sigma_f$ with degree of prestrain for aged and unaged materials after Sandstrom et al (1981). | 53 |
| Figure 3.12 | Shear cracking of pearlite after Miller and Smith (1970). | 53 |
| Figure 4.1 | Dimensions of the $K_{IC}$ specimen. | 61 |
| Figure 4.2a | Dimensions of the single notched bend specimen. | 61 |
| Figure 4.2b | Dimensions of the double notched bend specimen. | 61 |
| Figure 4.3 | The variation of the stress intensification R with applied load in a 45° blunt notched specimen (Griffiths and Owen, 1971). | 62 |
| Figure 4.4 | The variation of the maximum principal stress below the notch root at various loads (Griffiths and Owen, 1971). | 62 |
| Figure 4.5a | Prior austenite grain boundaries in specimens of the eutectoid steel austenitized for 1 hour at 900 °C and 1200 °C respectively. | 64 |
| Figure 4.5b | Prior austenite grain boundaries outlined by proeutectoid ferrite in the hypoeutectoid steel. | 65 |
| Figure 5.1 | Different stages in the transformation of pearlite. | 69 |
| Figure 5.2 | Three impinging pearlite nodules in a specimen transformed in a fluidised bed at 510 °C after austenitizing for 1 hour at 1200 °C and 1000 °C respectively. | 70 |
| Figure 5.3a | The microstructure of the fully pearlite steel in the as received condition. | 71 |
| Figure 5.3b | The microstructure of specimens austenitized for 1 hour at 900 °C and 1200°C respectively and transformed in a fluidised bed at 510 °C. | 72 |
| Figure 5.4a | Specimens showing coarse and fine pearlitic microstructures. | 73 |
| Figure 5.4b | Proeutectoid ferrite along prior austenite grain boundaries in a specimen transformed at 650 °C, thus revealing austenite grains, pearlite colonies and pearlite nodules. | 74 |
| Figure 5.5a | The effect of prior austenite grain size $\gamma$ on the proof stress $\sigma_{0.2}$, ultimate tensile stress $\sigma_u$, and the cleavage fracture stress $\sigma_f$ for the isothermally transformed specimens (-80 °C) | 78 |

Figure 5.5b The effect of austenitizing temperature on the proof stress $\sigma_{0.2}$, ultimate tensile stress $\sigma_u$, and % elongation at fracture $\delta$ for the normalised specimens tested at room temperature. 79

Figure 5.6 The effect of prior austenate grain size $\gamma$ on the proof stress $\sigma_{0.2}$, ultimate tensile stress $\sigma_u$ and the cleavage fracture stress $\sigma_f$ in the fine grain regime. 80

Figure 5.7 The effect of prior austenite grain size $\gamma$ on the tensile ductility $\delta$ and the plane strain fracture toughness $K_{IC}$. 82

Figure 5.8 The effect of pearlite interlamellar spacing $S_t$ on the proof stress $\sigma_{0.2}$, ultimate tensile stress $\sigma_u$, and the cleavage fracture stress $\sigma_f$. 84

Figure 5.9 The effect of pearlite interlamellar spacing $S_t$ on the tensile ductility $\delta$, and the plane strain fracture toughness $K_{IC}$. 85

Figure 5.10 The influence of test temperature on the proof stress $\sigma_{0.2}$ and the cleavage fracture stress $\sigma_f$ in coarse pearlite. 86

Figure 5.11 The influence of test temperature on the proof stress $\sigma_{0.2}$ and the cleavage fracture stress $\sigma_f$ in fine pearlite. 88

Figure 5.12 The relationship between the proof stress $\sigma_{0.2}$, and the cleavage fracture stress $\sigma_f$ for a range of microstructures and testing conditions (eutectoid steel). 89

Figure 5.13 Transgranular cleavage fracture in the bend specimens. 91

Figure 5.14 Localised regions of fibrous fracture where cleavage facets were linked by shear 92

Figure 5.15 The pearlitic microstructure revealed on cleavage facets after etching in 2% nital. 93

Figure 5.16 Typical fracture path in nickel plated fracture surfaces (a & b) 94

Figure 5.17 A colony-sized non propagating microcrack seen below the notch root in the double notched bend specimens. 96

Figure 5.18 The microcrack shown in figure 5.17 is seen to be an array of microvoids at higher magnification. 97

Figure 6.1 The microstructure of the hypoeutectoid steel in the as received condition. 99

Figure 6.2 The microstructure of the specimen which was austenitized at 800 °C and transformed at 510 °C (hypoeutectoid). 100

Figure 6.3 The microstructure of the specimen which was austenitized at 1200 °C and transformed at 510 °C (hypoeutectoid). 100

Figure 6.4 The microstructures of the specimens which were austenitized at 900 °C and transformed at 510 and 650 °C respectively (hypoeutectoid). 101

Figure 6.5 The microstructure of the specimen which was furnace cooled from 900 °C (hypoeutectoid) 102

Figure 6.6 The effect of prior austenite grain size $\gamma$ on proof stress $\sigma_{0.2}$, ultimate tensile stress $\sigma_u$ and cleavage fracture stress $\sigma_f$ (hypoeutectoid steel). 106

Figure 6.7 The effect of prior austenite grain size $\gamma$ on tensile ductility $\delta$ and plane strain fracture toughness $K_{IC}$ (hypoeutectoid steel). 107

Figure 6.8 The effect of interlamellar spacing $S_t$ on proof stress $\sigma_{0.2}$, ultimate tensile stress $\sigma_u$ and cleavage fracture stress $\sigma_f$ (hypoeutectoid steel). 109

Figure 6.9 The effect of interlamellar spacing $S_t$ on tensile ductility $\delta$ and plane strain fracture toughness $K_{IC}$ (hypoeutectoid steel). 110

Figure 6.10 The temperature dependents of $\sigma_{0.2}$ and $\sigma_f$ in the hypoeutectoid steel with a coarse pearlitic microstructure. 113

Figure 7.1 The relationship between the prior austenite grain size and the pearlite nodule size in the fully pearlitic steel. 115

Figure 7.2 The dependents of the proof stress $\sigma_{0.2}$ on the inverse of true interlamellar spacing ($S_t^{-1}$) in the eutectoid steel. 118

| | | |
|---|---|---|
| Figure 7.3 | The dependence of the proof stress $\sigma 0.2$ of the eutectoid steel on the inverse square root of the mean free distance in pearlitic ferrite ($\lambda^{-1/2}$). | 118 |
| Figure 7.4 | The microstructure of specimen A1 which was austenitised for half an hour at 750 °C. | 121 |
| Figure 7.5 | Cooling curves of 25 mm cube specimens austenitised at different temperatures and then quenched into a fluidised bed at 640 °C. | 122 |
| Figure 7.6a | A fibrous fracture facet located below the tip of a fatigue crack in the eutectoid steel. | 127 |
| Figure 7.6b | The fibrous fracture facet in figure 7.6a reveals the carbide-nucleated microvoids at high magnifications. | 127 |
| Figure 7.7 | The variation of the stress intensification $R(\sigma_{yy}/\sigma_o)$ with the dimensionless quantity $X/(K/\sigma_o)^2$, where X is the characteristic distance for fracture. | 134 |
| Figure 7.8a | The dependence of the proof stress $\sigma_{0.2}$ on the inverse square root of the ferrite mean free distance ($\lambda_\alpha$) in the hypoeutectoid steel. | 139 |
| Figure 7.8b | The dependence of the proof stress $\sigma_{0.2}$ of the hypoeutectoid steel on the inverse square root of the mean free distance (mfd) in pearlitic ferrite. | 140 |
| Figure 7.9 | The dependence of the proof stress $\sigma_{0.2}$ of the eutectoid and hypoeutectoid steels on the mean free distance (mfd) in pearlitic ferrite. | 142 |
| Figure 7.10 | The relationship between the proof stress $\sigma_{0.2}$ and the cleavage fracture stress $\sigma_f$ of the hypoeutectoid steel for all test conditions. | 144 |
| Figure 7.11 | The relationship between the proof stress $\sigma_{0.2}$ and the cleavage fracture stress $\sigma_f$ in the eutectoid and hypoeutectoid steels. | 145 |

# 1. I N T R O D U C T I O N

Modern rail materials must cope with faster trains and higher axle loads than were encountered a few decades ago. These materials must therefore exhibit high hardness and yield strength to resist abrasion wear, plastic deformation and fatigue, and possess sufficient fracture toughness to resist brittle fracture. Due to their inherent wear resistance, pearlitic carbon - manganese steels have long been used to make rails. In Britain, these steels are manufactured mainly by the basic oxygen process combined with continuous casting. In the past, these steels used to be manufactured by either the acid Bessemer or the open hearth process. The steels were cast into ingots which were then hot rolled into rails. The present manufacturing process was adopted because it proved to be more economical and produces a higher output tonnage.

Rails for specific applications may require controlled cooling during manufacture, or alloying with chromium, molybdenum or vanadium to improve the mechanical properties. In certain cases, rail steels are also heat treated by induction hardening of the rail head, or by oil quenching and tempering of a whole rail. Standard carbon - manganese rail steels have a yield strength of about 500 $MN/m^2$ and a modulus of elasticity of about 207 x $10^3$ $MN/m^2$. Alloying elements may increase the yield strength by between 15 and 35 %, while heat treatment may raise the yield strength by more than 40 %.

The yield strength and ultimate tensile strength of pearlitic steels increase with decreasing pearlite interlamellar spacing. The toughness of these steels, as measured by the Charpy transition temperature or the dynamic fracture toughness appears to be controlled by the prior austenite grain size. Whilst the prior austenite grain size is controlled by the austenitizing temperature, in this case the final rolling temperature of the rail, the interlamellar spacing is determined by the austenite - to - pearlite transformation temperature. The latter is therefore controlled by the cooling rate of the finished rail.

Most rail failures are associated with either excessive wear or fatigue damage that leads to brittle fracture. The mode of fracture is normally transgranular cleavage. It is therefore necessary to have a clear

understanding of the micromechanisms of cleavage fracture in these steels in order to be able to design against premature failures. In mild steels, the micromechanisms of cleavage fracture appear to be well understood. In pearlitic steels the process of fracture has been studied previously, but no satisfactory micromechanisms for cleavage fracture have been proposed. The objective of this research has been to study the deformation behaviour of pearlite, and to identify the micromechanisms of cleavage fracture in pearlitic steels. By characterizing fracture in terms of the microscopic cleavage fracture stress and the plane strain fracture toughness, the microstructural variables that control cleavage will be elucidated. The roles of austenite grain size, pearlite interlamellar spacing, pearlite colony and nodule size, ferrite mean free distance and pearlite volume fraction in a eutectoid and a hypoeutectoid steel will be studied to identify the heat treatment conditions associated with optimum strength and fracture toughness.

# 2. P E A R L I T I C S T E E L S

## 2.1 Pearlitic steels for rails.

Most commercial rails are made from pearlitic steels. A study of rail steels should thus begin by exploring the behaviour and properties of pearlite in steels. In the UK, specifications for conventional rail steels are laid down in British standard BS 11 and in the International Union of Railways specifications UIC 860-0, table 2.1. Apart from these specifications, some rails are also made to the specifications of the American Railway Engineering Association (AREA), table 2.2.

**Table 2.1** Specifications for commercial rail steels in the UK (wt. %)

| Specification | C | Si | Mn | $S_{max}$ | $P_{max}$ |
|---|---|---|---|---|---|
| BS 11 | 0.50-0.60 | 0.05-0.35 | 0.95-1.25 | 0.06 | 0.06 |
| UIC 860-0 | 0.40-0.60 | 0.35 max | 0.80-1.20 | 0.05 | 0.05 |
| UIC 860-0A | 0.60-0.75 | 0.50 max | 0.80-1.30 | 0.05 | 0.05 |
| UIC 860-0B | 0.50-0.70 | 0.50 max | 1.30-1.70 | 0.05 | 0.05 |
| UIC 860-0C | 0.45-0.65 | 0.40 max | 1.70-2.10 | 0.03 | 0.03 |

**Table 2.2** AREA specifications for rail steels

| Constituents | Nominal weight lb/yd * | | | |
|---|---|---|---|---|
| wt. % | 70/80 | 81/90 | 91/120 | 121 & over |
| C | 0.55-0.68 | 0.64-0.77 | 0.67-0.80 | 0.69-0.82 |
| Si | 0.10-0.25 | 0.10-0.25 | 0.10-0.25 | 0.10-0.25 |
| Mn | 0.60-0.90 | 0.60-0.90 | 0.70-1.00 | 0.70-1.00 |
| $S_{max}$ | 0.05 | 0.05 | 0.05 | 0.05 |
| $P_{max}$ | 0.05 | 0.04 | 0.04 | 0.04 |

* 1 lb/yd = 0.5 kg/m

## 2.2 The nature of pearlite.

Steels of eutectoid composition have a fully pearlitic microstructure. Pearlite is made up of alternate layers of ferrite and cementite, the ratio of ferrite to cementite being about 87:13 by weight. In plain carbon steels cooled under equilibrium conditions, pearlite forms from austenite by a eutectoid reaction which occurs at a temperature of 723 °C and at a carbon content of about 0.8 wt-%. Just after the reaction, the ferrite contains 0.025 wt-% carbon and the cementite contains 6.7 wt-% carbon.

Pearlite has a lamellar structure, and forms by a process of nucleation and growth. The nucleation site may be a prior austenite grain boundary, proeutectoid grain boundary ferrite or cementite. Assuming the first nucleus is cementite, the development of a cementite platelet at a grain boundary may be pictured as in figure 2.1 after Mehl and Hagel (1956). Here the alternate nucleation and growth of cementite and ferrite is considered. The first cementite formed thickens so that the adjacent austenite becomes impoverished in carbon. The increasingly reduced carbon content of the adjacent austenite ultimately permits the nucleation of a layer of ferrite. The ferrite thickens, while both layers grow edgewise and as the adjacent austenite becomes impoverished in ferrite, another cementite layer nucleates. The process then proceeds in this manner and generates a lamellar structure. As the lamellae continue to grow sidewise, and extend edgewise, a new cementite lamella may nucleate and grow at a different orientation, thus creating a different pearlite colony. A colony is that portion of pearlite in which the cementite and ferrite lamellae are essentially parallel.

The development of differently oriented colonies in the microstructure results into a bigger reacted volume that is essentially spherical in shape. This is called a pearlite nodule. The nodule will continue to grow as its colonies develop, and it will eventually stop as it impinges upon another growing nodule. The orientation relations between cementite, ferrite and austenite have been studied extensively by Dippenaar and Honeycombe (1973). Within a pearlite nodule, the ferrite and cementite tend to show two distinct orientation relations. Colonies which happen to nucleate on prior austenite grain boundaries develop into a hemispherical aggregate, figure 2.2. In such cases the orientation

Figure 2.1 Nucleation and growth of pearlite colonies.

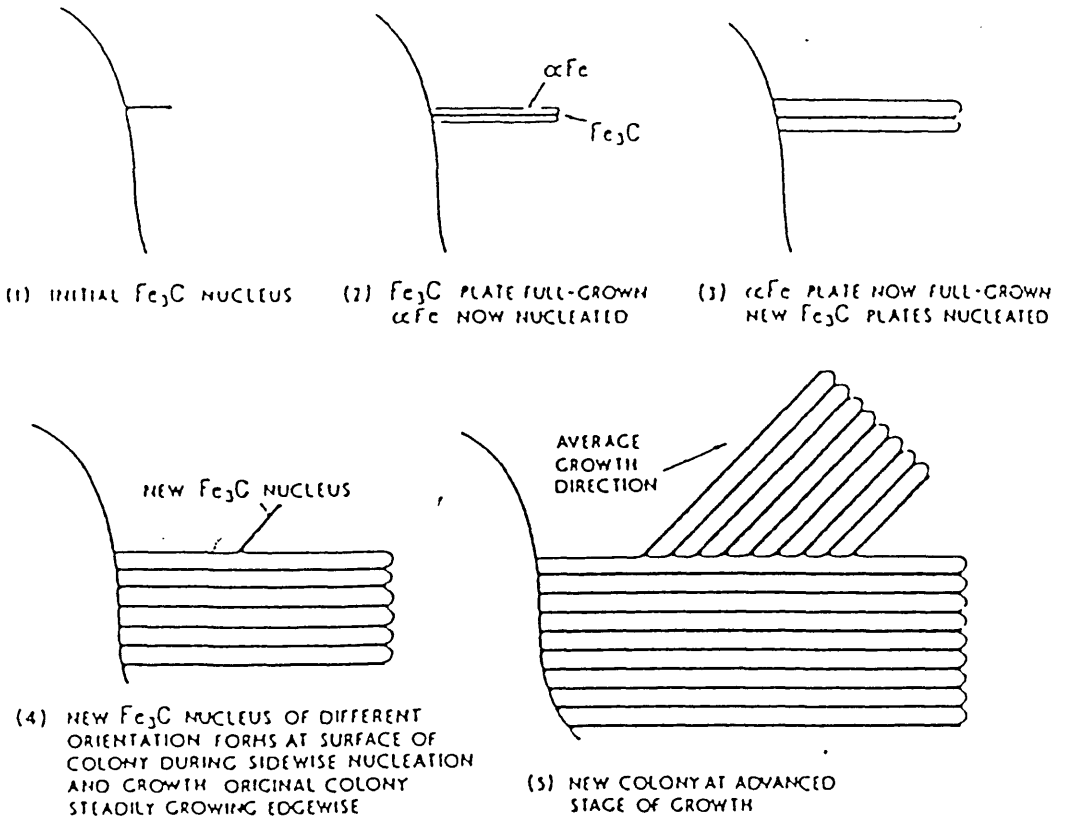
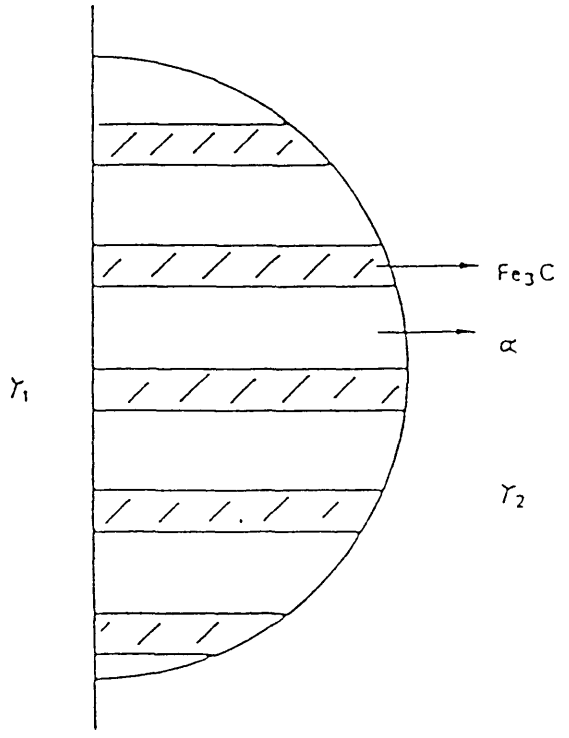



Figure 2.2 Schematic diagram of a pearlite colony formed on an austenite grain boundary and growing hemispherically into the neighbouring austenite grain $\gamma_2$.



relation between the ferrite ($\alpha$) and cementite (c) follows the Pitsch-Petch relation, so that:

$(100)_c$ are 2.6° from $[13\bar{1}]_\alpha$
$(010)_c$ are 2.6° from $[113]_\alpha$
$(001)_c$ are parallel to $(5\bar{2}\bar{1})_\alpha$

Further, the pearlitic ferrite tends to be related to the austenite grain $\gamma_1$ into which it is not growing, and has no consistent crystallographic relation with the austenite grain $\gamma_2$ into which it is growing. The observed relationship is close to the Kurdjumov-Sachs relationship, namely:

$\{111\}_\gamma$ are parallel to $\{110\}_\alpha$
$\langle 110\rangle_\gamma$ are parallel to $\langle 111\rangle_\alpha$.

As for ferrite, the pearlitic cementite is not related to the austenite grain $\gamma_2$. It is related to grain $\gamma_1$ into which it is not growing by the following relation:

$(100)_c$ are parallel to $[1\bar{1}1]_\gamma$
$(010)_c$ are parallel to $[110]_\gamma$
$(001)_c$ are parallel to $[\bar{1}12]_\gamma$

The fact that the ferrite and cementite of nodules showing the Pitsch-Petch relation are related to grain $\gamma_1$ means that the ferrite and cementite formed at the $\gamma_1/\gamma_2$ boundary (figure 2.2) are in direct contact with grain $\gamma_1$. The lamellae have a low-energy interface with $\gamma_1$ and display a random relation with grain $\gamma_2$ which results into a high-energy interface associated with high mobility. Thus the ferrite and cementite grow into grain $\gamma_2$ as a result of the high mobility interface. This observation is in good agreement with that of Smith (1953).

In those cases where pearlite colonies nucleate on grain boundary cementite, the ferrite and cementite show the Bagaryatski type relation whereby :

$(100)_c$ are parallel to $(0\bar{1}1)_\alpha$
$(010)_c$ are parallel to $(1\bar{1}\bar{1})_\alpha$
$(001)_c$ are parallel to $(211)_\alpha$

The pearlitic cementite in these colonies is continuous with the grain boundary cementite, and is related to the adjacent austenite grain $\gamma_1$, while the ferrite tends to be unrelated to both austenite grains $\gamma_1$ and $\gamma_2$. The ferrite is thus not in contact with any of the austenite grains at the time of its nucleation, and this confirms that nucleation did not take place on a clean prior austenite boundary.

The role of prior austenite grain boundaries on the growth of pearlite colonies is controversial. Rathenau and Baas (1954), observed that pearlite colonies can grow across prior austenite grain boundaries without the lamellae even changing direction. Further, Mehl and Hagel (1956), observed that pearlite nodules could cross prior austenite boundaries and consume a large number of austenite grains before impingement. Yet we know the prior austenite grain size controls the nucleation rate of pearlite, and would therefore control the pearlite nodule size for a given transformation temperature. Marder and Bramfitt (1976) obtained a linear relationship when they plotted nodule size against the logarithm of prior austenite grain size. It would seem therefore, that this question deserves a more thorough metallographic investigation.

## 2.3 Pearlite interlamellar spacing

The fineness of a lamellar structure is normally measured by the true interlamellar spacing, $S_t$. This is defined as the mean perpendicular distance across two consecutive lamellae. Apart from true spacing, we may also identify an apparent spacing and a random spacing. The apparent spacing, $S_a$ is a perpendicular distance across two consecutive lamellae measured on a plane of polish where the lamellae are not necessarily perpendicular to the plane of section. The apparent spacing will therefore vary from one colony to another, reflecting the angle at which the lamellae in the colony intersect the plane of polish. The random spacing $S_r$ is a mean distance across two successive lamellae taken from a test line applied randomly to the plane of polish. A schematic illustration of these spacings by Underwood (1970), is shown in figure 2.3.

Pearlite is sometimes characterized by the minimum observed interlamellar spacing, $S_o$. Pellisier et al (1942) observed that measurements of true interlamellar spacing in a given specimen

displayed a distribution of spacings about a mean value. The minimum observed true spacing in this distribution was about 1.7 times smaller than the mean true spacing, figure 2.4. Birkbeck and Wells (1968) have determined the ratio of mean spacing to minimum spacing in plain carbon and manganese-carbon steels and found it to vary from 1.1 to 1.6. The work of Asundi and West (1966) on a binary aluminium bronze of eutectoid composition suggested a ratio of mean true spacing to minimum spacing of about 2 to 2.5. Several other workers have obtained different ratios of mean true spacing to minimum spacing in both ferrous and non ferrous pearlites. It appears therefore that the factor which relates minimum spacings to mean true spacings is not constant, and may vary from one system to another, and with temperature within a given system (Ridley, 1984). Measurements of minimum spacing and mean true spacing can therefore not be compared directly when determined by different investigators. In the present investigation, the mean true interlamellar spacing has been used throughout to characterize the microstructure.

The pearlite interlamellar spacing is important because it controls the strength of pearlitic steels. The spacing is determined by the transformation temperature, the lower the temperature, the finer the spacing. Zener (1946) predicted that the reciprocal interlamellar spacing should vary linearly with undercooling, and that a logarithmic plot of spacing versus undercooling should give a straight line with a slope of -1. Data summarized by Ridley (1984) shows a linear relationship between reciprocal spacing and transformation temperature (figure 2.5). A regression analysis of this data leads to the following relationship between undercooling, $\Delta T$, and the minimum interlamellar spacing, $S_o$:

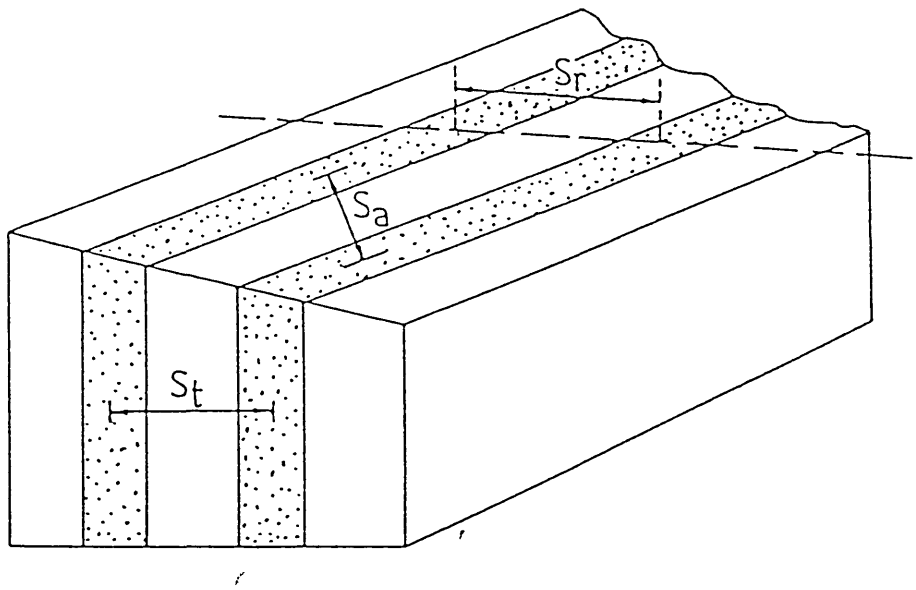
$$S_o \Delta T = 6.13 \ \mu m^oC \qquad (2.1)$$

Marder and Bramfitt(1975) also obtained a linear relationship when they plotted minimum interlamellar spacing against either cooling rate or undercooling (figure 2.6). Their data gave the following relationship between minimum spacing and undercooling:

$$S_o \Delta T = 8.02 \ \mu m^oC \qquad (2.2)$$

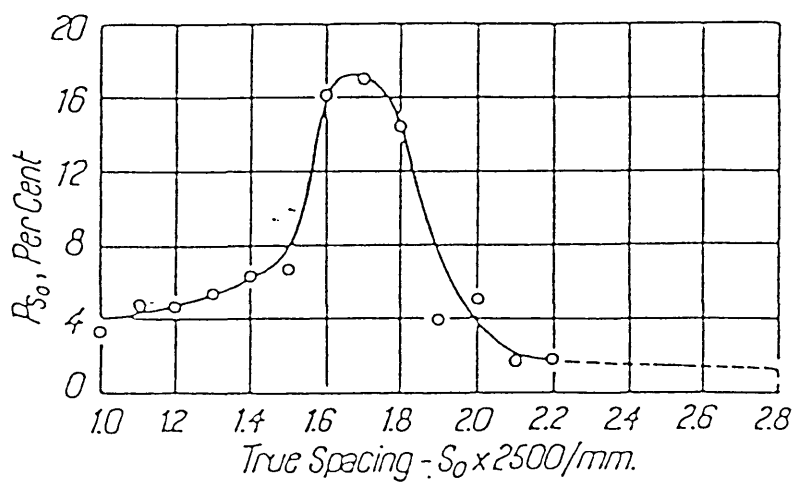
Roosz and Gacsi (1981) obtained an expression very similar to that of

Figure 2.3 The classification of spacings in a geometrically ideal lamellar structure.




$S_t$ – true spacing
$S_a$ – apparent spacing
$S_r$ – random spacing

Figure 2.4 The probable distribution of true spacings in a commercial eutectoid steel (Pellisier et al. 1942).



Marder and Bramfitt when they plotted the mean true interlamellar spacing against undercooling. Their constant of proportionality was 8.9. Like most other previous investigators, they observed that the interlamellar spacing is independent of austenitizing temperature, and that it is only governed by the transformation temperature, irrespective of whether the steel is transformed isothermally or by continuous cooling. A review of data on the interlamellar spacing of pearlite has recently been given by Ridley (1984). The review includes the various optical and electron microscopical methods for measuring interlamellar spacings. The present investigation adopted a linear intercept method described by Underwood (1970).

**2.4 The yield strength of pearlitic steels.**

The yield stress of pearlitic steels has been shown to be inversely related to the interlamellar spacing, and independent of prior austenite grain size and pearlite nodule size. In mild steels, the relationship between the yield stress $\sigma_y$ and grain diameter d, follows the Hall-Petch equation, expressed in the form:

$$\sigma_y = \sigma_i + k_y d^{-1/2} \qquad (2.3)$$

where $\sigma_i$ is the friction stress and $k_y$ is the Hall-Petch constant. Figure 2.7 shows a set of experimental results for mild steel where the linear relationship between $\sigma_y$ and $d^{-1/2}$ is illustrated (Honeycombe, 1980). Here $\sigma_i$ is the stress required to move free dislocations along the slip planes in the bcc crystals of ferrite, and can be regarded as the yield stress of a single crystal. This stress is very much dependent on temperature. The $k_y$ term represents the slope of the lines in figure 2.7, and as seen, it is temperature insensitive.

In pearlitic steels, the yield stress appears to obey the Hall-Petch relationship when the grain diameter term is replaced by the pearlite interlamellar spacing $S_o$, equation 2.4:

$$\sigma_y = \sigma_i + k_y S_o^{-1/2} . \qquad (2.4)$$

Lindbourg (1968), Hyzak and Bernstein (1976) and Bouse et al (1978) applied equation 2.4 to fully pearlitic steels and obtained a linear

Figure 2.5 The dependence of the minimum interlamellar spacing of pearlite on transformation temperature (Ridley, 1984)

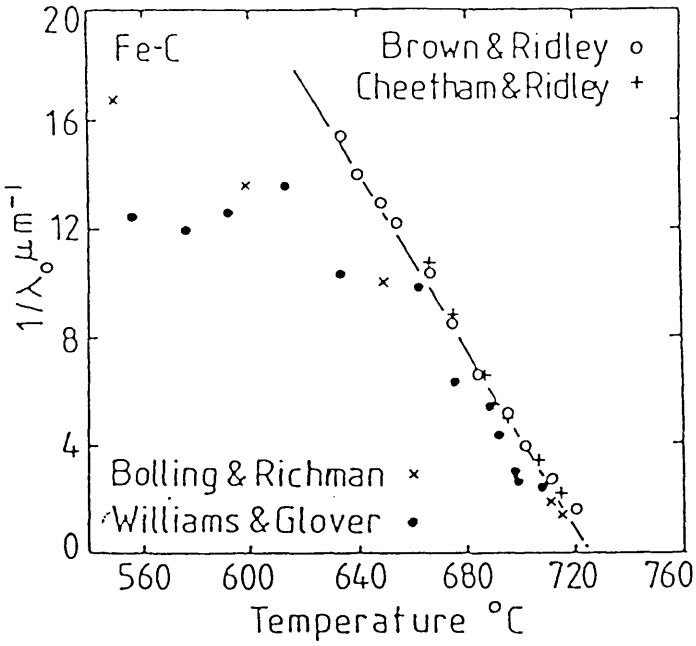



Figure 2.6a The effect of cooling rate on the minimum interlamellar spacing of pearlite after Marder and Bramfitt (1975). Data on nodule size is also included.

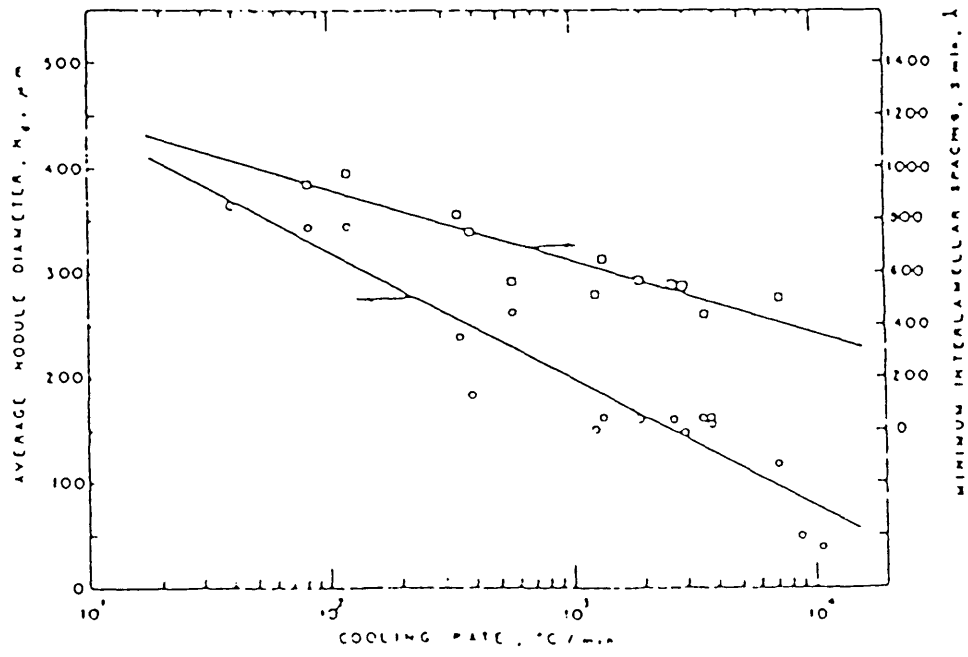


Figure 2.6b The effect of undercooling ($\Delta T$) on the minimum interlamellar spacing of pearlite after Marder and Bramfitt (1975).

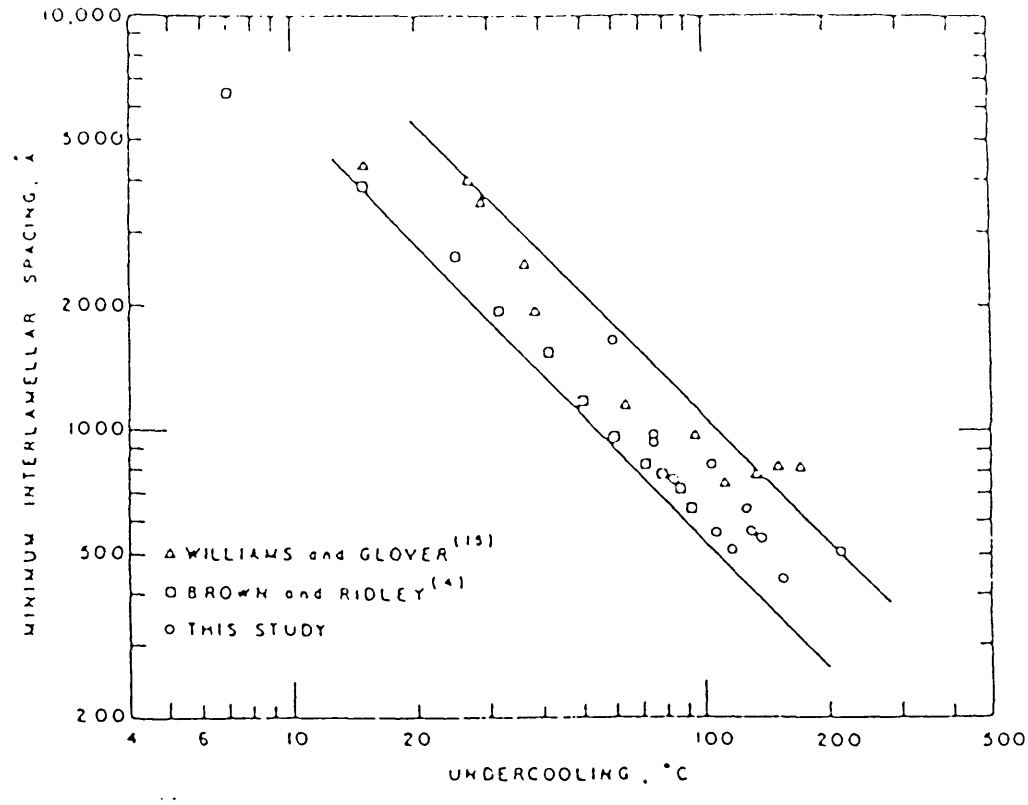
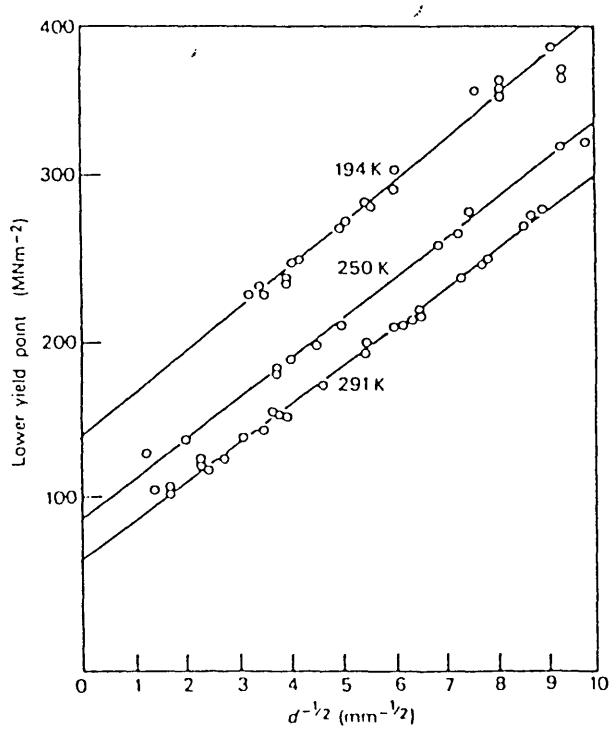



Figure 2.7 The dependence of the lower yield stress of mild steel on grain size d (Honeycombe, 1981).



relationship. However, they noted that the friction stress term was always negative when the expression was extrapolated to $S_o^{-1/2} = 0$. Bouse et al reported a value for $\sigma_i$ of -342 $MN/m^2$. This clearly contradicts the meaning of friction stress. Marder and Bramfitt (1975) had noted this problem, and proposed an equation for the yield stress based on $S_o^{-1}$. They used regression analysis on their data and obtained a linear relationship between the yield stress and the inverse of interlamellar spacing. The intercept on the stress axis which is taken to represent the friction stress was 139 $MN/m^2$ at room temperature. The friction stress of ferrite at room temperature as predicted by the data in figure 2.7 is, however, only about 60 $MN/m^2$. Apart from the relatively high value of $\sigma_i$, it is difficult to find the physical significance of a dependence of strength on the inverse of distance.

Gladman et al (1972) have expressed the yield stress of high-carbon ferrite-pearlite steels in the form:

$$\sigma_y = V_\alpha^{0.33}\,[2.3 + 3.8(\%Mn) + 1.13d^{-1/2}] + 4.1(\%Si) + 27.6(\%N)^{1/2} + (1-V_\alpha^{0.33})\,[11.6 + 0.25\,S_o^{-1/2}] \qquad (2.5)$$

where $\sigma_y$ is expressed in tons/$in^2$, d and $S_o$ are in mm, and where the Hall-Petch constants for ferrite, $(1.13\ V_\alpha^{0.33})$, and pearlite, $0.25(1-V_\alpha^{0.33})$, have the units of tons /$in^2/mm^{-1/2}$. $V_\alpha$ is the volume fraction of proeutectoid ferrite. A mild steel containing say, 90% ferrite by volume is predicted by equation 2.5 to have a Hall-Petch constant of 1.09 tons/$in^2/mm^{-1/2}$ or 0.53 $MN/m^{3/2}$. This value is slightly lower than that of 0.75 $MN/m^{3/2}$ obtainable from figure 2.7 (Honeycombe, 1980). A fully pearlitic steel has $V_\alpha = 0$, and the Hall-Petch constant is therefore 0.25 tons/$in^2/mm^{-1/2}$, which works out to be 0.12 $MN/m^{3/2}$. This value is significantly lower than that of 0.25 $MN/m^{3/2}$ predicted by Karlsson and Linden (1975), or that of 0.24 $MN/m^{3/2}$ proposed by O'Donnelly et al. Bouse et al (1980), on the other hand, obtained a value for $k_y$ in pearlite of 0.381 $MN/m^{3/2}$. They used a fully pearlitic microstructure and obtained that value by regression analysis. Karlson and Linden, and O'Donnelly et al used steels whose microstructures were a mixture of ferrite and pearlite, and expressed the yield stress in a form very similar to that used by Gladman et al. Whilst the present research will also attempt to determine $k_y$ in a fully pearlitic microstructure, it is

sufficient at this stage to note that the Hall-Petch constant for ferrite-pearlite microstructures tends to decrease as the pearlite volume fraction increases.

Takahashi and Nagumo (1970) have argued that the flow stress of pearlite is controlled by the mean free distance (mfd) in the pearlitic ferrite. When the flow stress was plotted against $(mfd)^{-1/2}$ they obtained a Hall-Petch relationship in which the friction stress was about 170 $MN/m^2$ at room temperature. O'Donnelly et al (1984) obtained a similar relationship between proof stress and ferrite mfd. The ferrite mfd was defined as the distance over which a dislocation may travel in ferrite without encountering an obstacle in the form of cementite lamellae. Since O'Donnelly et al used steels having microstructures which ranged from a medium carbon mixture of ferrite and pearlite to a fully pearlitic condition, they proposed separate expressions for the yield stress of proeutectoid ferrite and pearlite, namely:

$$\sigma_y^{\alpha} = \sigma_i^{\alpha} + k_y^{\alpha}(d_{\alpha})^{-1/2} \qquad (2.6)$$

$$\sigma_y^{p} = \sigma_i^{\alpha} + k_y^{p}(d_p)^{-1/2} \qquad (2.7)$$

where the superscript $\alpha$ refers to ferrite and p refers to pearlite, and where $d\alpha$ is the grain size of the proeutectoid ferrite and dp the mfd in pearlitic ferrite. It is worth noting that these equations utilize the same value of friction stress $\sigma_i$ for ferrite in both microstructures, although the Hall-Petch constants $k_y$ are different.

## 2.5 The tensile deformation of pearlitic steels

Lindbourg (1968) studied the morphology of fracture in two near-eutectoid steels over the temperature range 200°C to -196°C and noted that the fracture was always transgranular. At low temperatures fracture was cleavage, and followed the {100} cleavage planes of ferrite. At high temperatures the steels failed by tearing, and the fracture followed the cleavage planes of cementite, while plastic deformation occured in the ferrite. At room temperature, fracture was transgranular cleavage, but it was preceded by a considerable amount of plastic deformation.

Langford (1977) studied the deformation of pearlite in which the lamellae were oriented mainly parallel to the longitudinal direction and observed two modes of deformation. In one case the pearlite suffered homogeneous deformation when the slip distances of all operative slip systems in the ferrite were approximately equal, and the macroscopic deformation was also homogeneous. In the other case inhomogeneous interlamellar slip analogous to deck-of-cards slip took place when one highly stressed slip system in the ferrite was nearly parallel to the plane of the lamellae.

Porter et al (1978) have argued that cementite in pearlite may undergo brittle or plastic deformation depending on which cementite slip planes have been activated. In many cases cementite fails in a brittle manner because ferrite deformation at room temperature only activates the cementite slip planes (100), (001), (010) and Burgers vectors [100], [001] and [010], which together cannot provide sufficient slip systems to cause full ductile deformation. At higher temperatures, or after cold working, it is possible to activate the additional slip planes {110} and Burger's vector <111> so that the criterion of five independent slip systems for full ductility is satisfied.

Porter et al observed that the mode of deformation in coarse pearlite was different from that in fine pearlite. Coarse pearlite exhibited both homogeneous and inhomogeneous deformation. Crack initiation was due to dislocation pile-ups in the ferrite which caused the brittle failure of cementite and the successive rupture of the adjoining ferrite. In fine pearlite, homogeneous deformation predominated. Crack initiation was more difficult and was accompanied by relatively high plastic strains. The cementite deformed by a fibre loading mechanism and showed much ductility.

The shear flow stress of cementite, $\tau_C$, is thought to be inversely proportional to the thickness of the lamellae, t. Langford (1977) has expressed this relationship in the form:

$$\tau_C = \tau_{iC} + 0.24\ G_C \underline{b}_C (1/t) \qquad (2.8)$$

where $\tau_{iC}$ is the lattice friction shear stress of cementite, $G_C$ the shear modulus of cementite, and $\underline{b}_C$ is the Burgers vector in cementite.

The fracture of cementite lamellae is associated with either pile-up stresses or fibre loading stresses. In low-strength pearlite, the cementite lamellae are relatively thick and their flow stress is low as predicted by equation 2.8. The cementite tends to fail as a result of pile-up stresses (Langford 1977). Porter et al (1978) have expressed the pile-up stress in the form :

$$\tau_p = \frac{k_y . D . \epsilon_p}{\underline{b}(2S_t)^{1/2}} \qquad (2.9)$$

where $k_y$ is the Hall-Petch constant, D the distance between active slip planes, $S_t$ the interlamellar spacing, $\underline{b}$ the Burgers vector of the dislocation, and $\epsilon_p$ is the plastic strain. The pile up stress decreases with decreasing test temperature because the quantity $\epsilon_p$ is temperature dependent.

In fine pearlite, deformation has been associated with homogeneous fine slip. Fine slip implies smaller values of D, which together with the corresponding low values of $\epsilon_p$ due to increased strength, cause a decrease in $\tau_p$, although $S_t$ has decreased. These observations tend to suggest that at low test temperatures and in fine pearlite, there is less probability for cementite lamellae to fail as a result of pile-up stresses. When pearlite is subjected to relatively low strains, the strain $\epsilon$ in the ferrite is the same as that in the cementite if the lamellae have high aspect ratios, l/t. The fibre stress in the cementite is then given by Hooke's law:

$$\sigma_{Fc} = E_c . \epsilon \qquad (2.10)$$

where the Young's modulus for cementite, $E_c$, is assumed to be the same as that of the steel ($207 \times 10^3$ MN/m$^2$). The stress level along the lamella falls off at the ends if the lamella is surrounded by the matrix phase, ferrite. For low aspect ratios and high strains, it has been proposed that the maximum stress occurs at the centre of the lamella, with the ends virtually supporting no stress (Lindley et al, 1970). This maximum stress is governed by the shear strength of the matrix, $\tau$, so that:

$$\sigma_{max} = (l/t) . \tau \qquad (2.11)$$

The fracture stress of cementite lamellae has been estimated as 1400 - 7000 $MN/m^2$ (Lindley et al. 1970). This would imply that above a strain of about 0.7%, cementite lamellae could fracture due to fibre loading stresses, irrespective of whether any pile-up stresses are present.

## 2.6 The toughness of pearlitic steels

Fully pearlitic steels exhibit the poorest impact properties among the medium-high carbon ferritic-pearlitic steels (Pickering 1978). As the volume fraction of pearlite in a steel increases, the Charpy transition temperature progressively increases and the Charpy shelf energy decreases, figure 2.8. This behaviour is consistent with the observed increase in the yield stress as the pearlite content is increased, figure 2.9.

The effect of pearlite morphology on the impact properties of fully pearlitic steels has been reported by Gladman et al (1972) and Pickering (1978). The impact transition temperature of pearlite is raised by increasing the pearlite colony size or the thickness of cementite lamellae. The transition temperature is also raised by refining the pearlite interlamellar spacing. But since interlamellar spacing and thickness of cementite lamellae are directly related, their opposing effects tend to cancel one another. The overal effect of interlamellar spacing on the impact transition temperature is therefore small. However, there is an optimum spacing for the best impact toughness, as shown in figure 2.10 where a pearlite dilution factor of 1 is assumed (Pickering 1978).

The pearlite dilution factor $D_p$ is defined as:

$$D_p = 0.8V_p/C_s \qquad (2.12)$$

where $V_p$ is the volume fraction of pearlite and $C_s$ is the carbon content of the steel. Therefore a fully pearlitic steel of eutectoid composition has $D_p = 1$. It is however possible to obtain fully pearlitic microstructures in hypoeutectoid steels which have been transformed near the nose of the TTT curve. In such cases $D_p$ will be greater than one. On the other hand, increasing the carbon content of the pearlite lowers the dilution factor. But this is accompanied by an increase in the thickness of

Figure 2.8 The effect of carbon content (pearlite volume fraction) on the impact transition temperature and shelf energy value of normalized steels.

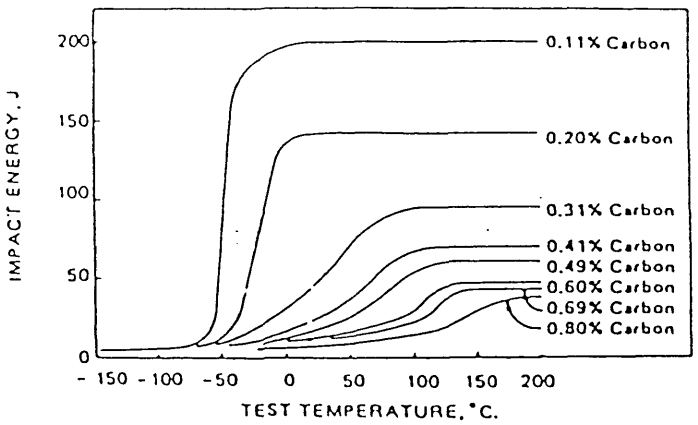
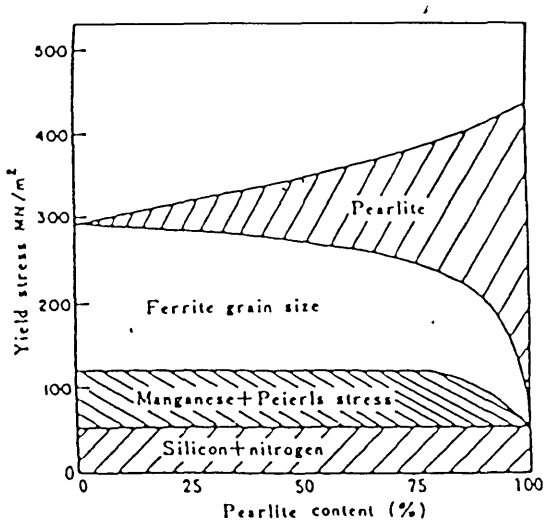
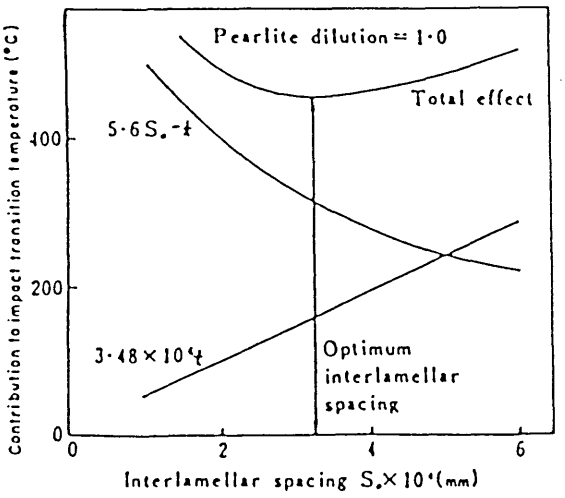



Figure 2.9 The effect of pearlite volume fraction on contributions of various strengthening mechanisms on the yield stress of ferrite-pearlite steels.

Figure 2.10 The effect of minimum spacing $S_o$ and thickness of cementite lamellae t on contribution to impact transition temperature.



cementite lamellae, which is detrimental to impact properties. The best impact properties are therefore achieved by increasing the pearlite dilution factor. And as $D_p$ increases, so does the optimum pearlite interlamellar spacing.

Hyzak and Bernstein (1976) have reported that the impact strength of fully pearlitic steels, and the dynamic fracture toughness $K_{ID}$, vary inversely with the prior austenite grain size. Similar observations have been made by Bouse et al (1978) who also observed that the Charpy transition temperature was lowered by decreasing $\gamma$ grain size. In both cases fatigue pre-cracked Charpy specimens were used in the investigations. It was proposed that the fracture toughness of pearlitic steels is controlled by a structural unit which acts as an effective grain size for cleavage. This unit was shown to be strongly related to the prior austenite grain size, and was of the same order as the cleavage fracture facets.

The decrease in impact toughness or dynamic fracture toughness with increasing $\gamma$ grain size was rationalized in terms of the energy requirements of a propagating crack. A running cleavage crack is expected to change its direction at a mismatch boundary, in this case the boundary of the effective grain size for cleavage. Most of the energy absorbing process of such a crack occurs at the mismatch boundary. A microstructure with a higher number of mismatch boundaries, i.e. a fine grained microstructure would therefore absorb much more energy when it fractures. Such a microstructure is said to have higher toughness. Since the Charpy test and the dynamic fracture toughness test are energy-related tests, a fine grained microstructure should exhibit good Charpy toughness and high $K_{ID}$ values. This is borne out experimentally.

## 2.7 Ferritic/pearlitic steels for rails.

Rail steels for certain applications may be required to have high toughness to resist brittle fracture. Such a requirement is in addition to possessing sufficient strength to resist plastic deformation and wear. Eutectoid steels provide the highest strength among the medium-high carbon ferritic/pearlitic steels. But their toughness is relatively low, figure 2.8. The impact toughness of these steels can be improved by refining the prior austenite grain size (Bouse et al, 1978); but for

similar grain sizes, the hypoeutectoid steels still possess better toughness, figure 2.11. The low carbon ferritic steels have even better toughness, but cannot meet the strength requirements for rail applications, even after grain refinement. Hypoeutectoid rail steels are therefore made from medium-high carbon steels whose microstructures are essentially pearlitic, with the proeutectoid ferrite being confined to a grain boundary network.

The strength and impact toughness of medium-carbon hypoeutectoid steels depend on the pearlite spacing, the amount of proeutectoid ferrite and on the prior austenite grain size (Gladman et al, 1972, Bouse et al, 1978). The effect of interlamellar spacing on the yield strength of 0.6% and 0.8%C steels is shown in figure 2.12. The dependence of tensile strength on the interlamellar spacing of the 0.6%C steel is shown in figure 2.13. It is evident that strength increases as the pearlite spacing is refined. The scatter in the data suggests that there are variables other than interlamellar spacing which contribute to the strength of these steels. Gladman et al (1972) observed, for example, that in steels containing small amounts of discontinuous ferrite, the yield strength is very strongly influenced by the interlamellar spacing of the pearlite. However, if the ferrite is present as a continuous network, the yield strength is only partly dependent on pearlite spacing. It should be noted as well, that the strength of hypoeutectoid steels can be influenced by solid solution strengthening of the proeutectoid ferrite, if present in sufficient amounts.

## 2.8 Objectives of the present research

Theories of pearlite transformation, its kinetics and morphology, have already received significant attention, and appear to be well understood. A fair amount of research has also been devoted to structure/property relationships in pearlitic steels. Certain aspects, however, are not well understood, and it was the intention of this research to attempt to clarify the following:

(i) The influence of $\gamma$ grain size on pearlite colony size and pearlite nodule size.

(ii) The influence of $\gamma$ grain size on the yield strength (proof stress) and

ultimate tensile strength of these steels.

(iii) The influence of $\gamma$ grain size on the plane strain fracture toughness $K_{IC}$.

(iv) The role of pearlite interlamellar spacing in controlling $K_{IC}$.

(v) The application of the Hall-Petch equation in describing yielding in pearlite.

(vi) The role of interlamellar spacing on the tensile ductility of pearlite.

(vii) The influence of proeutectoid ferrite on the strength and fracture toughness of rail steels.

Figure 2.11 Charpy transition temperature as a function of the prior austenite grain size for rail steels (Bouse et al. 1978).

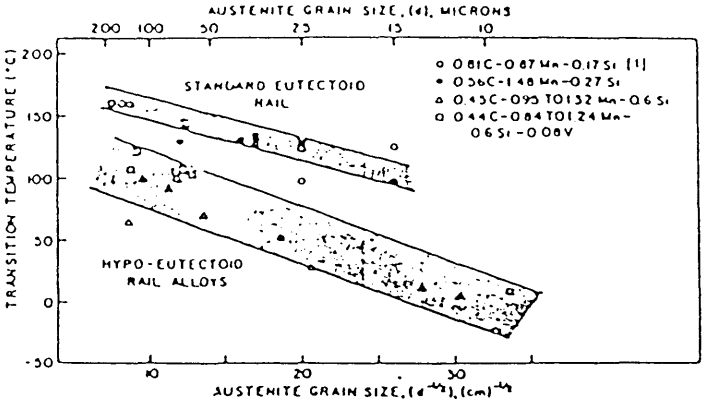



Figure 2.12 The effect of inter-lamellar spacing on the yield strength of a 0.6% and 0.8%C steel (Gladman et al. 1972).

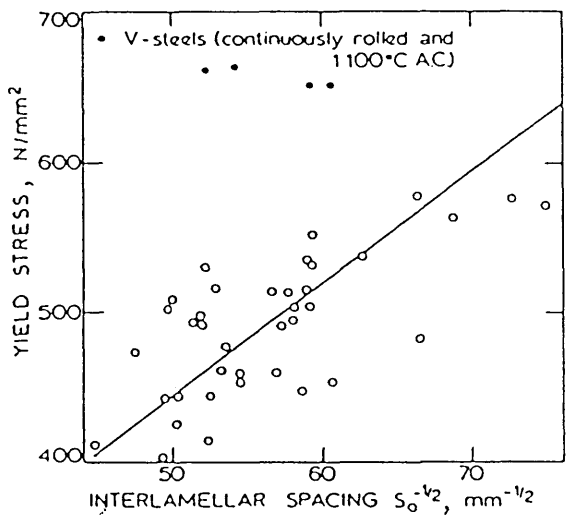
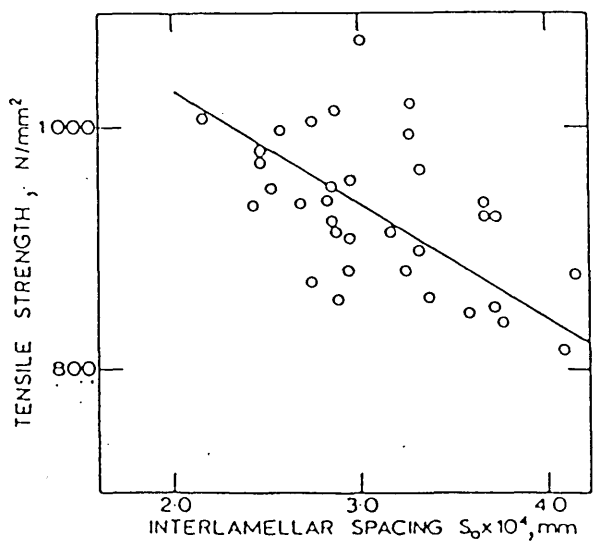



Figure 2.13 The effect of inter-lamellar spacing on the tensile strength of a 0.6%C steel (Gladman et al. 1972).



# 3. C L E A V A G E F R A C T U R E

## 3.1 Modes of fracture in metals.

Macroscopically fracture may be classified as either brittle or ductile. Brittle fracture in metals is characterized by low toughness, and occurs very rapidly, requiring low energy and low strain to fracture. This mode of fracture normally takes place before general yield. Ductile fracture is characterized by high toughness, and occurs after a metal has undergone substantial plastic deformation. It takes place relatively slowly, and requires high energy and high strain to fracture.

Microscopically fracture may be classified as either cleavage or fibrous. In addition, fracture may occur in a transgranular or intergranular manner. Transgranular cleavage fracture occurs by the direct separation of crystals along definite low index crystal planes. There is little plastic deformation associated with this mode of fracture since only a small amount of localised yielding is involved at the initiation stage. Intergranular cleavage fracture is associated with the fast propagation of cracks along grain boundaries which have been weakened either by the segregation of impurity elements or by the presence of a continuous film of a brittle phase. In steels intergranular cleavage may occur along prior austenite grain boundaries as a result of as-quenched embrittlement or temper embrittlement. Micromechanisms of cleavage fracture in steels have been reviewed by Knott (1966) and Curry (1980), amongst others.

Transgranular fibrous fracture is associated with intense localised plastic deformation of a metal. In materials containing inclusions or second phases, fibrous fracture involves the nucleation, growth and subsequent coalescence of voids. The voids are initiated by decohesion of the particle-matrix interface or by the cracking of the particles themselves. This is thought to be a result of the stress concentration caused by the particles (Gurland and Plateau, 1963). As the material is strained , the voids grow in directions transverse as well as parallel to the applied tensile stress. Final coalescence by an internal necking mechanism results in the dimpled fracture surface characteristic of ductile fracture.

Intergranular fibrous fracture is known to occur by the linkage of

microvoids formed around grain boundary second-phase particles. This type of fracture is favoured to transgranular fibrous fracture in those situations where the density of weakly bonded particles within the grains is lower than on the grain boundaries (Knott, 1977). Mechanisms of fibrous fracture have been studied by Rice and Tracey (1969), Hahn and Rosenfield (1975), Goods and Brown (1979), Knott (1980) and others.

### 3.2 Cleavage fracture in mild steels.

The commonly accepted criterion for cleavage fracture in mild steels is that fracture occurs when the local tensile stress exceeds some critical stress $\sigma_f$, called the cleavage fracture stress. In ferritic steels cleavage planes are generally the {100} planes of iron. Before cleavage fracture can occur, a certain amount of localised plastic deformation must take place. This was demonstrated by Low (1954) who studied the effect of ferrite grain size on cleavage fracture stress and compressive yield stress in mild steels, figure 3.1. He observed that in unnotched specimens the fracture stress was always equal to or greater than the uniaxial yield stress, making it apparent that plastic flow was a necessary precursor to cleavage. The yielding that preceeds cleavage nucleation may occur by slip or twinning.

A dislocation model for cleavage fracture in steels proposed by Zener (1948) and Stroh (1954) suggested that cleavage fracture may be nucleated as a result of the stress levels ahead of a dislocation pile-up. The dislocations may be squeezed together to produce a crack nucleus, as illustrated in figure 3.2. If the pile-up can produce a crack nucleus, then there is already sufficient energy to propagate the crack, if the surface energy of the system remains constant. Crack nucleation is predicted to be the most difficult stage in cleavage produced by this mechanism, and thus the fracture process is nucleation-controlled. This model further predicts that cleavage fracture occurs when a critical value of effective shear stress, $\tau_e$, given by equation 3.1, is attained.

$$\tau_e \equiv \tau_y - \tau_i \geq \left[\frac{12\mu\gamma_p}{\pi(1-\nu)d}\right]^{1/2} \qquad (3.1)$$

Here $\tau_y$ is the shear yield stress, $\tau_i$ the lattice friction shear stress, $\mu$ the shear modulus, $\nu$ Poisson's ratio, $\gamma_p$ the surface energy of ferrite (14 J/m$^2$) and d is the slip band half-length.

Figure 3.1 The grain size dependence of yield stress ($\sigma_y$) and cleavage fracture stress ($\sigma_f$) in mild steel at -196 $^{o}$C.

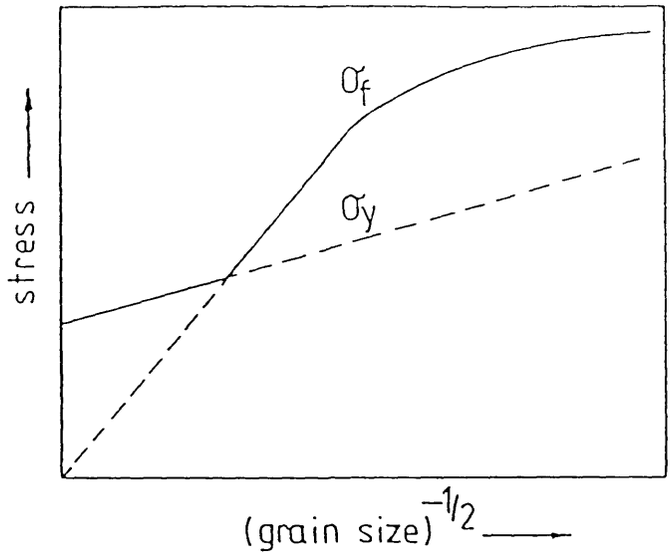
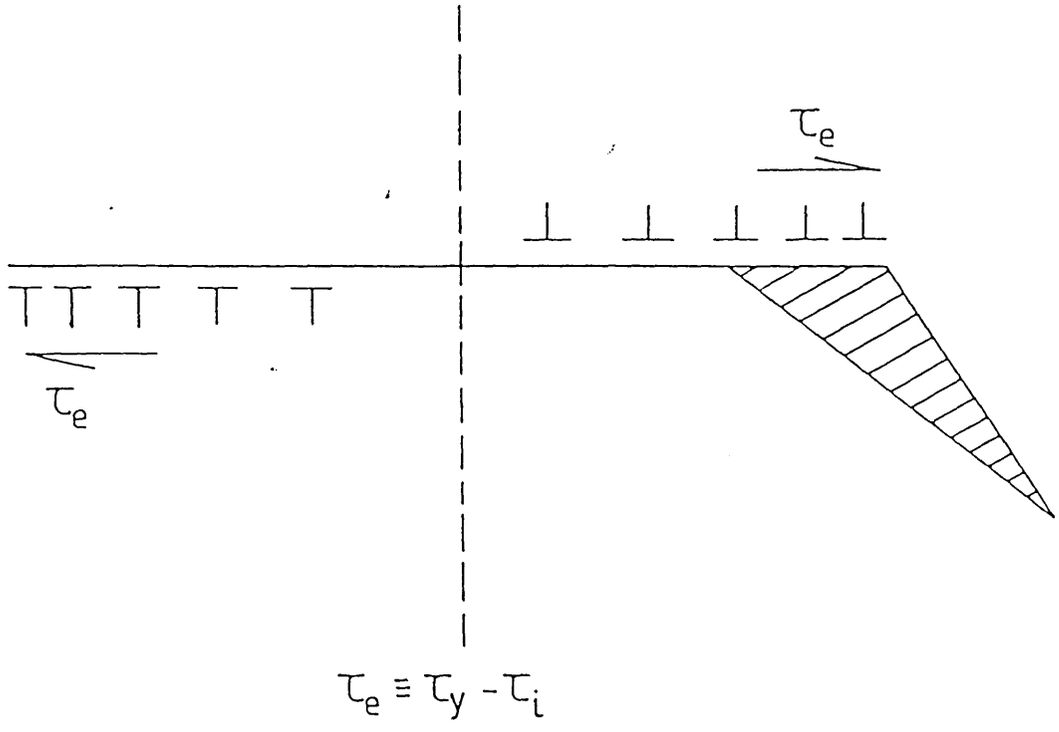



Figure 3.2 Cleavage fracture nucleation ahead of a dislocation pile-up according to the Zener/Stroh model.



The Zener/Stroh model could not explain why cleavage fracture predominates at low temperatures. Further, experiments with notched bar specimens indicated that it was the attainment of a critical tensile stress that was necessary to precipitate cleavage fracture in mild steels. Since tensile stresses govern the propagation of crack nuclei, then this would imply that cleavage in mild steels is propagation controlled. Cottrell (1958) proposed a critical tensile stress and propagation-controlled mechanism by suggesting that two dislocations on intersecting {101} slip-planes may interact to form a sessile dislocation whose Burgers vector is normal to the cleavage plane, figure 3.3 and equation 3.2:

$$a/2\,[\bar{1}\bar{1}1]_{(101)} + a/2\,[111]_{(\bar{1}01)} \longrightarrow a\,[001]_{(001)} \qquad (3.2)$$

This model predicts that crack nucleation is much easier because the dislocation interaction is accompanied by a reduction in energy. The critical event is then the attainment of the cleavage fracture stress $\sigma_f$, which is given by:

$$\sigma_f \geq \frac{2\mu.\gamma_p.d^{-1/2}}{k_y^s} \qquad (3.3)$$

where $k_y^s$ is the shear Hall-Petch yielding constant, $\mu$ is the shear modulus, $\gamma_p$ is the surface energy and d is the grain size. Whereas Cottrell's model explained the roles of tensile stress, grain size and yielding parameters on the fracture process, it did not include the influence of other microstructural variables like carbide size and carbide particle distribution which are known to influence cleavage behavior. A model to include the influence of carbide size was subsequently developed by Smith (1966).

Smith suggested that an impinging dislocation pile-up may crack a grain boundary carbide, and the resulting microcrack may then propagate as a Griffith defect under the combined influence of the pile-up and the applied stress, figure 3.4. According to this model, the carbide thickness plays a crucial role in determining the fracture stress. The failure criterion is given in equation 3.4a:

$$(C_o/d)\sigma_f^2 + \tau_e^2\{1 + 4/\pi(C_o/d)^{1/2}\,(\tau_i/\tau_e)\}^2 \geq (4E\gamma_p)/\pi(1-\nu^2)d \qquad (3.4a)$$

Figure 3.3 Model for cleavage fracture nucleation in a bcc metal after Cottrell.

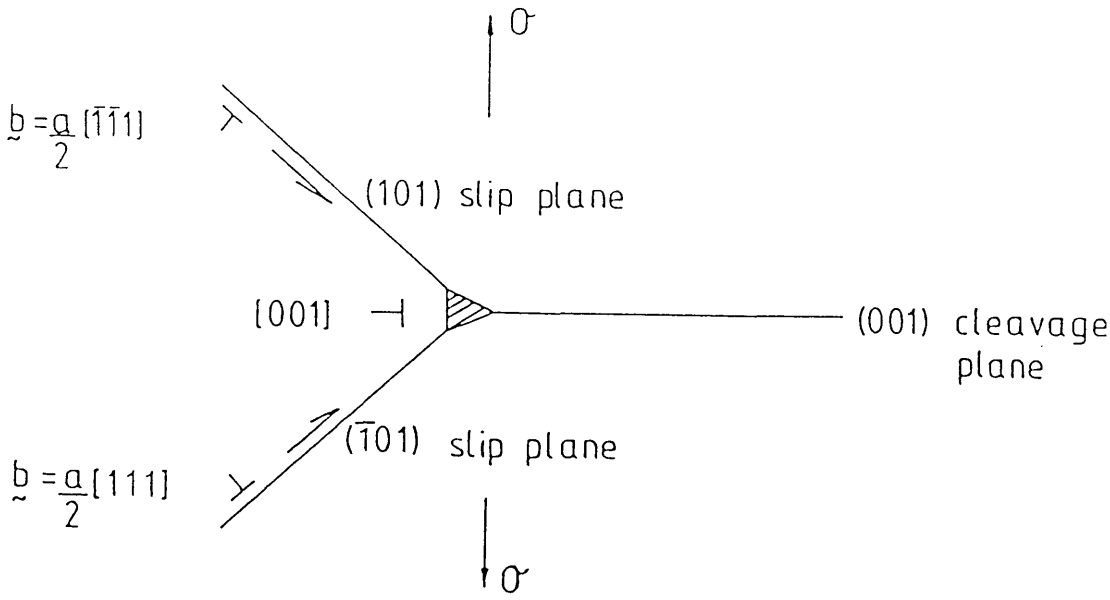
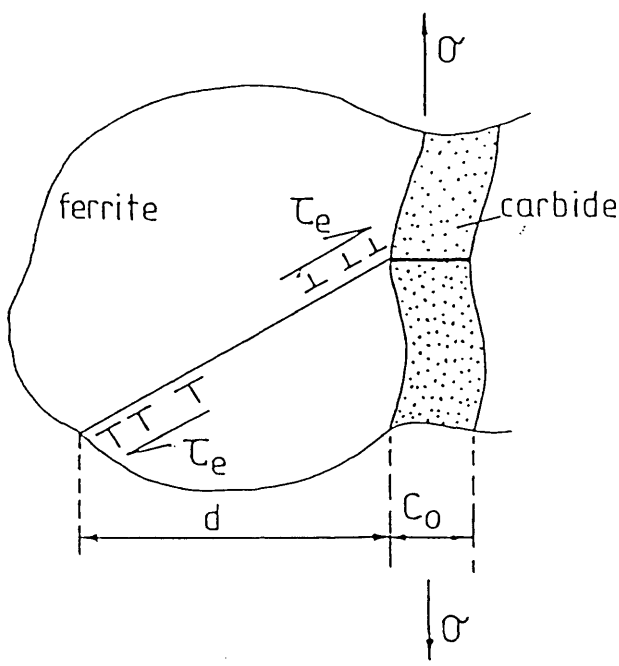



Figure 3.4 Smith's model for cleavage fracture in mild steels.



where d is the grain size, $C_o$ the thickness of the grain boundary carbide, $\tau_e$ the effective shear stress, $\tau_i$ the friction shear stress, E the Young's modulus, $\gamma_p$ the effective surface energy of ferrite and $\nu$ Poisson's ratio. The second term in the left hand side of equation 3.4a is small and may be ignored. By multiplying the remaining terms by the factor $d/C_o$, the expression for the cleavage fracture stress $\sigma_f$ becomes:

$$\sigma_f = \left[ \frac{4E.\gamma_p}{\pi(1-\nu^2)C_o} \right]^{1/2} \qquad (3.4b)$$

Cleavage in steels containing discrete carbide particles is caused by the propagation of microcracks formed in the carbide particles when the fracture obeys a critical tensile stress criterion. The cleavage fracture stress is then largely dependent upon the size of the cracked carbide particle. It has been shown that in steels, carbides can also crack by a fibre loading mechanism (Lindley et al, 1970). At low temperatures and at high strain rates, slip in steels is hindered, and cleavage fracture can be caused by deformation twins.

The cleavage fracture stress in mild steels is independent of temperature and strain rate if fracture is slip induced (Knott, 1966). The temperature independence of $\sigma_f$ was further demonstrated in a 3% silicon iron by Griffiths and Owen (1971). They determined $\sigma_f$ values over the temperature range +50 to -196 °C and obtained an almost constant value of about 1000 $MN/m^2$. Based on the observations of Knott and those of Griffiths and Owen, it has been taken for granted that the cleavage fracture stress of medium-high carbon steels in either ferritic, pearlitic, bainitic or martensitic condition is also temperature independent. One of the objectives of the present research will be to study the influence of test temperature on the cleavage fracture stress of pearlitic steels.

In spheroidised plain carbon steels there are no grain boundary cementite films. Curry and Knott (1978) have suggested that the spheroidal carbide particles can crack and act as nuclei for cleavage crack propagation. The crack nucleus is then penny-shaped, and cleavage fracture is caused by the propagation of such nuclei which act as Griffith-type defects. The Griffith crack propagation criterion for a penny-shaped crack of length $C_o = 2r$, where r is the radius of the carbide spheroid, is given by:

$$\sigma_f = \left[\frac{\pi.E.\gamma_p}{2(1-\nu^2)r}\right]^{1/2} \qquad (3.5)$$

where the terms are as defined before and where plane strain conditions are assumed. Fracture occurs when the largest cracked carbide particle is subjected to sufficient local tensile stress to satisfy the crack propagation energy balance.

### 3.3 Cleavage fracture in bainitic steels

Brozzo et al (1977) have proposed that certain structure/property relationships in bainitic steels can be based on the bainite packet size as being equivalent to the polygonal ferrite grain size in mild steels. In a study of a low-carbon 2Mn-3Cr bainitic steels, it was observed that cleavage resistance was controlled by the bainite packet size, although yielding was governed by the substructure inside a packet which may be viewed in terms of lath diameter (Naylor, 1979). The cleavage fracture stress $\sigma_f$ was found to be proportional to the reciprocal square root of the packet size, $d_B$ (figure 3.5). Cleavage was therefore thought to occur by the propagation of a Griffith crack from one bainite packet to an adjacent one. Measured values of the fracture stress and the packet size were used to calculate an effective surface energy $\gamma_p$ of about 120 J/m$^2$.

The packet size, which is controlled by the prior austenite grain size, correlated very well with the cleavage facet size. Roberts (1970) also observed that the cleavage facet size in bainitic steels corresponded directly to the packet size. The cleavage fracture stress was thought to be controlled solely by the bainite packet size. By varying the packet size, values of $\sigma_f$ ranged from 1700 to 2700 MN/m$^2$. These values are greater than those obtained in mild steels for corresponding values of $d^{-1/2}$ when data from the literature are extrapolated (figure 3.5).

The dependence of $\sigma_f$ on the bainite packet size has also been reported by Kotilainen (1980), Kamada et al (1976) and Kotilainen et al (1982). Kotilainen (1982) further suggested that the cleavage fracture stress of bainitic steels consists of three components which include a Griffith stress, the internal resistance of the crystal, and a strain hardening and probability term. The packet size was thought to contribute only to the Griffith stress.

A study by Curry (1984) of a Mn-Mo-Ni pressure vessel steel in a bainitic condition showed that both the yield strength and the cleavage fracture stress of this material were controlled by the same microstructural features. It was observed that cleavage fracture in this steel did not involve the propagation of microcracks whose length was equal to any of the possible microstructural units, namely carbide particle size, lath width or bainite packet size. The similar microstructural dependences of yield stress and cleavage fracture stress were thought to suggest that the controlling step in the micromechanism of cleavage fracture involved dislocation motion. This is illustrated in figure 3.6 where $\sigma_f$ is plotted against $\sigma_y$, and from where the following relationship was obtained:

$$\sigma_f = 2.84(\sigma_y - 275) \qquad (3.6)$$

Curry argued that if cleavage fracture was dislocation nucleated, then some mechanism for easy crack nucleation must operate before cleavage could be propagation controlled, i.e. tensile stress controlled. He assumed that cleavage in this steel was propagation controlled, and proposed that it operated by a dislocation mechanism similar to that described by Cottrell (see section 3.2). He obtained a value for $\gamma_p$ of 5.6 $J/m^2$ and a lattice friction stress of 275 $MN/m^2$, both of which are significantly lower than the values for mild steel (14 $J/m^2$ and 400 $MN/m^2$ respectively at -196 °C.

The conflicting results of the works of Brozzo et al (1977) and Curry (1984) cannot easily be rationalized. The fact that Brozzo et al (1977) determined their $\sigma_f$ values at the nil ductility temperature (NDT) which varied with bainite packet size makes it difficult to predict the temperature dependence of $\sigma_f$ in their material. In addition, it is difficult to assess the correlation of $\sigma_f$ and $\sigma_y$, if any, from their limited results. Curry, on the other hand, did not study the temperature dependence of $\sigma_f$ in his material, and assumed that the fracture process was necessarily propagation controlled.

The results of Brozzo et al and Curry are further complicated by the observations of Wallin et al (1984) who suggested that cleavage fracture in bainitic steels is controlled by carbide distribution, rather than bainite packet size. A recent study of a medium carbon Ni-Cr-Mo steel in a

Figure 3.5 Critical fracture stress $\sigma_f$ as a function of size of microstructural units separated by high-angle boundaries in steels.

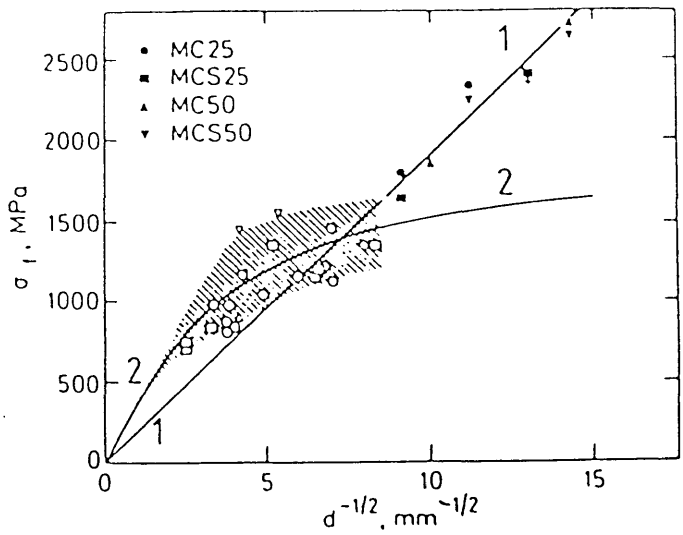
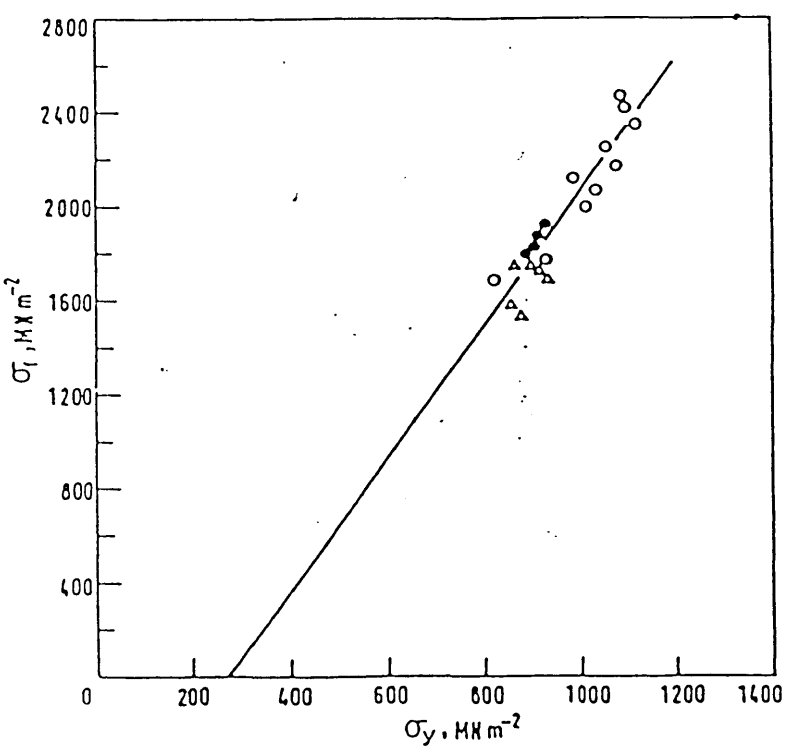



Figure 3.6 Correlation between cleavage fracture stress $\sigma_f$ and yield stress $\sigma_y$ in a Mn-Mo-Ni bainitic steel after Curry(1984).




○ tempered, ferritic ● as transformed, ferritic △ as transformed, bainitic

mixed martensitic/bainitic condition by Tomita and Okabayashi (1985) suggests that the 0.2 % proof stress in this steel is related to the prior austenite grain size by a Hall-Petch relationship (figure 3.7). Since packet size is controlled by prior austenite grain size, then it can be implied that a similar relationship will be observed between $\sigma_{0.2}$ and packet size in lath microstructures. Considering all these suggestions, it can be concluded that there is no generally agreed model for the micromechanism of cleavage fracture in bainitic steels.

### 3.4 Cleavage fracture in a martensitic steel.

A study of a Mn-Ni-Mo pressure vessel steel in a martensitic condition by Bowen and Knott (1984) has shown that cleavage fracture in this steel is not controlled by the prior austenite grain size, martensite packet size or lath width. The packet size was strongly dependent on prior austenite grain size. The mean cleavage facet size showed reasonable agreement with the mean packet size. But the width of martensite laths was essentially independent of prior austenite grain size.

In the temperature range -160 to -100 °C, the cleavage fracture stress $\sigma_f$ was found to be temperature independent; in sharp contrast to the observed yield stress behaviour in this temperature range, figure 3.8. This was thought to be strong evidence for a tensile stress controlled fracture process, generally taken to imply propagation controlled. A tentative suggestion that cleavage fracture in this steel followed an inclusion controlled mechanism was further modified (Bowen, 1985) to suggest that $\sigma_f$ was controlled by the largest observed carbide particle in the microstructure. The critical event was thought to be the propagation of a carbide-size Griffith microcrack where the effective surface energy $\gamma_p$ was in the range 4.3 to 6.1 $J/m^2$. It was further noted that:

(i) Observed packet-size cracks in the microstructure were not microcracks, but rather secondary cracks, because facet size was well correlated to packet size, and it was not possible for the critical crack size to be of the order of facet size.

(ii) The microstructural unit controlling cleavage was independent of the prior austenite grain size, and of any features that were dependent on

Figure 3.7 The prior austenite grain size ($d_\gamma$) dependence of proof stress in a 0.4% C.Ni-Cr-Mo steel in martensitic/bainitic condition.

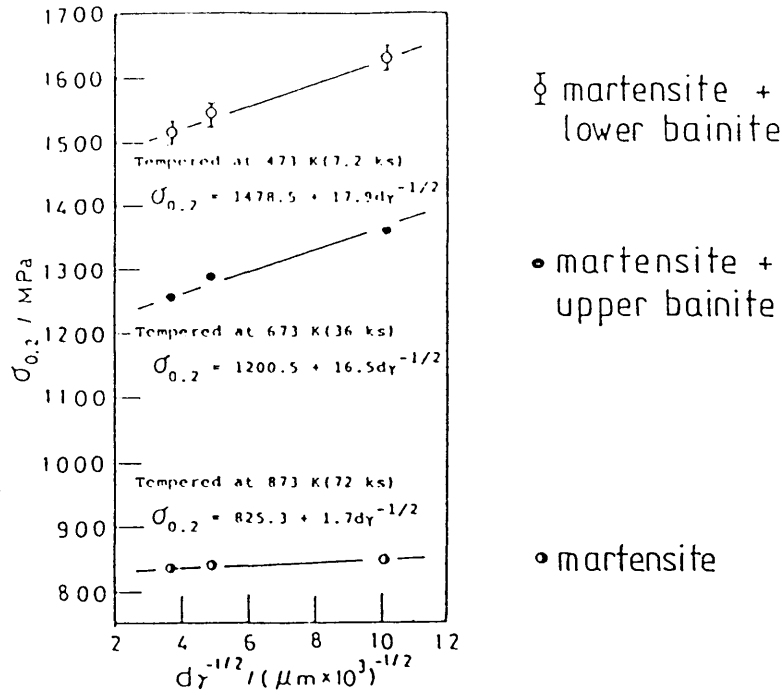
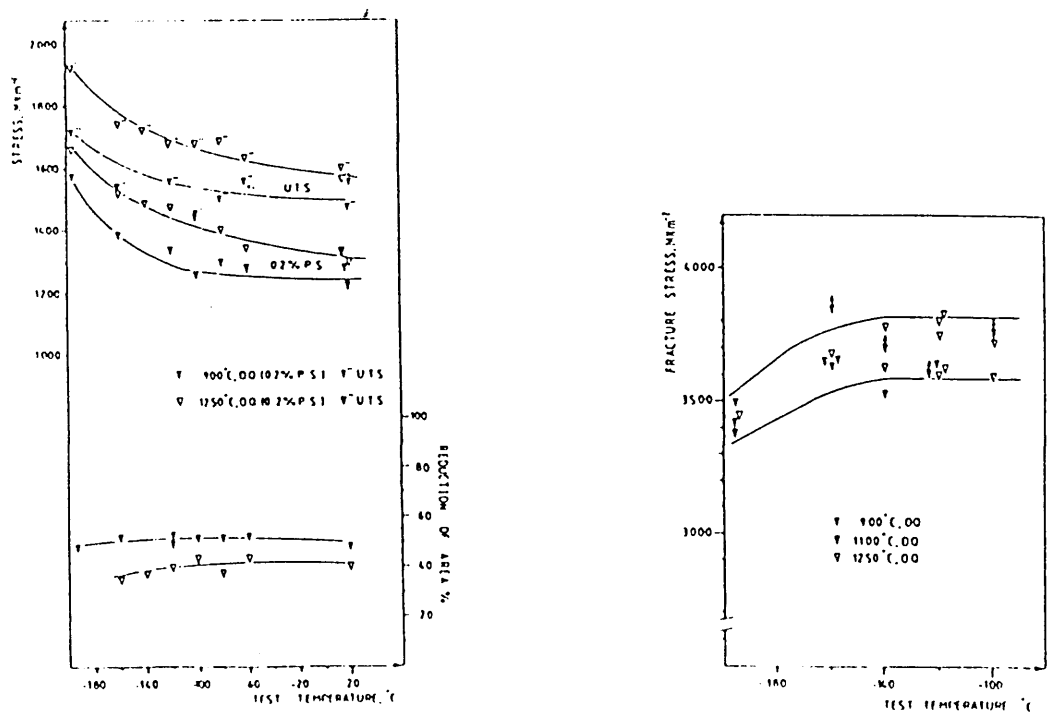



Figure 3.8 The variation of proof stress, ultimate tensile stress and cleavage fracrure stress with temperature in A 533 B pressure vessel steel.



the austenitising temperature.

(iii) The calculated $\gamma_p$ values of 4.3 to 6.1 J/m$^2$ were lower than those of 11 to 17 J/m$^2$ reported for simple ferrite-carbide microstructures. It was thought the increased local stress intensification that results from more heavily dislocated microstuctures, as in martensite, would result into an apparently lower value of $\gamma_p$ because the true stress at the carbide would be higher than that represented by $\sigma_f$. When a microcrack forms in a carbide, $\gamma_p$ may be taken as a measure of the resistance of the microcrack to penetrate into the matrix. A heavily dislocated matrix would therefore lower the effective surface energy.

### 3.5 Factors affecting $\sigma_f$ in low carbon mild steels

The effect of temperature on the cleavage fracture stress of mild steels has been reported by Knott (1966), Griffith and Owen (1971), among others. For temperatures between room temperature and -196 °C, the cleavage fracture stress is essentially temperature independent. Since in this temperature range the yield stress increases with decreasing test temperature, cleavage fracture in mild steels has always been associated with a tensile stress controlled mechanism. The slight decrease in $\sigma_f$ at about -196 °C has been associated with a twin-induced cleavage fracture, as opposed to the slip-induced fracture which predominates at higher temperatures (Oates 1969).

The cleavage fracture stress is strongly influenced by grain size. Although Smith's theory for cleavage fracture in mild steels shows that $\sigma_f$ is determined by carbide size, variations in grain size normally produce corresponding variations in carbide size. Results obtained by Curry and Knott (1976) show that the cleavage fracture stress increases with increasing reciprocal square root of ferrite grain size, figure 3.9. The fracture stress results of several other workers which were summarized by Knott (1976), figure 3.10, show a broad agreement with the results of Curry and Knott (1976).

The effect of prestrain on cleavage fracture stress has been reported by Groom and Knott (1975) and Sandstrom et al (1981). It was observed that the cleavage fracture stress increases with increasing prestrain.

Figure 3.9 Variation in cleavage fracture stress $\sigma_f$ with ferrite grain size d (Curry and Knott, 1976).

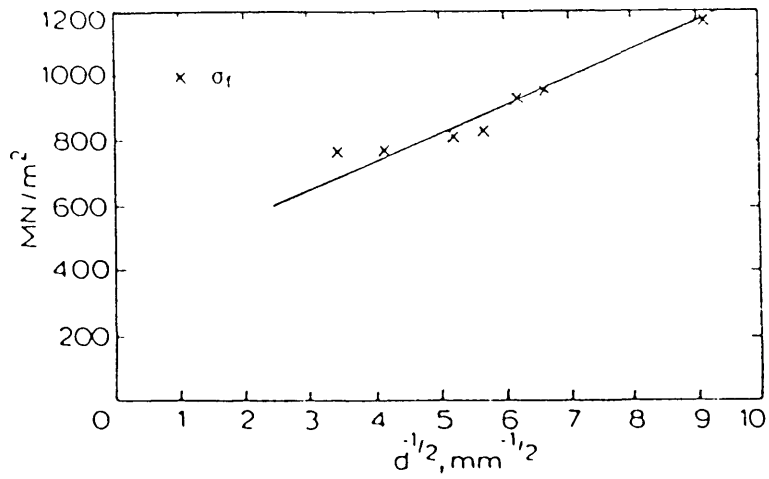



Figure 3.10 Variation in cleavage fracture stress $\sigma_f$ with ferrite grain size d (several workers, from Knott, 1976).

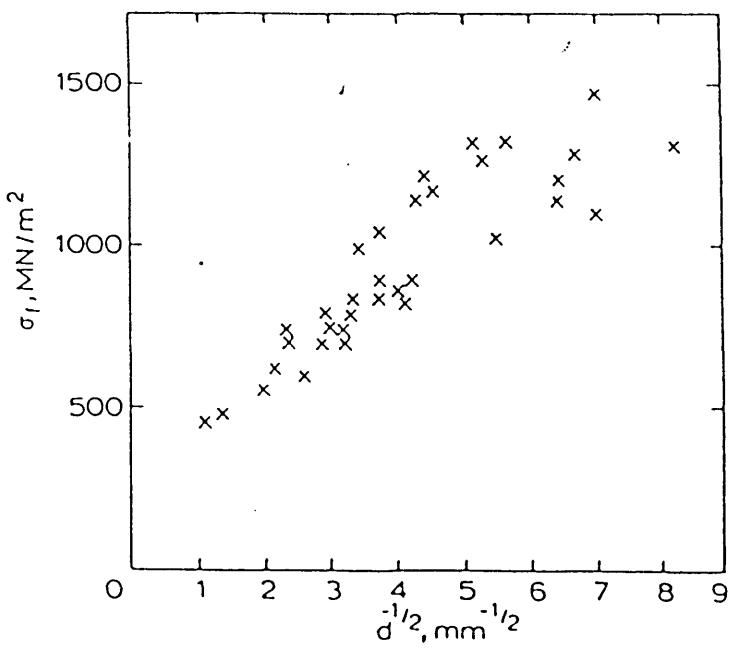


figure 3.11. In addition, strain ageing has the effect of slightly reducing the value of $\sigma_f$ (Sandstrom et al). The increase in $\sigma_f$ with increasing prestrain was attributed to the increase in the friction stress term which appears in the left hand quantity of equation 3.4a. This term is normally ignored in calculations of $\sigma_f$, but considering that $\tau_i$ is the sum of all the athermal components due to solution, precipitation and strain hardening, then in the presence of prestrain, this term is no longer negligible.
The effective surface energy $\gamma_p$ is independent of the amount of prestrain, but is slightly reduced by increasing the amount of strain ageing. Values of $\gamma_p$ obtained by Sandstrom et al (1981) which were 3.1 ± 0.2 J/m$^2$ for a non-aged material and 2.6 ± 0.2 J/m$^2$ for material aged for 30 minutes were only slightly higher than the true surface energy of ferrite (2.0 to 2.5 J/m$^2$). This meant only an insignificant amount of plastic deformation took place at the crack tip before the crack could grow. The reduction in effective surface energy with strain ageing is attributed to the dislocations becoming pinned down during ageing, thus making dislocation activity more difficult.

### 3.6 Cleavage fracture in fully pearlitic steels

The micromechanisms of cleavage fracture proposed for mild steels are unlikely to be operative in fully pearlitic steels due to the differences in microstructure. Fully pearlitic steels have neither grain boundary carbides, nor discrete carbide particles as found in low carbon mild steels. Park and Bernstein (1978) proposed that cleavage fracture in fully pearlitic steels is propagation controlled. They suggested that crack nucleation was due to dislocation pile-ups in the ferrite which impinged on the cementite lamellae and caused them to crack. This results in an array of cracks in the cementite lamellae which may then link up by the process of shear cracking proposed by Miller and Smith (1970), figure 3.12. When the microcrack formed by this process is large enough, it may be assumed to act as a Griffiths-type crack which initiates cleavage fracture.

Park and Bernstein assumed that the cleavage fracture stress in fully pearlitic steels was temperature independent. This was consistent with a propagation controlled cleavage mechanism. However, Lewandowski and Thompson (1984) have recently shown that the cleavage fracture stress

Figure 3.11 The variation of $\sigma_f$ with degree of prestrain for aged and unaged materials (Sandstrom et al, 1981).

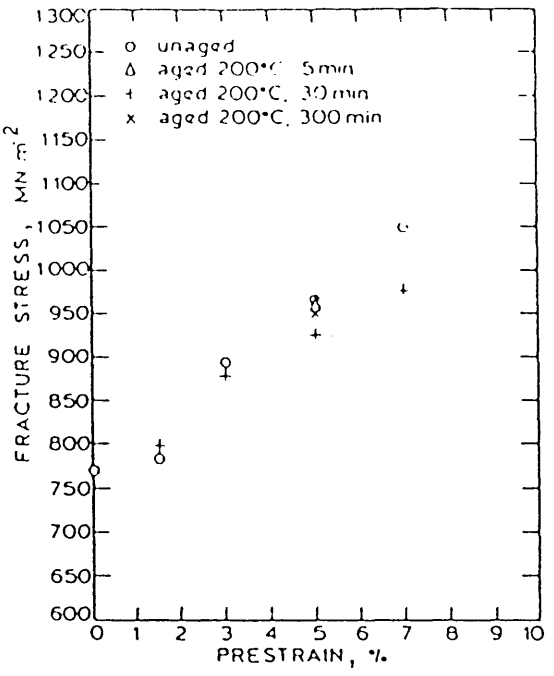
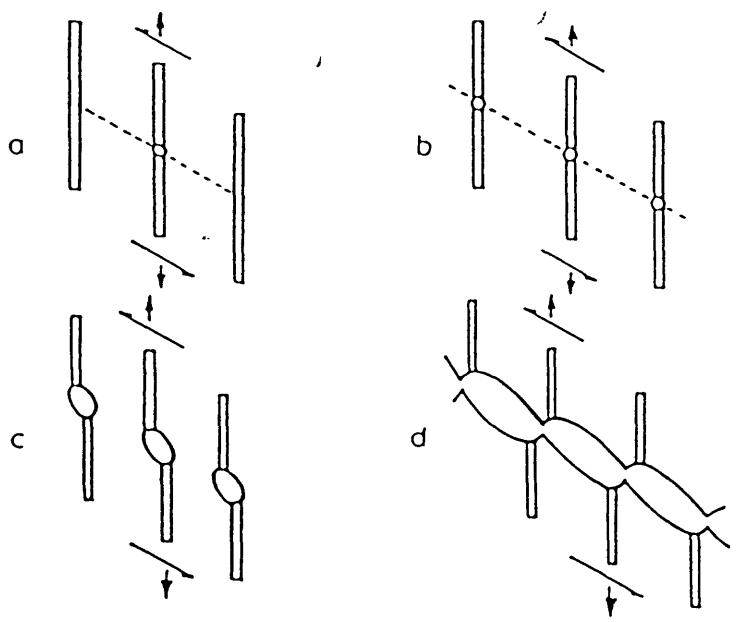



Figure 3.12 Shear cracking of pearlite, after Miller and Smith (1970).




*a* cracking of a cementite plate; *b* shear zone developing in the ferrite causing cracking of adjacent plates; *c* and *d* void formation and coalescence

is temperature independent only in fine pearlite. In coarse pearlite, the cleavage fracture stress was found to increase with decreasing test temperature. They suggested that in such microstructures, a critical strain or stress-strain product was necessary to describe the cleavage fracture process.

Cleavage in pearlite has been shown to follow the {100} planes of ferrite (Alexander and Bernstein 1982). Park and Bernstein (1979) have argued that the cleavage facet in pearlite constitutes an effective grain size in which the {100} planes of ferrite are closely aligned. This unit was shown to be strongly related to the prior austenite grain size. The unusual feature of this effective grain size is that it cannot be determined independently. It has to be related to the cleavage facet size which is in turn controlled by the prior austenite grain size, despite the fact that there are no austenite grains at the test temperature! It is evident therefore, that further work needs to be done to clarify the dependence of fracture facet size on the microstructure.

### 3.7 Aspects of Cleavage fracture covered by the present research

The objectives of this research will be to draw attention to the following:

(i) Identifying the micromechanism of cleavage fracture in pearlitic steels.

(ii) Identifying the microstructural variables which control the cleavage fracture stress $\sigma_f$ in pearlite.

(iii) Identifying the temperature dependence of $\sigma_f$.

(iv) Attempting to identify the differences in modes of fracture between fine and coarse pearlite.

(v) Identifying the microstructural variable that controls the size of cleavage fracture facets.

(vi) Identifying the micromechanism of cleavage fracture in medium-high carbon hypoeutectoid steels.

# 4. EXPERIMENTAL TECHNIQUES

## 4.1 Material used

The chemical compositions of the two rail steels used in this investigation are given in table 4.1. The eutectoid steel conformed to BS 11 grade A specification, and was supplied as a 90 lb/yd (45 kg/m) rail beam. The hypoeutectoid steel was supplied in plate form.

**Table 4.1** Chemical composition of rail steels used (wt.%).

| | C | Si | Mn | P | S |
|---|---|---|---|---|---|
| Eutectoid | 0.75 | 0.23 | 1.12 | 0.023 | 0.026 |
| Hypoeutectoid | 0.58 | 0.21 | 0.75 | 0.031 | 0.034 |

## 4.2 Heat treatment

Heat treatment was performed so that microstructural variables such as prior austenite grain size, pearlite nodule size, pearlite colony size, pearlite interlamellar spacing and ferrite grain size could be altered as required. Table 4.2(a) gives the heat treatment sequence for the eutectoid steel. Specimens were extracted from the web of the rail, and heat treated before final machining.

The objective of the series A specimens was to produce a wide variation in prior austenite grain size whilst maintaining a fairly constant interlamellar spacing. These specimens were austenitized in an argon atmosphere inside a muffle furnace and then isothermally transformed in a fluidized bed held at a temperature of 510 °C. Apart from specimen A1, all the specimens in this series were expected to have austenite grains ranging from medium coarse (1 hour at 900 °C) to very coarse (2 hours at 1200 °C). The cyclic heat treatment of specimen A1 consisted of 1 hour austenitizing at 750 °C followed by air cooling. The specimen was then reaustenitized at 750 °C for half an hour and then quenched into a fluidized bed held at 300 °C. At this stage the specimen had a fine bainitic microstructure. From this condition, the specimen was

reheated to 750 °C, held for half an hour, and then isothermally transformed to pearlite inside the fluidized bed. This cyclic treatment was adopted after the work of Grange (1971), and was expected to produce a very fine austenite grain size.

The objective of the series B specimens was to produce a range of fine austenite grains by selecting short austenitising times and low austenitising temperatures. The specimens were austenitized and transformed in salt baths to take advantage of the better heat transfer coefficient of molten salts. The objective of the series S specimens was to produce a large variation in pearlite interlamellar spacing and maintain a constant prior austenite grain size. The specimens were austenitized at 900 °C and transformed at different temperatures. Specimen S3 which was furnace cooled at a rate of 1.6 °C per minute was expected to produce the coarsest pearlite spacing.

Table 4.2(b) shows the sequence of heat treatment for the hypoeutectoid steel. Specimens were designated with the letter H, and were subjected to heat treatments similar to those given in table 4.2(a). All specimens were austenitized and transformed in salt baths except specimens H5, H6, H7 and H11. These were austenitized in a muffle furnace and then transformed in a fluidized bed, except specimen H11 which was furnace cooled at a rate of 1.6 °C per minute. An argon atmosphere was maintained in the muffle furnace throughout the heat treatment. Specimens H1 to H7 were designed to produce a wide variation in prior austenite grain size whilst maintaining a fairly constant interlamellar spacing. Specimens H8 to H11 were designed to produce a variation in interlamellar spacing since they were transformed at different temperatures.

## 4.3 Plane strain fracture toughness.

### 4.3.1 Specifications for the test.

The plane strain fracture toughness $K_{IC}$ was determined according to British standard BS 5447: 1977. The standard requires the determination of a provisional value of $K_{IC}$, designated $K_Q$, and then checking the validity of that value. If the test is valid, then $K_Q$ is taken to be equal to $K_{IC}$. In this investigation, bend specimens were adopted. The specimen

**Table 4.2** Heat treatment sequencies

(a) The Eutectoid Steel

| Specimen | Austenitising Condition | | Transformation Condition | |
|---|---|---|---|---|
| | Temp. °C | Time | Temp. °C | Medium |
| A1 | 750 | cyclic | 510 | FB |
| A2 | 900 | 1 hr | 510 | FB |
| A3 | 1000 | 1 hr | 510 | FB |
| A4 | 1200 | 1 hr | 510 | FB |
| A5 | 1200 | 2 hrs | 510 | FB |
| B1 | 800 | 15 min | 510 | SB |
| B2 | 850 | 15 min | 510 | SB |
| B3 | 900 | 15 min | 510 | SB |
| B4 | 900 | 1 hr | 510 | SB |
| S0 | As B4 | | As B4 | |
| S1 | 900 | 1 hr | 580 | SB |
| S2 | 900 | 1 hr | 650 | SB |
| S3 | 900 | 1 hr | 1.6 °C/min | FC |
| AR | As received condition | | | |

(b) The Hypoeutectoid Steel

| Specimen | Austenitising Condition | | Transformation Condition | |
|---|---|---|---|---|
| | Temp. °C | Time | Temp. °C | Medium |
| H1 | 800 | 15 min | 510 | SB |
| H2 | 850 | 15 min | 510 | SB |
| H3 | 900 | 15 min | 510 | SB |
| H4 | 900 | 1 hr | 510 | SB |
| H5 | 1000 | 1 hr | 510 | FB |
| H6 | 1100 | 1 hr | 510 | FB |
| H7 | 1200 | 1 hr | 510 | FB |
| H8 | As H4 | | As H4 | |
| H9 | 900 | 1 hr | 580 | SB |
| H10 | 900 | 1 hr | 650 | SB |
| H11 | 900 | 1 hr | 1.6 °C/min | FC |
| HR | As received condition | | | |

FB (fluidised bed), SB (salt bath), FC (furnace cooled).

width W, and the thickness B, are related such that B = 1/2 W. Test specimens are required to be fatigue precracked at the bottom of the machined notch after all heat treatments have been done. The length of the fatigue crack has to be at least 1.25 mm, and should be such that the a/W ratio, as measured after fracture is in the range 0.45 - 0.55.

During the test, the crack opening displacement is recorded as a function of applied load, P, using a clip gauge. From the plot, the fracture load $P_Q$ is read off, and used to calculate $K_Q$. For plain strain conditions, the size of the plastic zone at fracture must be very small compared to the specimen dimensions. Both B and a must in fact exceed 50 $r_p$, where $r_p$ is the size of the plastic zone ahead of the crack tip (Knott, 1973). From this it follows:

$$a \geq 2.5\ (K_{IC}/\sigma_y)^2 \leq B \qquad (4.1)$$

The provisional plane strain fracture toughness $K_Q$ for a three-point bend geometry is given by the expression:

$$K_Q = \frac{3P_Q L}{BW^{3/2}}[1.93(a/W)^{1/2} - 3.07(a/W)^{3/2} + 14.53(a/W)^{5/2} - 25.11(a/W)^{7/2} + 25.80(a/W)^{9/2}] \qquad (4.2a)$$

For the standard test piece geometry, L = 2W, the half loading span, and $K_Q$ is given by the following expression:

$$K_Q = \frac{P_Q . Y_1}{B . W^{1/2}} \qquad (4.2b)$$

where $Y_1$ is the polynomial function in equation 4.2a whose value depends on the ratio a/W. Values of $Y_1$ against a/W are given in Appendix 1.

When a specimen has been broken, the crack length is determined as the average of measurements taken at 25% B, 50% B and 75% B. The difference between any two of these measurements must not exceed 2.5% W. The difference between the maximum and minimum crack lengths in any specimen must not exceed 5% W.

### 4.3.2 Procedures used to determine $K_{IC}$

The $K_{IC}$ specimens were fatigue precracked at room temperature using a Mayes servo hydraulic testing machine. The test frequency was 15 Hz. The machine was operated in the compressive mode. The extension of the fatigue crack was monitored by means of a travelling telescope.
After precracking, specimens were loaded to fracture in 4-point bending.
Test temperatures of -80 °C for the eutectoid steel and -100 °C for the hypoeutectoid steel were selected because a relatively low temperature was required to ensure that the cleavage fracture specimens would fracture prior to general yield. A test rig incorporating a cooling chamber was therefore constructed for these tests. The rig was attached to an Instron screw driven machine that was operated at a cross head speed of 0.1 mm/minute. A mixture of liquid nitrogen and ethyl alcohol provided the coolant whose temperature was maintained to ± 2 °C.

Since the $K_{IC}$ specimens were loaded in four point bending, the compliance, $Y_1$, in equation 4.2b must be modified to account for the differences in loading geometry. Appendix 2 shows the modified expression which was used to calculate $K_Q$, namely

$$K_Q = \frac{P_Q.Y}{B.W^{1/2}} \qquad (4.3)$$

The values of the compliance Y, which are given in table 1 of Appendix 2, are approximately 53% the values of $Y_1$ for corresponding a/W ratios. Figure 4.1 shows the dimensions of the specimens used. The specimens were made longer than usual because tensile and cleavage fracture specimens were to be machined from the broken halves after testing. In this way it was possible to obtain $K_{IC}$, tensile, and cleavage data in specimens which had been subjected to exactly the same heat treatment conditions. All tests were performed in duplicate.

### 4.4 Cleavage fracture stress

The cleavage fracture stress ($\sigma_f$) was determined from single notched bend (SNB) specimens (figure 4.2(a)) using the specimen geometry and finite element analysis described by Griffiths and Owen (1971). In these tests a blunt notched specimen is broken in four point bending.

and the nominal bending stress $\sigma_{nom}$ is calculated. The level of the stress intensification R ahead of the notch depends on the nominal bending stress and the yield strength of the material. By calculating the ratio of the nominal bending stress to the yield stress, it is possible to obtain the stress intensification, and therefore the maximum principal stress $\sigma_{1max}$, using figure 4.3 taken from Griffiths and Owen (1971). The stress $\sigma_{1max}$ is then equal to $\sigma_f$. Figure 4.4 shows the variation of the maximum principal stress below the notch root at various loads. This figure is useful in predicting the possible location for crack nucleation in a blunt notched specimen.

Test temperatures for $\sigma_f$ were the same as those at which $K_{IC}$ was determined except when the temperature dependence of $\sigma_f$ was required, when tests were performed in the temperature range -25 to -196 °C. Specimens used for such tests were either normalized from 900 °C, or austenitized for 1 hour at 900 °C, and then isothermally transformed in a salt bath at 550 °C. All $\sigma_f$ specimens were tested in the Instron machine at a cross head speed of 0.2 mm/minute. Tests were performed in duplicate, and the temperature was maintained to ± 2 °C. Specimens were fully immersed in the coolant for at least 15 minutes before loading.

In order to understand the micromechanisms of cleavage fracture, it was necessary to study the early stages of crack nucleation. This was achieved using double notched bend (DNB) specimens (figure 4.2(b)) for some of the heat treatment conditions. This technique had been used previously by Lewandowski and Thompson (1984) to reveal similar information. When such specimens are loaded in pure bending, normally only one of the notches fails. The unbroken notch then represents the material immediately prior to the onset of unstable fracture. This material may contain non-propagating microcracks which can be exposed by suitable metallographic techniques.

### 4.5 Proof stress and ultimate tensile stress

The proof stress and ultimate tensile stress were performed on the Instron machine using either Hounsfield no. 13 specimens or compression specimens measuring 3x3x6 mm. Specimens made from the eutectoid steel did not display a yield point. For these specimens, the 0.2% proof

Figure 4.1 Dimensions of the $K_{IC}$ specimen

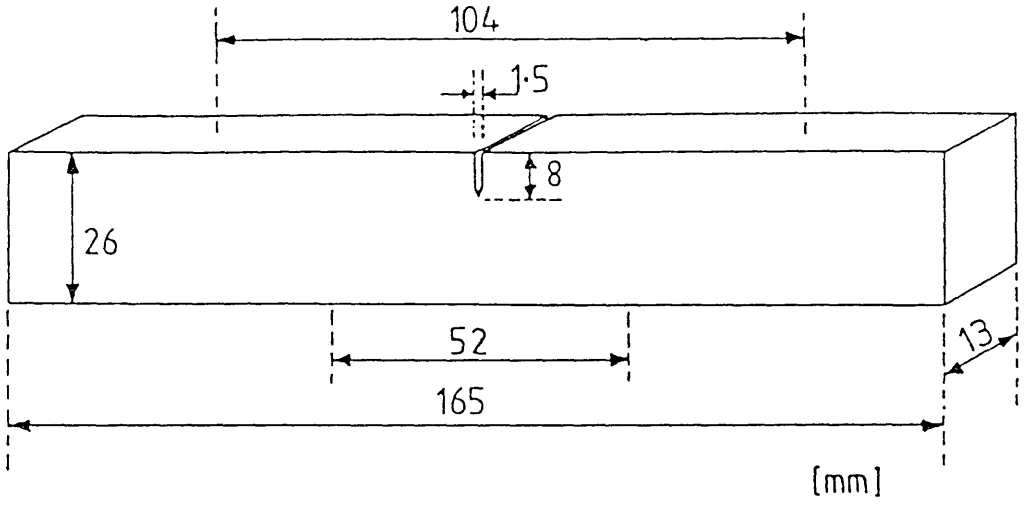



Figure 4.2(a) Dimensions of the single notched bend specimen (SNB)

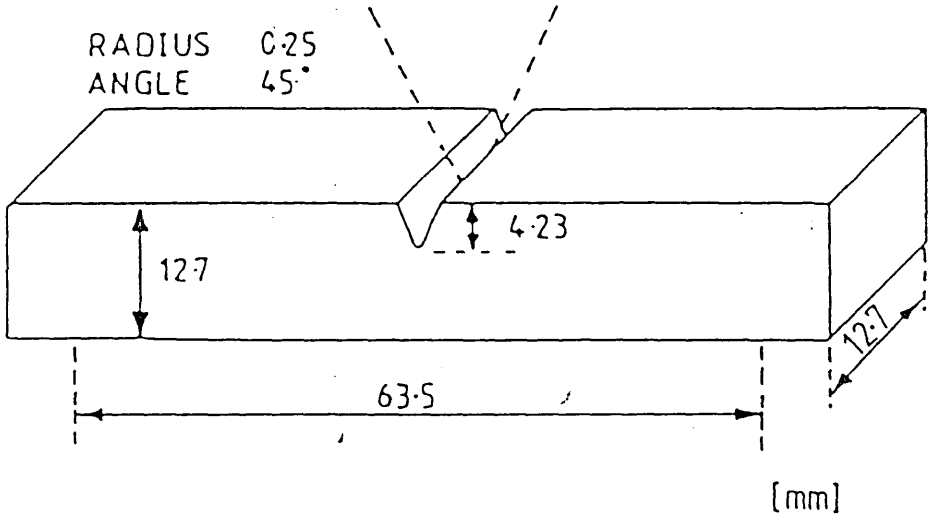



Figure 4.2(b) Dimensions of the double notched bend specimen (DNB)

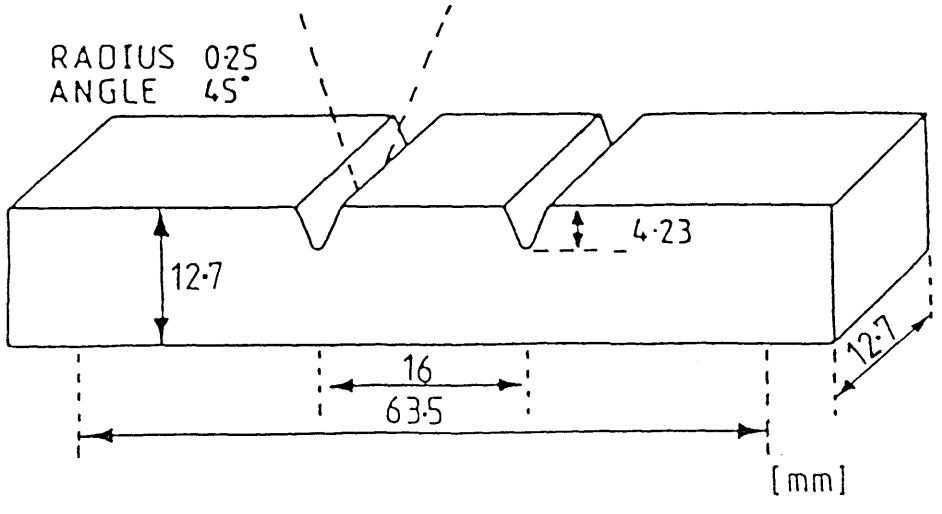


Figure 4.3 The variation of the stress intensification R with applied load in a 45° blunt notched specimen (Griffiths and Owen, 1971).

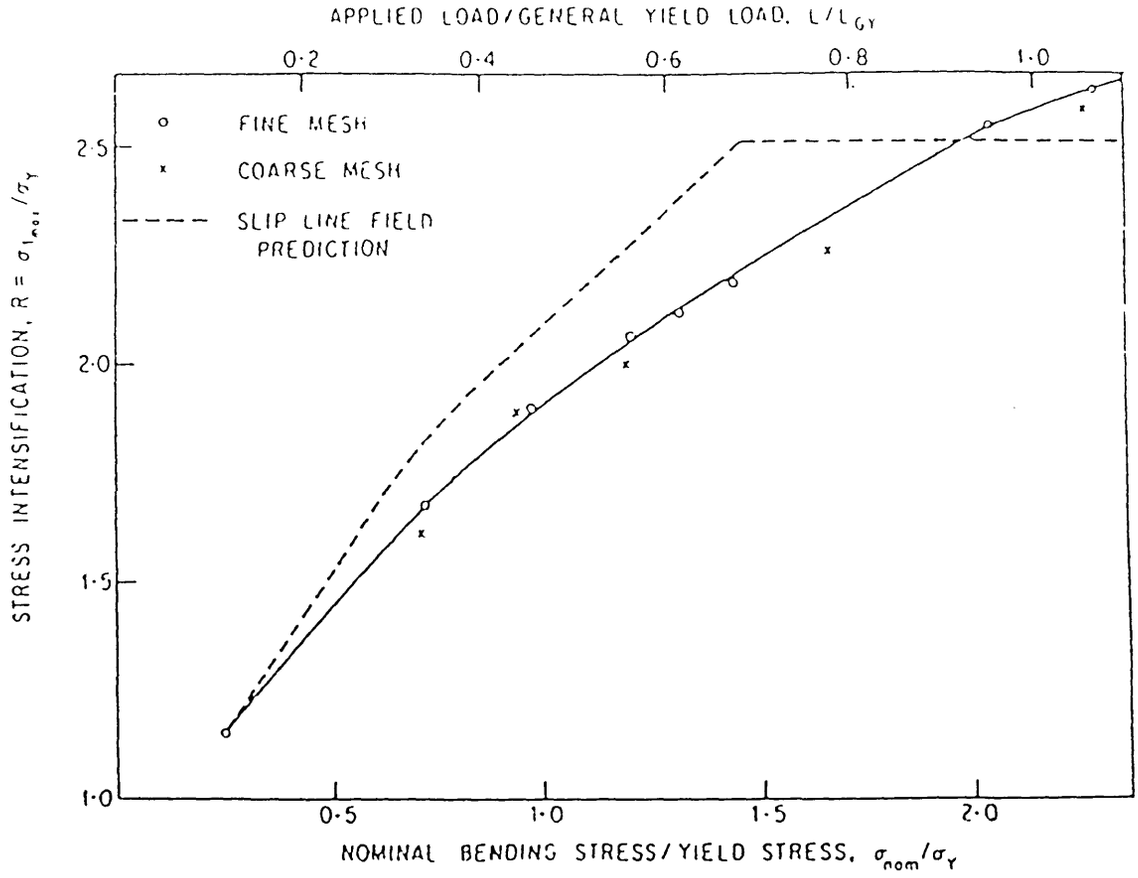
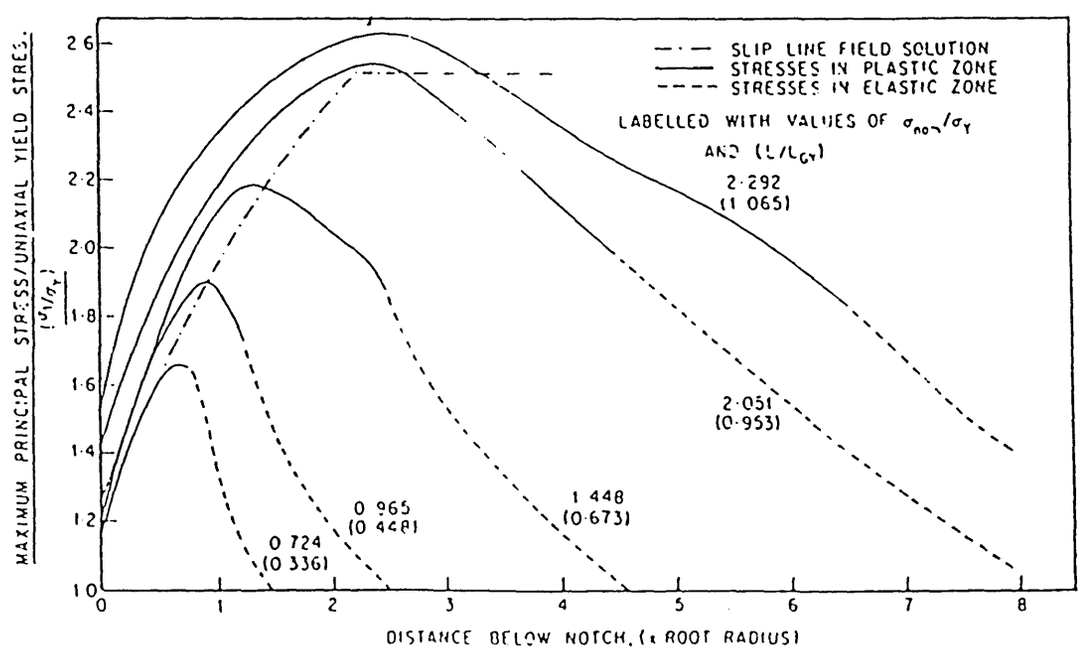



Figure 4.4 The variation of the maximum principal stress below the notch root at various loads (Griffiths and Owen, 1971).



stress was determined. Most of the specimens from the hypoeutectoid steel displayed a yield point, and therefore the lower yield stress was quoted. All the Hounsfield specimens were tested to fracture at a machine cross head speed of 0.2 mm/minute, and the ultimate tensile stress and the elongation to fracture $\delta$ were recorded. Some of the specimens with coarse austenite grains did not show necking instability, and so the maximum stress was taken to represent $\sigma_u$.

### 4.6 Quantitative metallography

#### 4.6.1 Prior austenite grain size

The prior austenite grain size of the eutectoid steel was determined on specimens measuring 12x12x12 mm. These specimens were austenitized for the same conditions as those given to the test specimens, but they were quenched in oil and then tempered at 510 °C for 16 hours to produce a tempered martensite structure. Microsections were prepared from the cube specimens and etched in boiling saturated aqueous picric acid for 1 minute. This was followed by a light polish on a quarter micron diamond polishing cloth after which the microsections were re-etched in the same reagent. The sequence was repeated with intermediate inspection until the austenite grain boundaries were fully developed (figure 4.5a). This technique has been used before by Hyzak and Bernstein (1976). The prior austenite grain size was then determined by a Bausch and Lomb "Ommicon 3000" image analysis system.

The prior austenite grain size of the hypoeutectoid steel was determined from microsections which had been prepared from the broken halves of the test specimens. After etching the microsections in 2% nital, the prior austenite grain boundaries were revealed by proeutectoid ferrite (figure 4.5b). The austenite grain boundaries were traced onto transparent film and the grain size determined by the image analyser. For some of the conditions, the grain size was also determined by the linear intercept method. Measurements by the linear intercept method correlated very well with those of the image analyser.

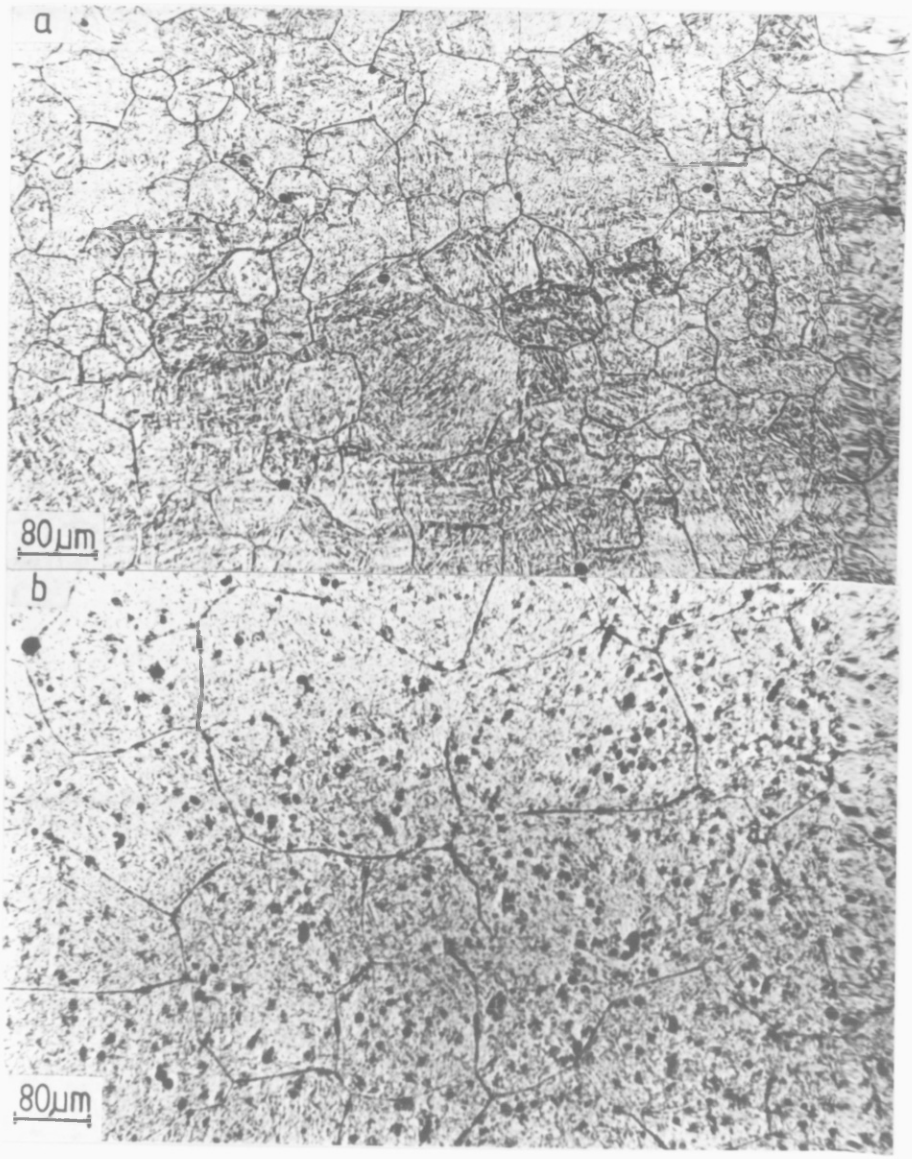



FIGURE 4.5(a)

Prior austenite grain boundaries in specimens which were austenitised for 1 hour at (a) 900 °C and (b) 1200 °C (eutectoid steel).

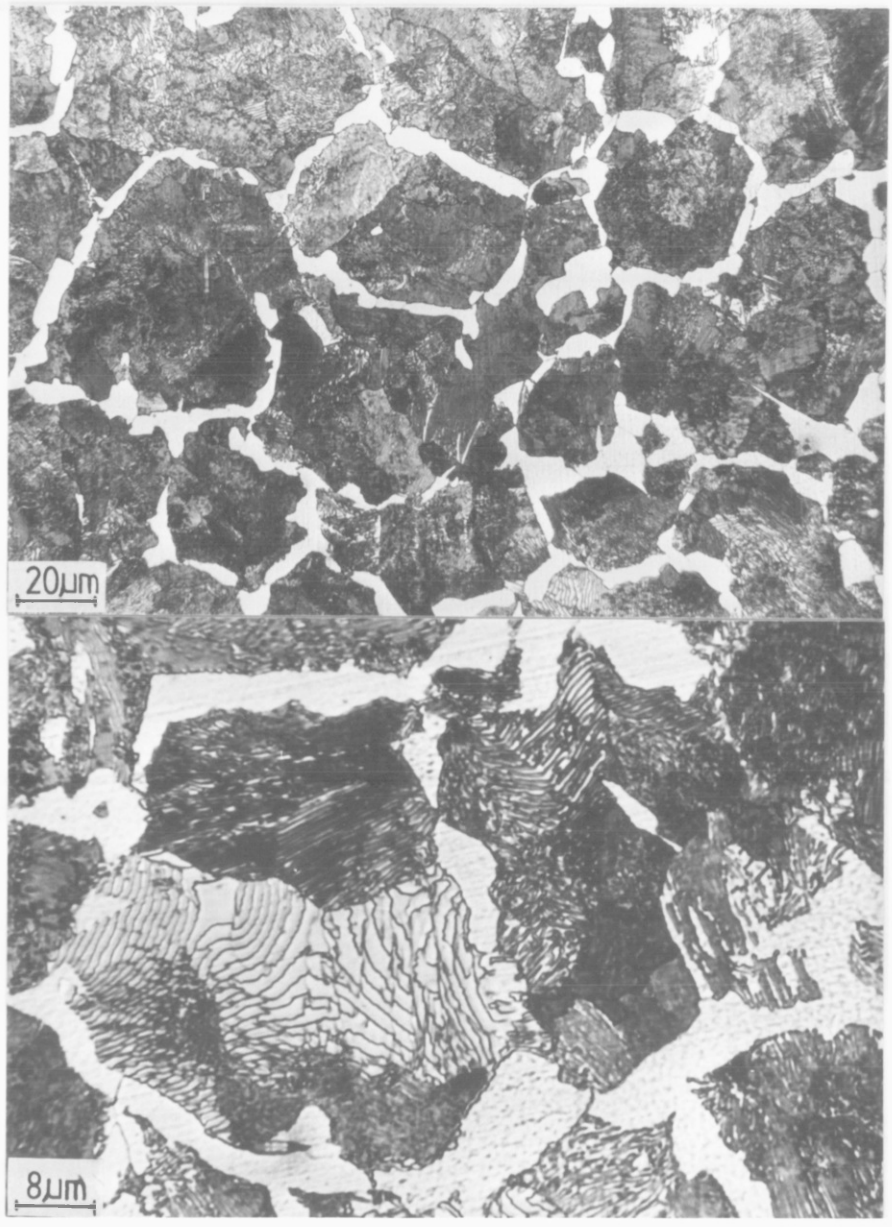



FIGURE 4.5(b)

Prior austenite grain boundaries outlined by proeutectoid ferrite in the hypoeutectoid steel (as received condition).

### 4.6.2 Pearlite nodule size and colony size

Microsections prepared from the broken halves of the test specimens and etched in 2% nital were used for these measurements. The pearlite nodule size was determined in an optical projection microscope using ASTM grain size charts. A comparator method was adopted due to the difficulty of tracing nodule boundaries in specimens which have been etched in nital. The nodule boundaries were always clearly revealed, but were hardly fully continuous. It was therefore not easy to trace out complete nodules, and apply a linear intercept measurement. The image analyser was also unsuitable because it requires that boundaries should clearly distinguish one grain from another.

The pearlite colony size was determined from micrographs obtained from a JEOL T200 scanning electron microscope (SEM). At a magnification of 2000X and above, pearlite colony boundaries are revealed. By tracing the boundaries onto a transparent film, it was possible to measure the colony size using the image analyser.

### 4.6.3 Pearlite interlamellar spacing and ferrite mean free distance

The pearlite interlamellar spacing was determined using a linear intercept method described by Underwood (1970). Microsections were examined in the scanning electron microscope at a magnification where the pearlite lamellae were fully resolved. A test line was applied randomly to the SEM screen, thus intersecting a large number of lamellae at all possible angles in the plane of polish. A mean random spacing, $S_r$, was obtained by dividing the total length of test line by the total number of alternate lamellae intersected. The mean free distance $\lambda$ in the pearlitic ferrite can be obtained by subtracting the thickness of cementite lamellae from the random spacing (Gensamer et al, 1942; O'Donnelly et al, 1984).

Lamellar structures are usually characterized by the mean true interlamellar spacing, $S_t$. This is the perpendicular distance across a single pair of contiguous lamellae. Underwood (1970) has shown that the true spacing is related to the random spacing through the expression:

$$S_t = S_r/2 \qquad (4.4)$$

In determining the pearlite spacings, about 200 fields of view were studied for each heat treatment condition. Two perpendicular test lines were kept fixed on the SEM screen, and the specimen stage was moved so that measurements were taken for every new field of view. The thickness of cementite lamellae, t, was calculated from the knowledge of the carbon content of the steel, $C_s$, and the interlamellar spacing, $S_t$, using the relationship:

$$t = 0.15 \times C_s \times S_t \qquad (4.5)$$

The thickness of ferrite lamellae $S_\alpha$ may be obtained by subtracting t from $S_t$. On the other hand, if t is calculated by using $S_r$, rather than $S_t$ in equation 4.5, then the ferrite mean free distance (mfd) in pearlite, $\lambda$, is obtained by subtracting t from $S_r$. The ferrite mfd represents an average distance over which dislocations may travel in the pearlitic ferrite without encountering an obstacle in the form of cementite lamellae. The mean free distance in proeutectoid ferrite, $\lambda_\alpha$, is related to both the volume fraction of proeutectoid ferrite ($V_\alpha$) and the prior austenite grain size $\gamma$. It is given by equation 4.6 (O'Donnelly et al, 1984).

$$\lambda\alpha = (1-V_\alpha)(S_r-t) + (V_\alpha)^2\gamma \qquad (4.6)$$

## 4.7 Fractography

The fracture surfaces of all the $K_{IC}$ and $\sigma_f$ specimens were protected with a clear lacquer immediately after fracture. Selected fracture surfaces were later ultrasonically cleaned in acetone and then studied in the SEM. Some of the fracture surfaces were etched in 2% nital so that the pearlitic microstructure could be related to fracture facets.

The fracture path was studied by nickel plating fractured samples and preparing microsections from sections taken perpendicular to the plated surface. The microsections were etched in 2 % nital and studied in the SEM. The nickel plating solution was prepared by dissolving 350 g of Nivo nickel salt in distilled water to make 1 litre of solution. The current density was 10 $mA/cm^2$, and the plating time was 48 hours.

# 5. RESULTS FROM THE EUTECTOID STEEL

## 5.1 The microstructure

Figure 5.1 shows different stages in the development of a pearlite nodule. The specimen was partially transformed to pearlite and then quenched in oil to allow the matrix austenite to transform to martensite. Figures 5.1 (b) and (d) show parts of the austenite boundaries on which the nucleation took place. Whilst in figure 5.1 there are no nodule boundaries because impingement is not complete, in figure 5.2 fully developed boundaries can be seen in a specimen which was completely transformed into pearlite. The micrographs were taken in a scanning electron microscope, and as such the black lamellae are ferrite and the white lamellae are cementite.

Figure 5.3(a) shows the microstructure of the eutectoid steel in the as-received condition. Figure 5.3(b) shows the microstructure of specimens which were austenitised at 900 and 1200 °C respectively, and then isothermally transformed to pearlite. It can be seen that the steel is almost fully pearlitic, the amount of proeutectoid ferrite being only about 1%. Figure 5.4(a) shows the microstructure of specimens which were transformed at different temperatures. Clearly the specimen which was transformed at the higher temperature (650 °C) had the coarser pearlitic microstructure. Figure 5.4(b) shows a specimen which has undergone slight decarburization so that proeutectoid ferrite is revealed. The micrograph shows the three grain-like parameters investigated, namely prior austenite grains, pearlite colonies and pearlite nodules.

The effect of the various heat treatment conditions on the microstructural parameters is shown in table 5.1. It can be seen in the series A specimens that the progressive increase in prior austenite grain size is accompanied by a similar increase in the pearlite nodule size. The pearlite colony size and the pearlite interlamellar spacing showed very small variation with austenite grain size. In the series B specimens the pearlite nodule size also increases with austenite grain size whilst the other pearlite parameters remain nearly constant. Since these specimens were transformed in molten salt baths, they had interlamellar spacings which were finer than those of the series A specimens. Specimen A1

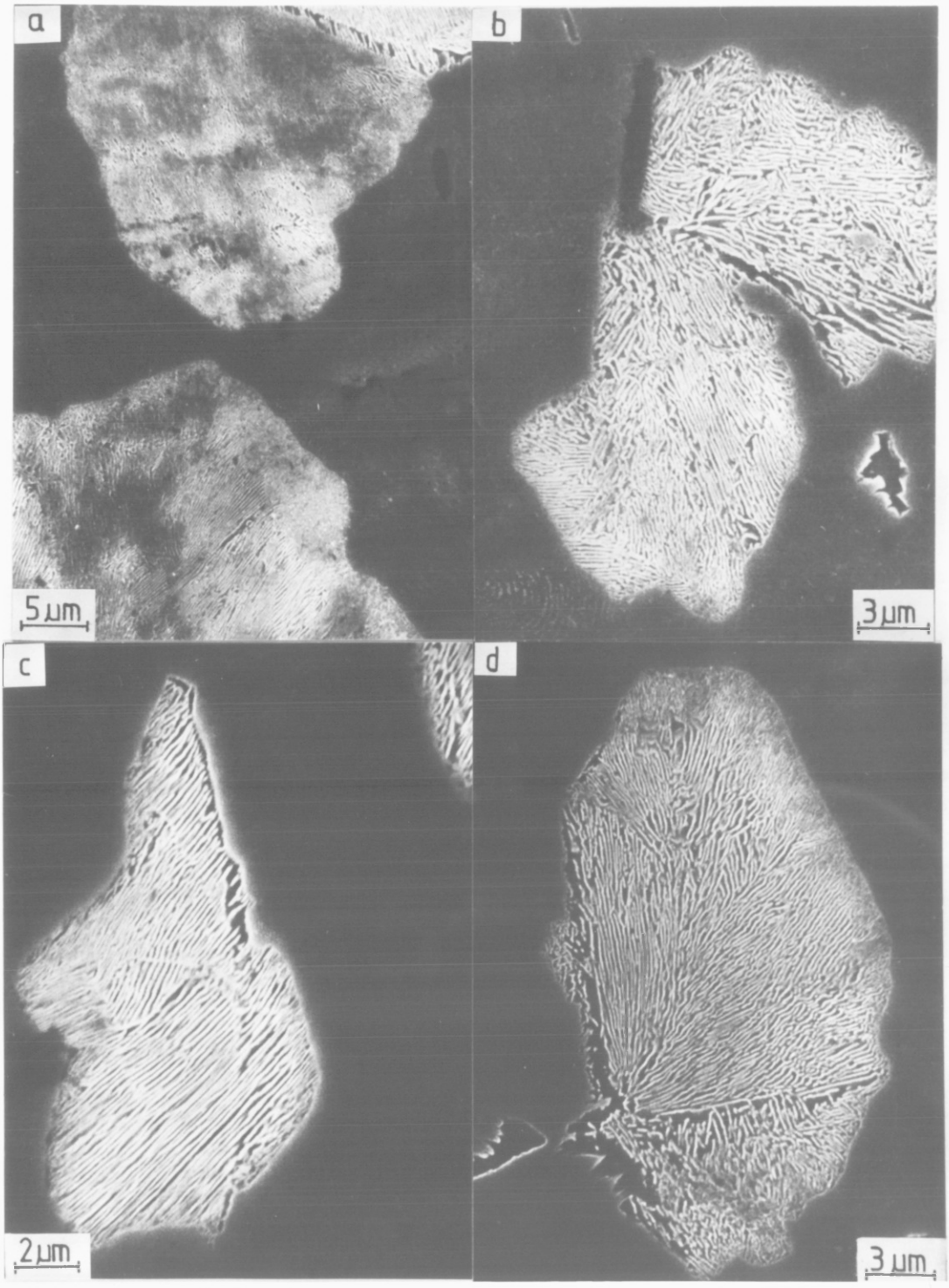



FIGURE 5.1

Different stages in the nucleation of pearlite; (a) two nodules about to impinge, (b) partly impinged nodules, (c) and (d) isolated nodules consisting of several colonies.




FIGURE 5.2

Three impinging pearlite nodules in specimens which were austenitised at (a) 1200 °C and (b) 1000 °C and transformed in a fluidised bed at 510 °C.

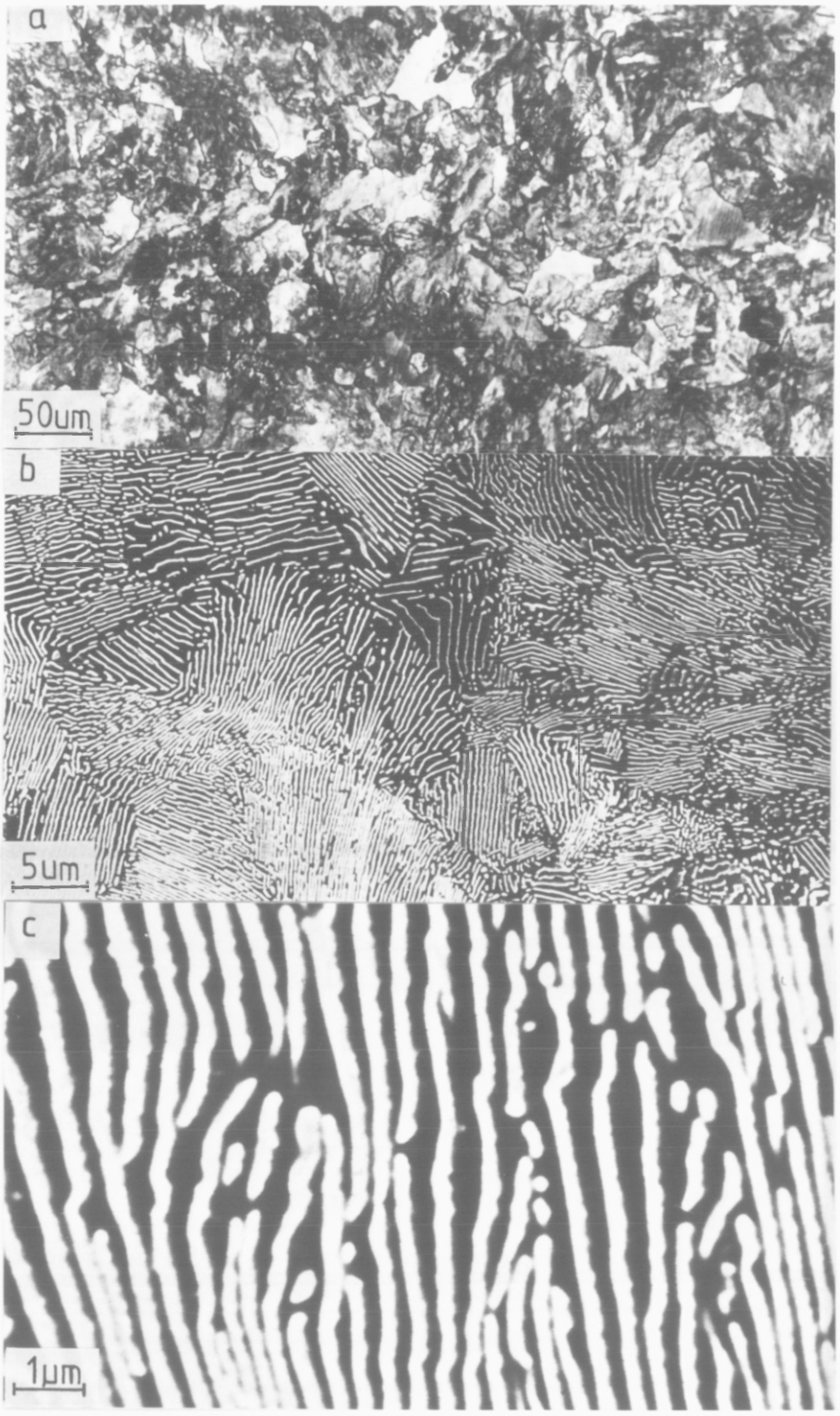



FIGURE 5.3(a)

The microstructure of the fully pearlitic steel in the as-received condition. Photo (a) shows pearlite nodules where the nodule boundaries are the black outline. Photo (b) shows pearlite colonies and photo (c) pearlite lamellae where the white lamellae are cementite.

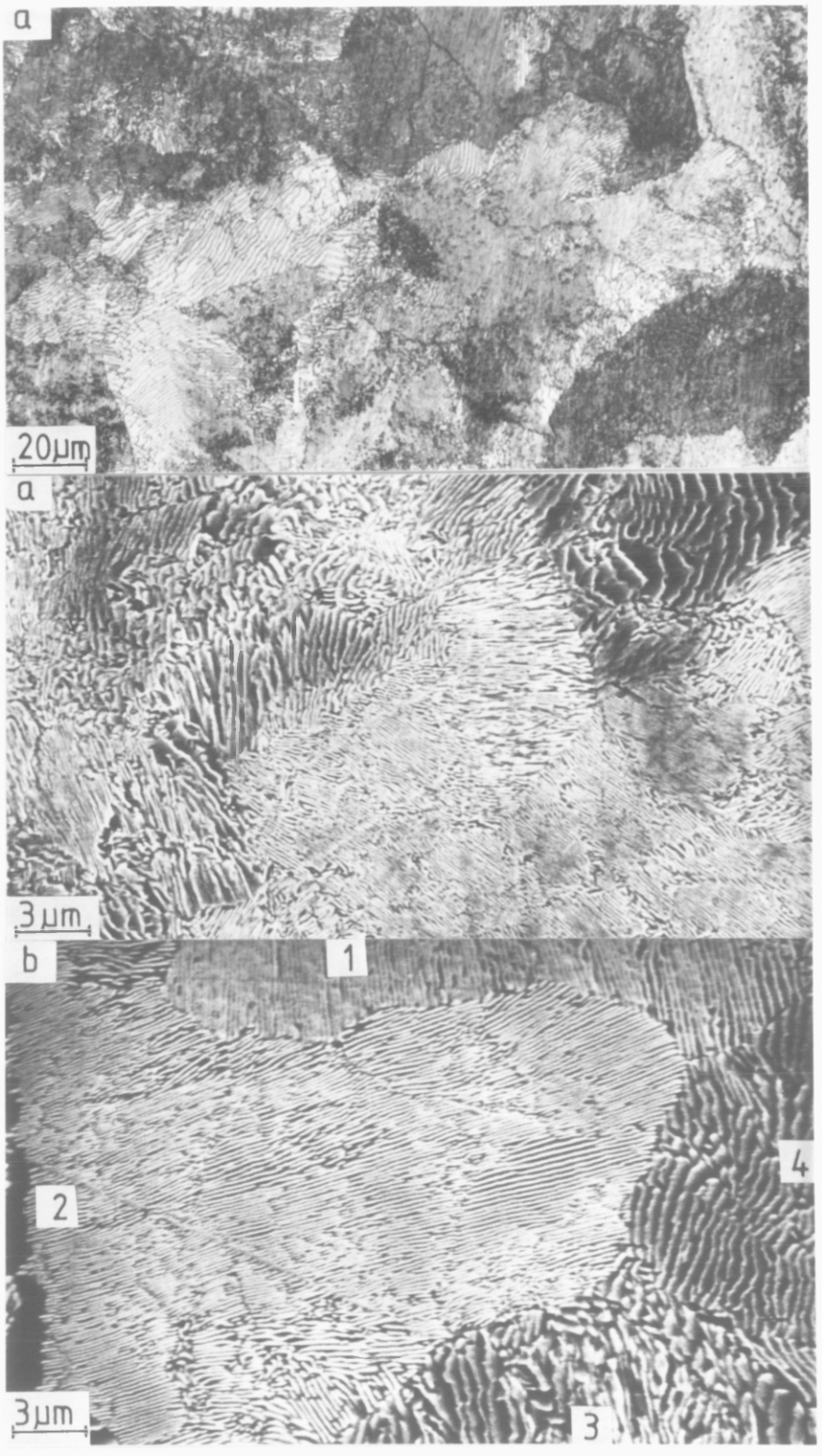



FIGURE 5.3(b)

The microstructures of specimens austenitised at (a) 900 °C and (b) 1200 °C and transformed in a fluidised bed at 510 °C. Four pearlite nodules can be distinguished in (b) (numbered 1-4).

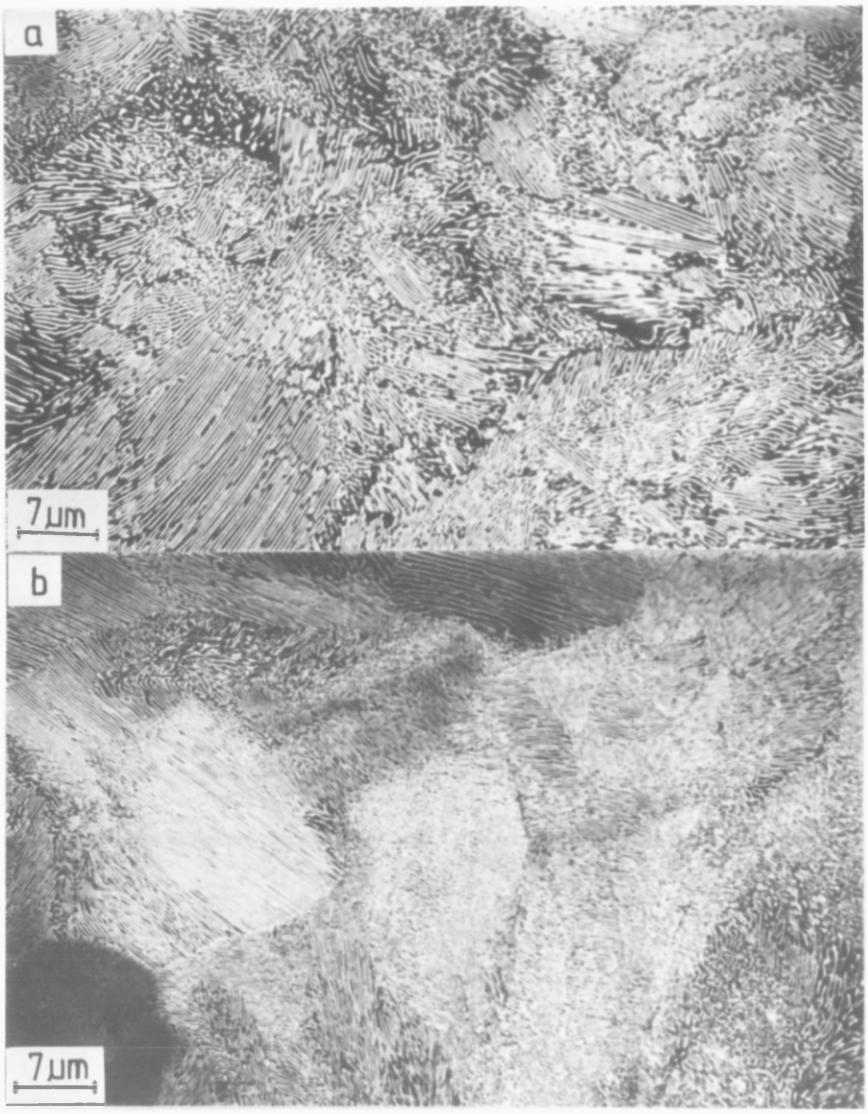



FIGURE 5.4(a)

The microstructures of specimens transformed at (a) 650 °C (salt bath) to give a coarse pearlite and (b) 510 °C (fluidised bed) to give a fine pearlite.

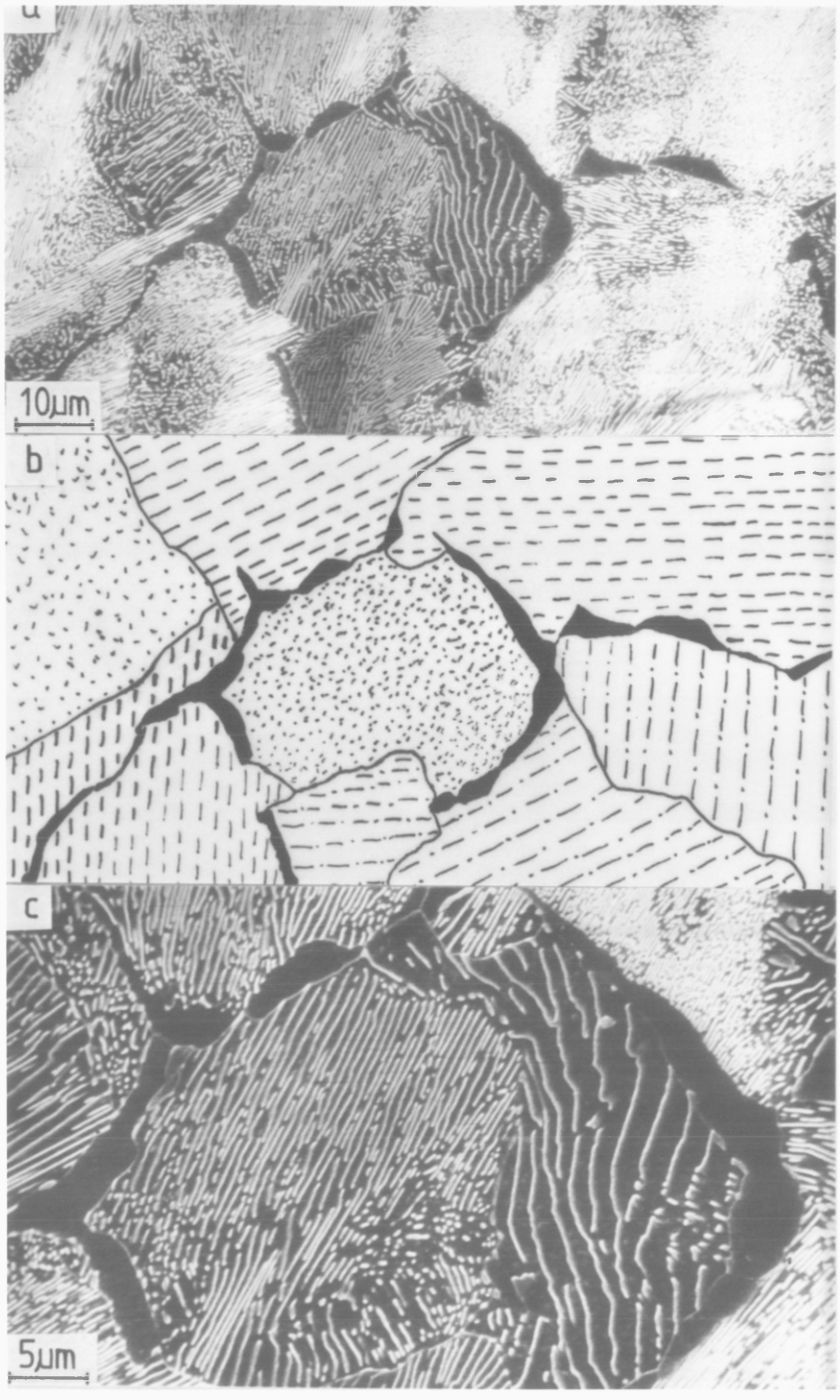



FIGURE 5.4(b)

Proeutectoid ferrite (black outline) along prior austenite grain boundaries in a specimen transformed at 650 °C. Photo (a) shows a single pearlite nodule occupying almost the whole of the austenite grain at the centre. Photo (c) shows that the nodule consists of at least 3 colonies. The nodules in (a) have been illustrated by different shades in (b). Since (a) and (c) are SEM micrographs, nodule boundaries appear as a white outline.

**Table 5.1 Microstructural parameters measured from the eutectoid steel**

| Specimen | $\gamma$ μm | $S_t$ μm | $S_r$ μm | C μm | N μm | λ μm | t μm |
|---|---|---|---|---|---|---|---|
| A1 | 15 | - | - | - | - | - | - |
| A2 | 45 | 0.16 | 0.32 | 10.0 | 48 | 0.28 | 0.018 |
| A3 | 84 | 0.18 | 0.36 | 11.0 | 80 | 0.32 | 0.020 |
| A4 | 350 | 0.15 | 0.30 | 9.5 | 135 | 0.26 | 0.017 |
| A5 | 400 | 0.16 | 0.32 | 10.5 | 160 | 0.28 | 0.018 |
| B1 | 15 | 0.13 | 0.26 | 4.1 | 14 | 0.24 | 0.015 |
| B2 | 22 | 0.12 | 0.24 | 4.8 | 20 | 0.22 | 0.014 |
| B3 | 31 | 0.12 | 0.24 | 4.9 | 28 | 0.22 | 0.014 |
| B4 | 45 | 0.10 | 0.20 | 4.6 | 40 | 0.18 | 0.011 |
| S0 | 45 | 0.10 | 0.20 | 4.6 | 40 | 0.18 | 0.011 |
| S1 | 45 | 0.19 | 0.38 | 8.0 | 40 | 0.34 | 0.021 |
| S2 | 45 | 0.26 | 0.52 | 12.5 | 56 | 0.46 | 0.029 |
| S3 | 45 | 0.33 | 0.66 | 14.0 | 80 | 0.58 | 0.037 |
| AR | 48 | 0.21 | 0.42 | 10.0 | 40 | 0.38 | 0.024 |

$\gamma$ - prior austenite grain size; $S_t$ - mean true interlamellar spacing; $S_r$ - random interlamellar spacing; C - pearlite colony size; N - nodule size; λ - ferrite mfd; t - thickness of cementite lamellae.

appeared to have undergone incomplete austenitization prior to transformation to pearlite. This was attributed to insufficient austenitising conditions. The microstructure of this specimen was a mixture of lamellar pearlite and spherodized pearlite, and therefore none of the pearlite parameters was determined. In the series S specimens, the increase in interlamellar spacing with increasing transformation temperature is accompanied by an increase in both colony size and nodule size. In addition, we observe an increase in the ferrite mfd and thickness of cementite lamellae.

## 5.2 Mechanical properties

Table 5.2 shows the mechanical properties determined for each heat treatment condition. Each of the values quoted is a mean from duplicate tests. All the $\sigma_f$ specimens failed before general yield and therefore the ratio of the nominal bending stress to the uniaxial yield stress did not exceed 2.1 (see figure 4.3). This meant the ratio of the applied load to the general yield load was always less than 1.

All the $K_{IC}$ results were valid. Most of the series A and B specimens exhibited at least one pop-in before fracture occured. In the series S specimens pop-ins were very rare. The fracture load was determined by the 5 % off-set method. In the series A and B specimens, this corresponded to the first pop-in load, but in the series S specimens the fracture load was almost always the maximum load.

## 5.3 The effect of austenitising conditions on mechanical properties

The dominant microstructural parameter which varied with austenitising condition was the prior austenite grain size $\gamma$. The prior austenite grain size was therefore used to compare the effects of varying austenitising conditions on mechanical properties although other properties like nodule size and interlamellar spacing also changed. The effect of prior austenite grain size on proof stress $\sigma_{0.2}$, ultimate tensile stress $\sigma_u$ and cleavage fracture stress $\sigma_f$ is shown in table 5.2 and in figures 5.5a and 5.6. The data in figure 5.5a came from the series A specimens. The data in the fine-grain regime (figure 5.6) were obtained from the series B

**Table 5.2 Mechanical properties of the eutectoid steel determined at -80 °C**

| Specimen | Condition | $\sigma_{0.2}$ MN/m$^2$ | $\sigma_u$ MN/m$^2$ | $\sigma_f$ MN/m$^2$ | $\delta$ % | $K_{IC}$ MN/m$^{3/2}$ |
|---|---|---|---|---|---|---|
| A1 | Variation | 494 | 924 | 1205 | 20.0 | 27.9 |
| A2 | of $\gamma$ | 676 | 1176 | 1575 | 15.7 | 27.7 |
| A3 | (FB specimens) | 618 | 1961 | 1480 | 12.0 | 30.3 |
| A4 | | 717 | 1081 | 1658 | 4.7 | 30.6 |
| A5 | | 694 | 982 | 1527 | 3.6 | 30.4 |
| B1 | Variation | 721 | 1194 | 1803 | 17.4 | 29.1 |
| B2 | of $\gamma$ | 748 | 1200 | 1907 | 16.4 | 27.6 |
| B3 | (SB Specimens) | 754 | 1174 | 1885 | 17.6 | 34.9 |
| B4 | | 818 | 1259 | 1955 | 15.0 | 28.9 |
| S0 | Variation | 818 | 1259 | 1955 | 15.0 | 28.9 |
| S1 | of $S_t$ | 630 | 1096 | 1488 | 17.1 | 25.1 |
| S2 | | 546 | 991 | 1325 | 15.9 | 29.8 |
| S3 | | 519 | 979 | 1249 | 10.1 | 34.5 |
| AR | As received | 573 | 994 | 1406 | 7.2 | 26.5 |

$\sigma_{0.2}$ - proof stress, $\sigma_u$ - ultimate tensile stress, $\delta$ - elongation at fracture, $K_{IC}$ - plane strain fracture toughness,
FB - fluidised bed, SB - salt bath.

Figure 5.5a The effect of prior austenite grain size $\gamma$ on the proof stress $\sigma_{0.2}$, ultimate tensile stress $\sigma_u$, and the cleavage fracture stress $\sigma_f$ for the isothermally transformed specimens tested at −80 °C.

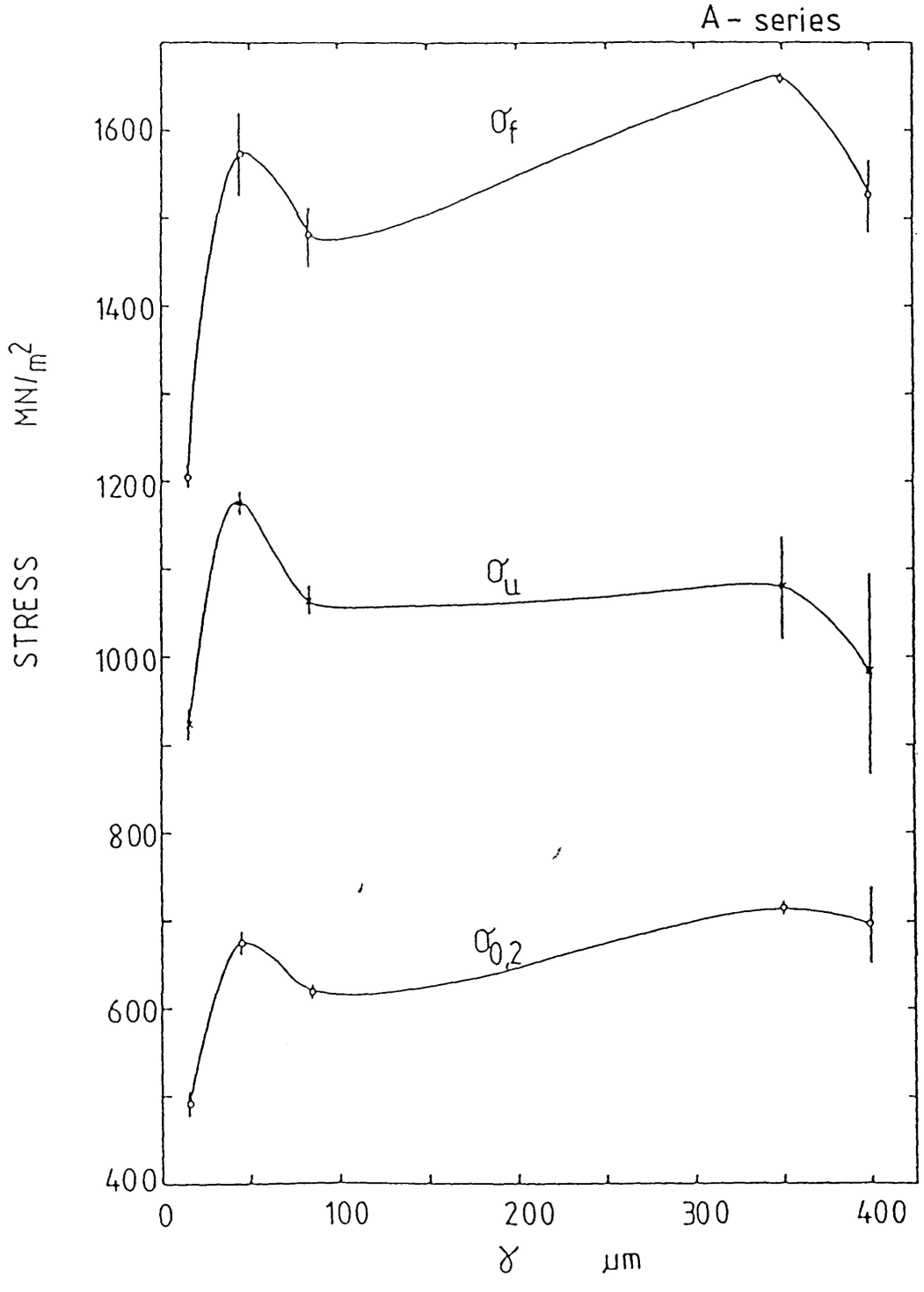


**Figure 5.5b** The effect of austenitising temperature on the proof stress $\sigma_{0.2}$, ultimate tensile stress $\sigma_u$ and % elongation at fracture $\delta$ for the normalised specimens tested at room temperature.

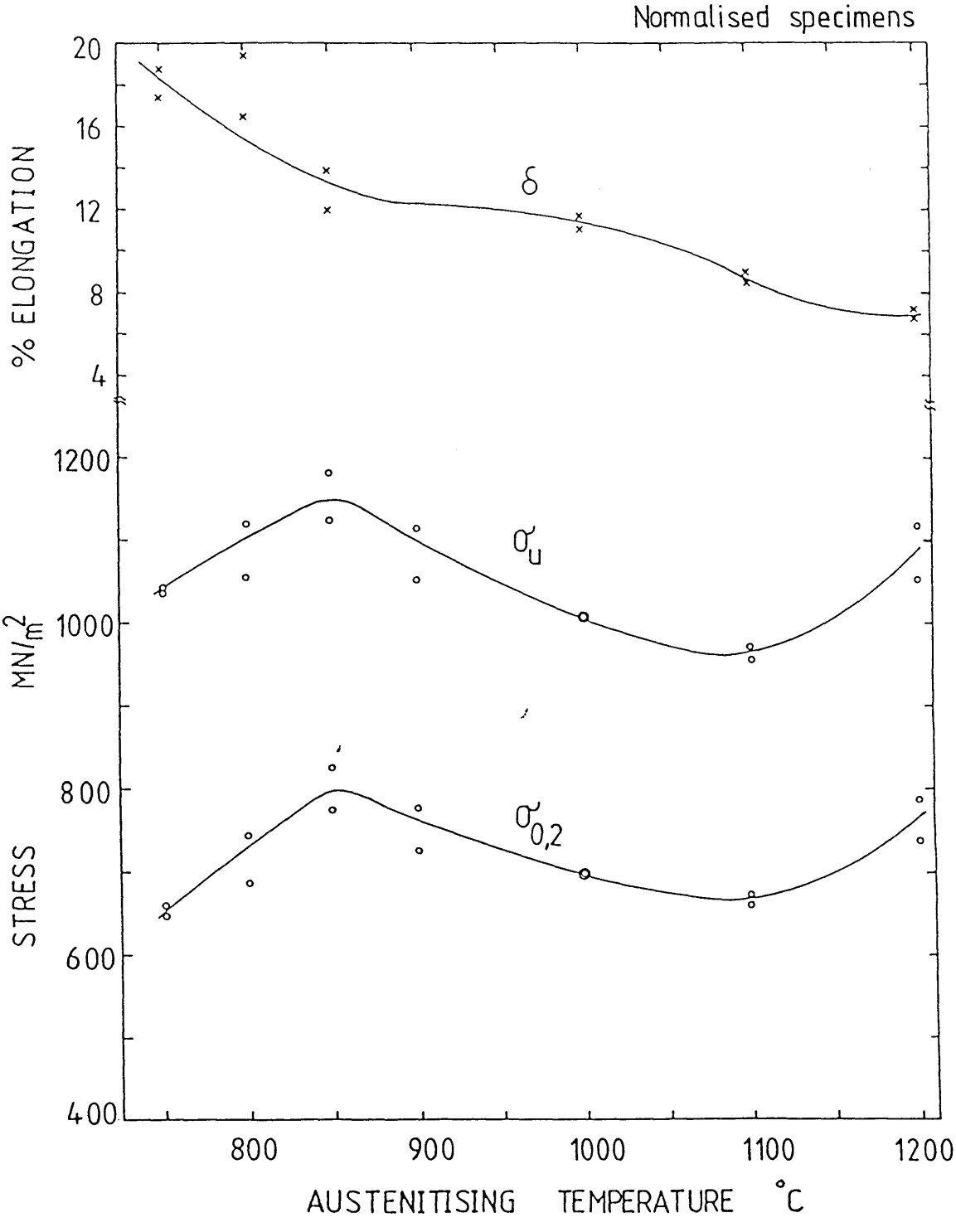
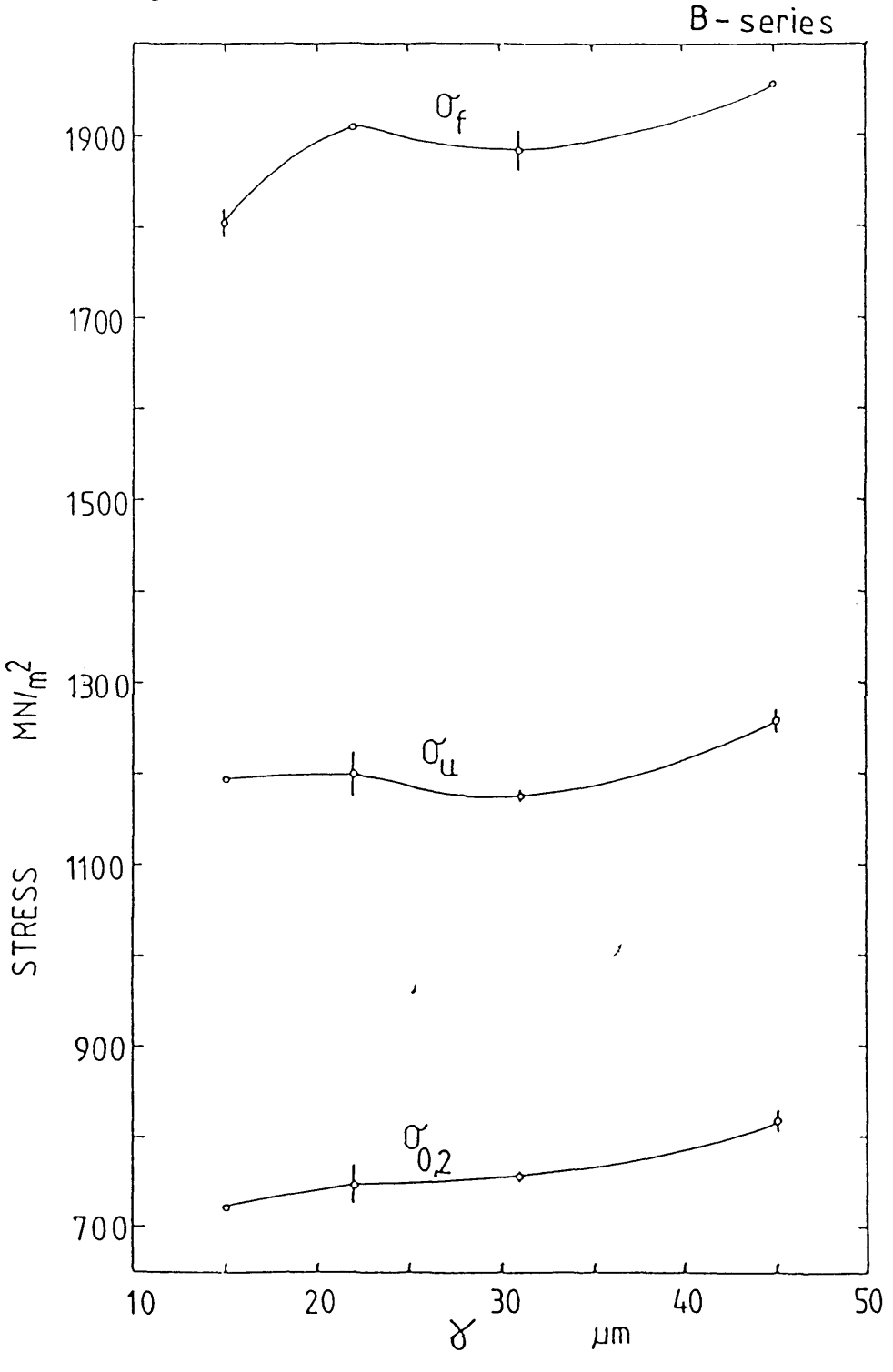


**Figure 5.6** The effect of prior austenite grain size $\gamma$ on the proof stress $\sigma_{0.2}$, ultimate tensile stress $\sigma_u$, and the cleavage fracture stress $\sigma_f$ in the fine grain regime.



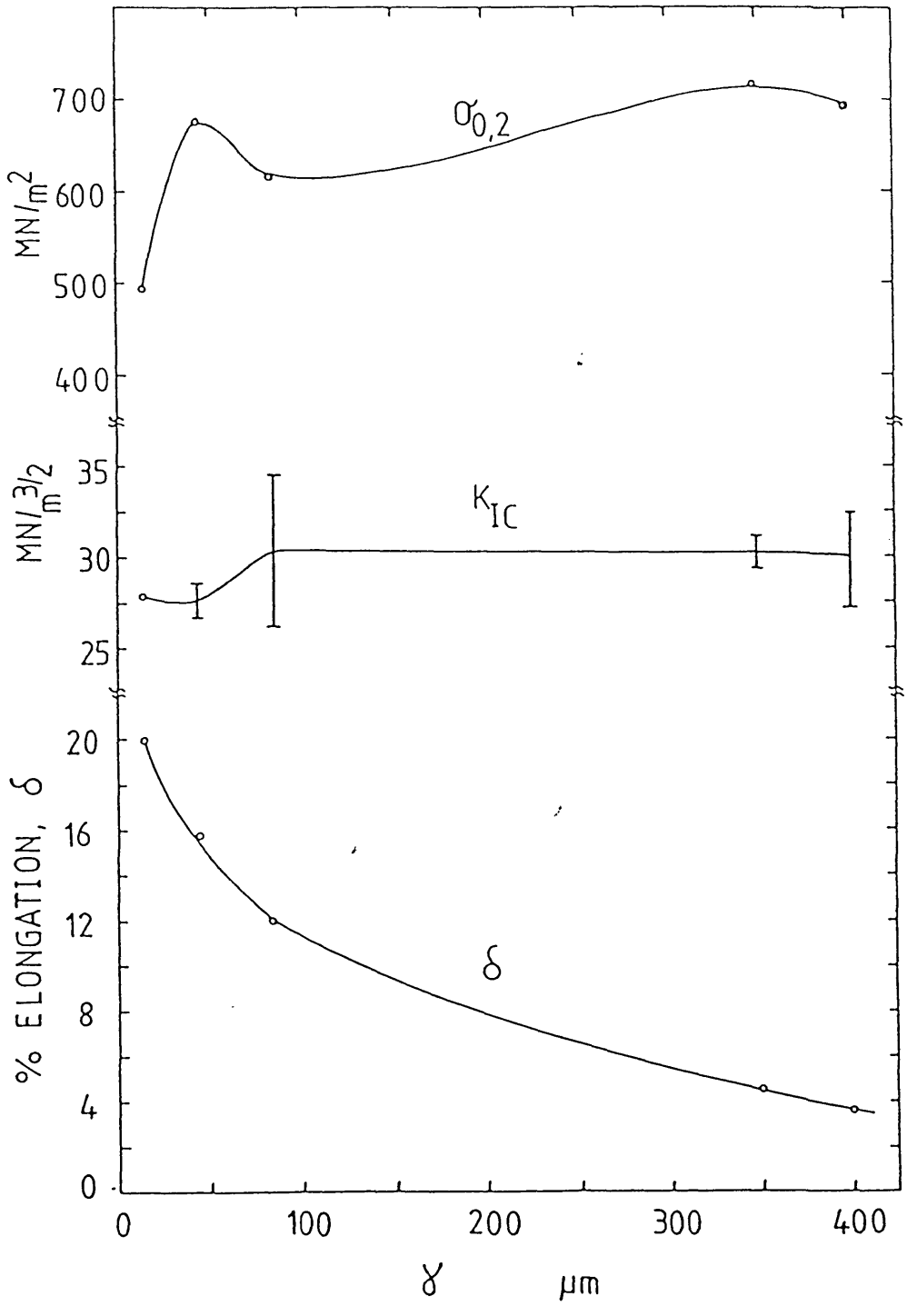
specimens. As noted previously, the series B specimens have finer interlamellar spacings, and therefore higher strength values than the series A specimens.

It is interesting to note in figures 5.5a and 5.6 that the proof stress, ultimate tensile stress and the cleavage fracture stress show very similar trends. Initially strength increases with increasing $\gamma$ grain size until maximum values are attained at a grain size of about 45 $\mu$m, which corresponds to an austenitizing temperature of 900 °C. The data shown in figure 5.5a show a very rapid increase in strength as the grain size increases from 15 to 45 $\mu$m. The more detailed investigation of this regime shown in figure 5.6 confirms that there is an increase in strength, but it is more gradual than indicated by figure 5.5a. This suggests that the strength value of specimen A1 whose microstructure was a mixture of lamellar and spherodised pearlite is anomalously low. For grain sizes in excess of 45 $\mu$m, corresponding to austenitizing temperatures above 900 °C, the strength parameters first decrease, then increase, and finally decrease again, as the grain size is increased.

A separate series of specimens was tested in the normalised condition at room temperature. The data obtained from these specimens are plotted in figure 5.5b where the effect of $\gamma$ grain size on $\sigma_{0.2}$, $\sigma_u$ and tensile ductility $\delta$ is shown. These data were intended to check whether the trend shown in figure 5.5a would be reproduced under different test conditions and different test temperatures. As seen, both sets of data display the same pattern in the variation of strength with austenitising conditions.

Figure 5.7 shows the effect of prior austenite grain size on tensile ductility and $K_{IC}$. The proof stress data from figure 5.5a are included for comparison purposes. The $K_{IC}$ values increased only by about 10 % as the grain size increased from 45 $\mu$m to 80 $\mu$m. Thereafter, $K_{IC}$ remained fairly constant up to the coarsest grain size of 400 $\mu$m. By comparison, the tensile ductility decreased continuously, as the $\gamma$ grain size increased.

Figure 5.7 The effect of prior austenite grain size $\gamma$ on the tensile ductility $\delta$, and the plane strain fracture toughness $K_{IC}$.



## 5.4 The effect of pearlite interlamellar spacing on mechanical properties

The effect of true interlamellar spacing $S_t$ on tensile and cleavage fracture strengths is shown in figure 5.8. These data were obtained from the series S specimens in table 5.2. Again a very similar trend is shown between the tensile and cleavage strength parameters which increase progressively as the interlamellar spacing decreases.

Figure 5.9 shows the effect of interlamellar spacing on tensile ductility and $K_{IC}$. The proof stress data is also included. It can be seen that $K_{IC}$ decreases initially with decreasing interlamellar spacing, but increases again for the finest pearlite. The tensile elongation data, on the other hand, tend to show a pattern opposite to that shown by $K_{IC}$. As the interlamellar spacing decreases, values of $\delta$ increase to a peak value and then start to decrease.

## 5.5 The effect of test temperature on $\sigma_{0.2}$ and $\sigma_f$

The effect of test temperature on proof stress and cleavage fracture stress was investigated by a series specimens designated C and F. The series C specimens were normalized from 900 °C to produce a fairly coarse pearlite having a spacing of about 0.25 $\mu$m. The series F specimens were austenitized at 900 °C, and then isothermally transformed at 550 °C in a salt bath to produce a fine pearlite spacing of about 0.12 $\mu$m.

Table 5.3 shows the strength values determined over the temperature range −25 to −196 °C. The temperature dependence of $\sigma_{0.2}$ and $\sigma_f$ for the coarse pearlitic condition is plotted in figure 5.10. As expected, $\sigma_{0.2}$ increased with decreasing test temperature in accordance with the temperature dependence of the ferrite friction stress. The notable feature of the results is that $\sigma_f$ also increased with decreasing test temperature. This behaviour is not observed for most steels where the cleavage fracture stress has been found to be temperature independent. However, a similar variation of $\sigma_f$ with test temperature has been reported by Lewandowski and Thompson (1984) for a pearlitic steel having a coarse interlamellar spacing.

**Figure 5.8** The effect of pearlite interlamellar spacing $S_t$ on the proof stress $\sigma_{0.2}$, ultimate tensile stress $\sigma_u$, and the cleavage fracture stress $\sigma_f$.

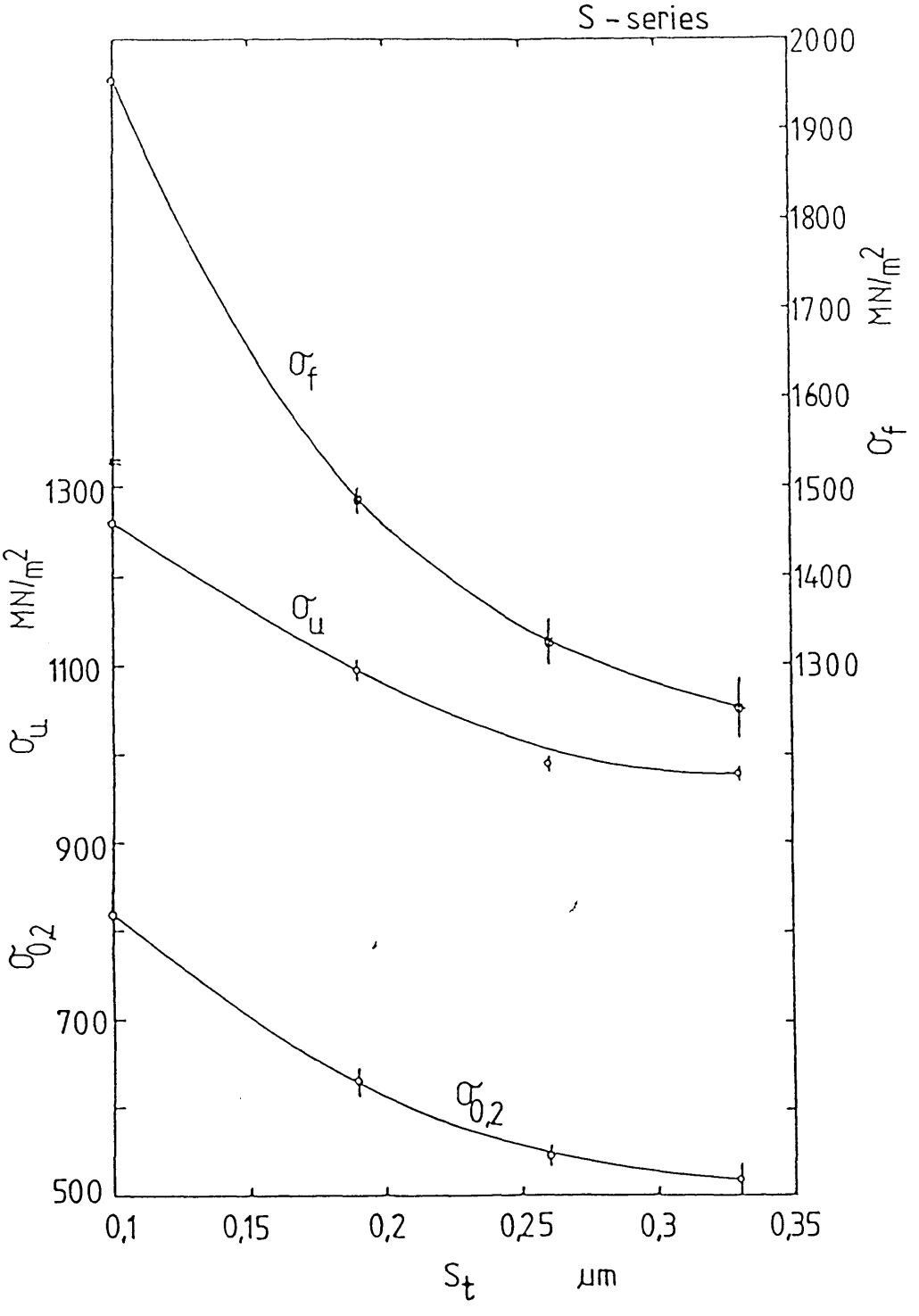


**Figure 5.9** The effect of pearlite interlamellar spacing $S_t$ on the tensile ductility $\delta$, and the plane strain fracture toughness $K_{IC}$.

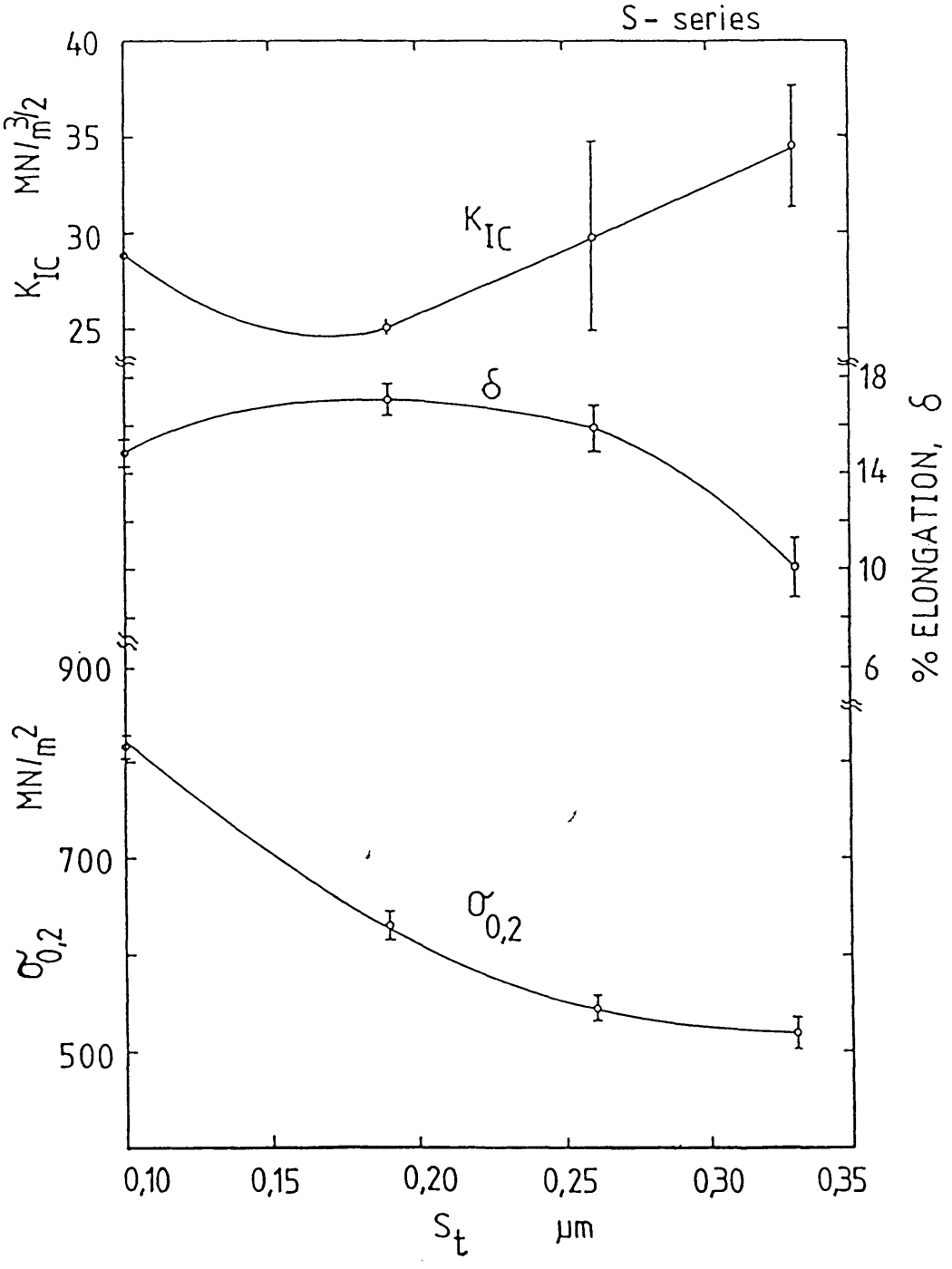
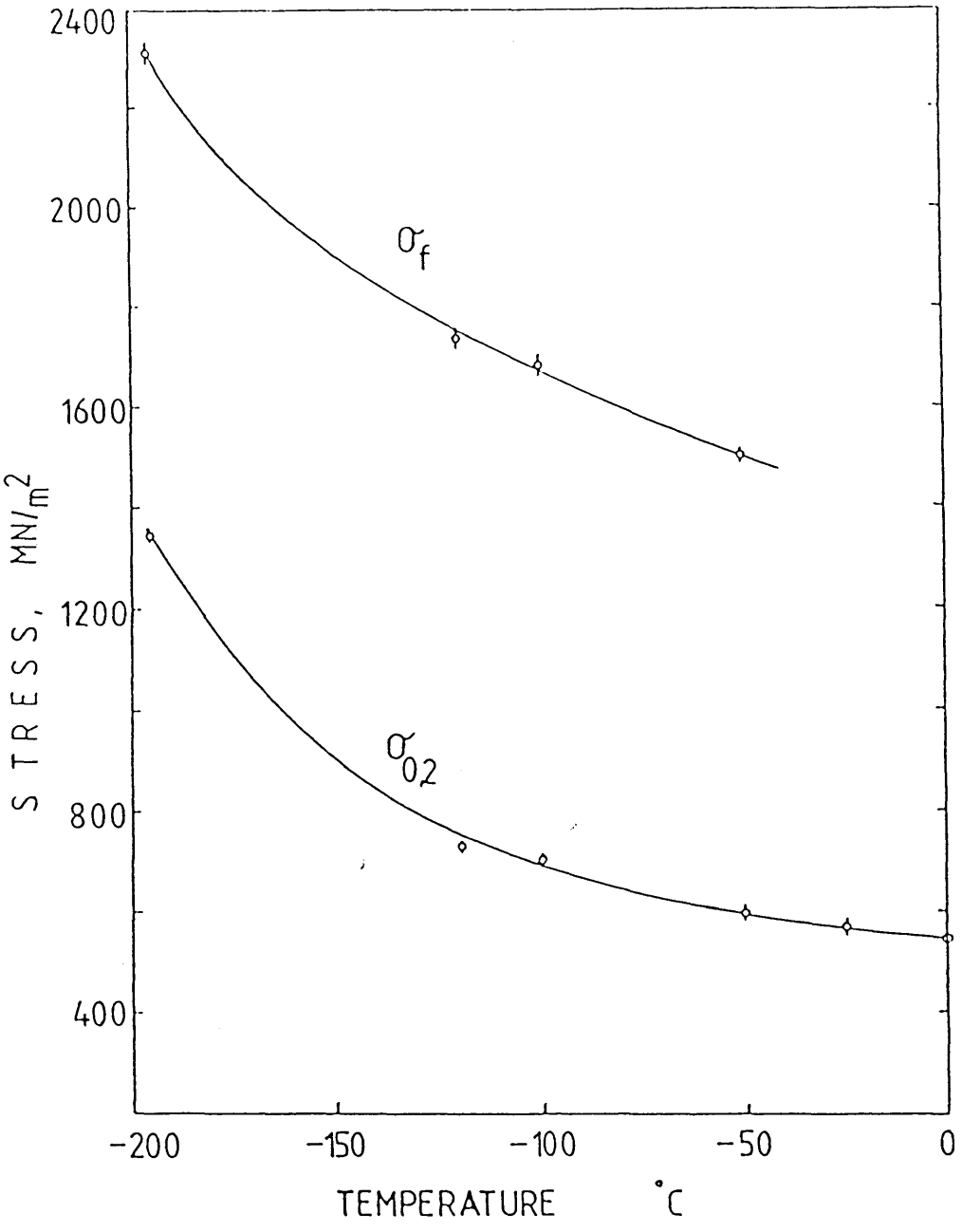


**Figure 5.10** The influence of test temperature on the proof stress $\sigma_{0.2}$ and the cleavage fracture stress $\sigma_f$ in coarse pearlite



The temperature dependence of $\sigma_{0.2}$ and $\sigma_f$ in the fine pearlitic condition is plotted in figure 5.11. The temperature dependence of $\sigma_{0.2}$ is similar to that observed in coarse pearlite. The significant difference in these data is that the cleavage fracture stress is temperature independent.

In figure 5.12, $\sigma_f$ is plotted against $\sigma_{0.2}$ for both the coarse and fine pearlitic conditions. Two distinct regimes can be identified in this plot. For cleavage fracture stresses less than about 2100 $MN/m^2$, $\sigma_f$ is directly proportional to $\sigma_{0.2}$. For values greater than or equal to 2100 $MN/m^2$, $\sigma_f$ appears to be almost independent of $\sigma_{0.2}$.

**Table 5.3** The variation of $\sigma_f$ and $\sigma_{0.2}$ with test temperature for coarse (C) and fine (F) pearlite.

| Specimen | Test temperature °C | $\sigma_{0.2}$ ($MN/m^2$) (compression) | $\sigma_f$ ($MN/m^2$) |
|---|---|---|---|
| C1 | -25 | 572 | * |
| C2 | -25 | 572 | * |
| C3 | -50 | 600 | 1500 |
| C4 | -50 | 600 | 1515 |
| C5 | -100 | 708 | 1710 |
| C6 | -100 | 708 | 1667 |
| C7 | -120 | 731 | 1762 |
| C8 | -120 | 731 | 1718 |
| C9 | -196 | 1344 | 2332 |
| C10 | -196 | 1344 | 2298 |
| F1 | -25 | 850 | 2057 |
| F2 | -25 | 856 | 2217 |
| F3 | -50 | 888 | 2167 |
| F4 | -50 | 921 | 2012 |
| F5 | -100 | 1003 | 2006 |
| F6 | -100 | 965 | 1998 |
| F7 | -150 | 1172 | 2121 |
| F8 | -150 | 1183 | 2023 |
| F9 | -196 | 1548 | 1942 |
| F10 | -196 | 1550 | 2279 |

* Beyond the validity of the Griffiths and Owen (1971) analysis.

Figure 5.11 The influence of test temperature on the proof stress $\sigma_{0.2}$ and the cleavage fracture stress $\sigma_f$ in fine pearlite.

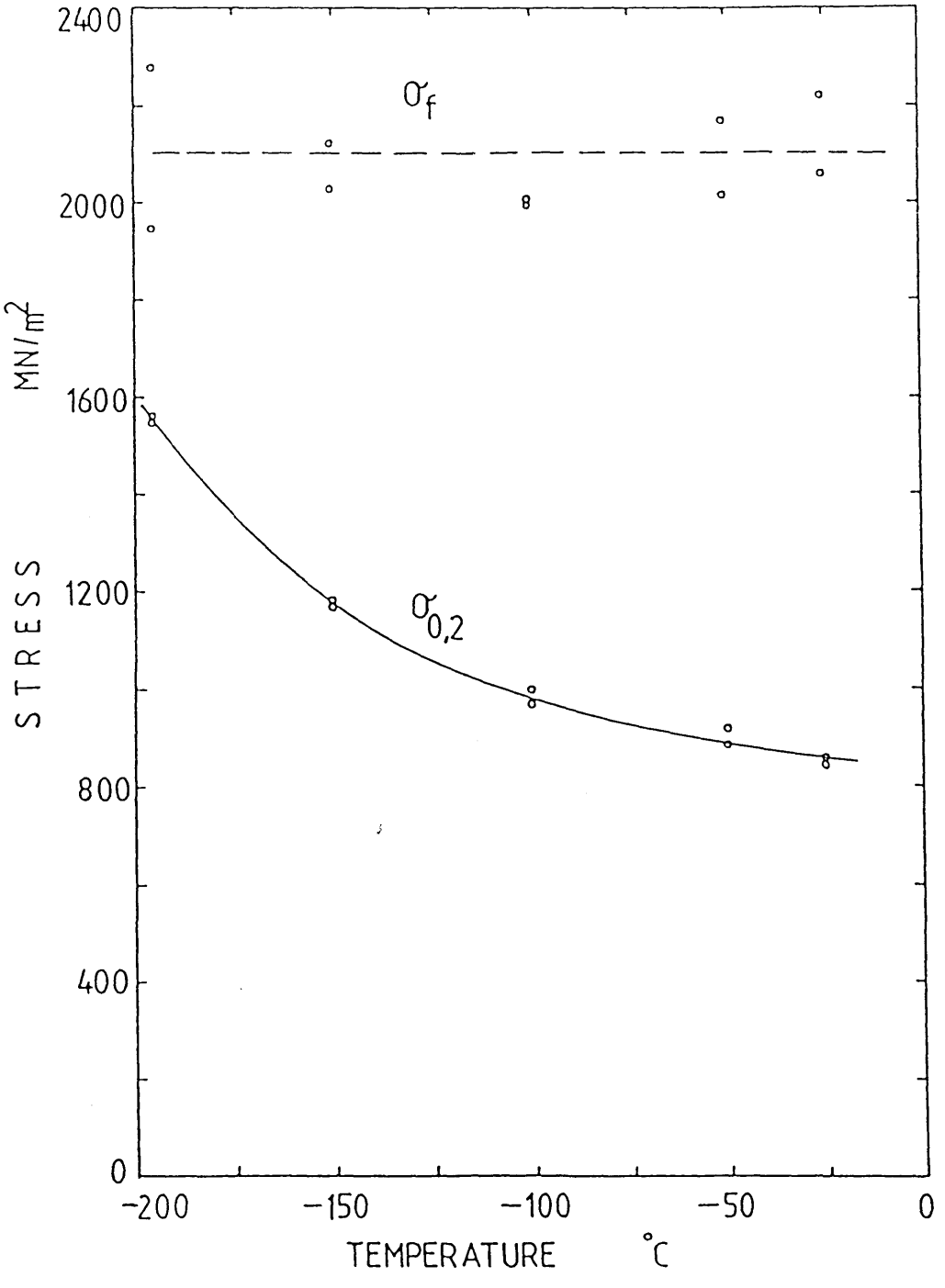
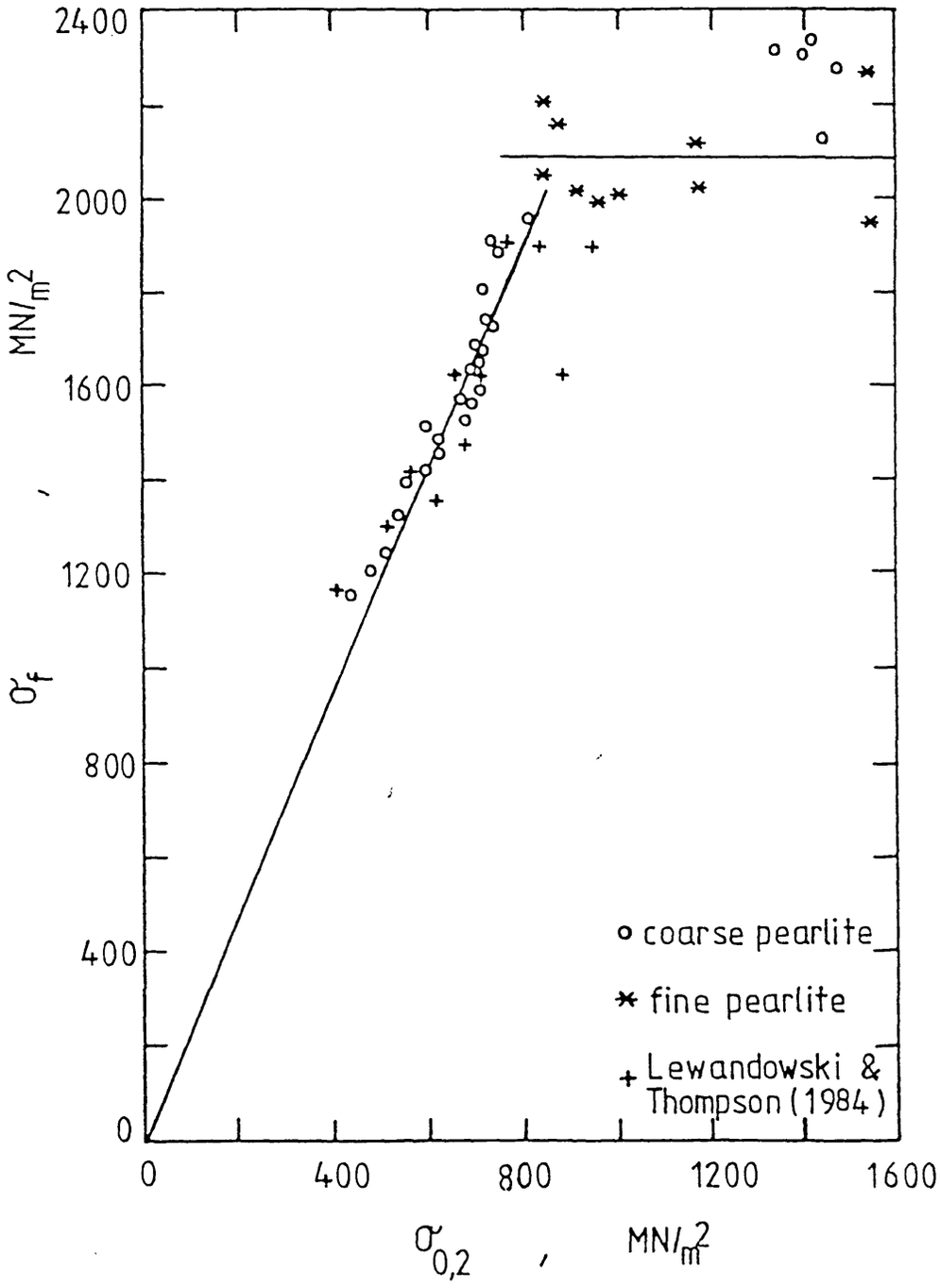


Figure 5.12 The relationship between the proof stress $\sigma_{0.2}$, and the cleavage fracture stress $\sigma_f$, for a range of microstructures and testing conditions. Data determined by Lewandowski and Thompson (1984) is included for comparison purposes.



## 5.6 Fractography

All the fracture specimens which were examined failed by transgranular cleavage. A typical example is shown in figure 5.13. Occasionally, localized regions of fibrous fracture were observed where cleavage facets had been linked by shear, (figure 5.14). The fracture appearance in coarse and fine pearlite was essentially similar. Measurements of the cleavage facet size showed that this was similar to the pearlite nodule size. The relationship between facet size and nodule size was further studied on fracture surfaces which were etched in nital. As seen in figure 5.15, the cleavage facets consist of more than one pearlite colony. Such colonies belong to the same pearlite nodule. Figures 5.16(a) and 5.16(b) show part of the fracture path as seen in a nickel plated specimen. The cleavage crack changed direction at the nodule boundaries, confirming that the facets were related to pearlite nodules.

The early stages of crack nucleation were studied using double notched bend specimens. When these specimens are loaded in pure bending, the two notches are exposed to nominally identical stress and strain. Usually only one of the notches fails. The unbroken notch should then represent the condition of the material which has been unloaded from a stress almost equal to its cleavage fracture stress. If the region beneath the unbroken notch is sectioned and subjected to appropriate microstructural examination, it may be possible to detect non-propagating microcracks.

Double notched specimens containing both fine and coarse pearlite conditions were examined. Only in the case of coarse pearlite was it possible to identify microcracks beneath the notch root. The cracks were generally seen to lie at 45° to the direction of maximum tensile stress. In addition, the cracks tended to be of pearlite colony size, as seen in figure 5.17. Figure 5.18 shows the appearance of this crack at higher magnification. It is apparent that the microcrack is not continous, but consists of a series of carbide-initiated voids connected by ligaments of plastically deformed ferrite. This was the feature of all the microcracks observed.

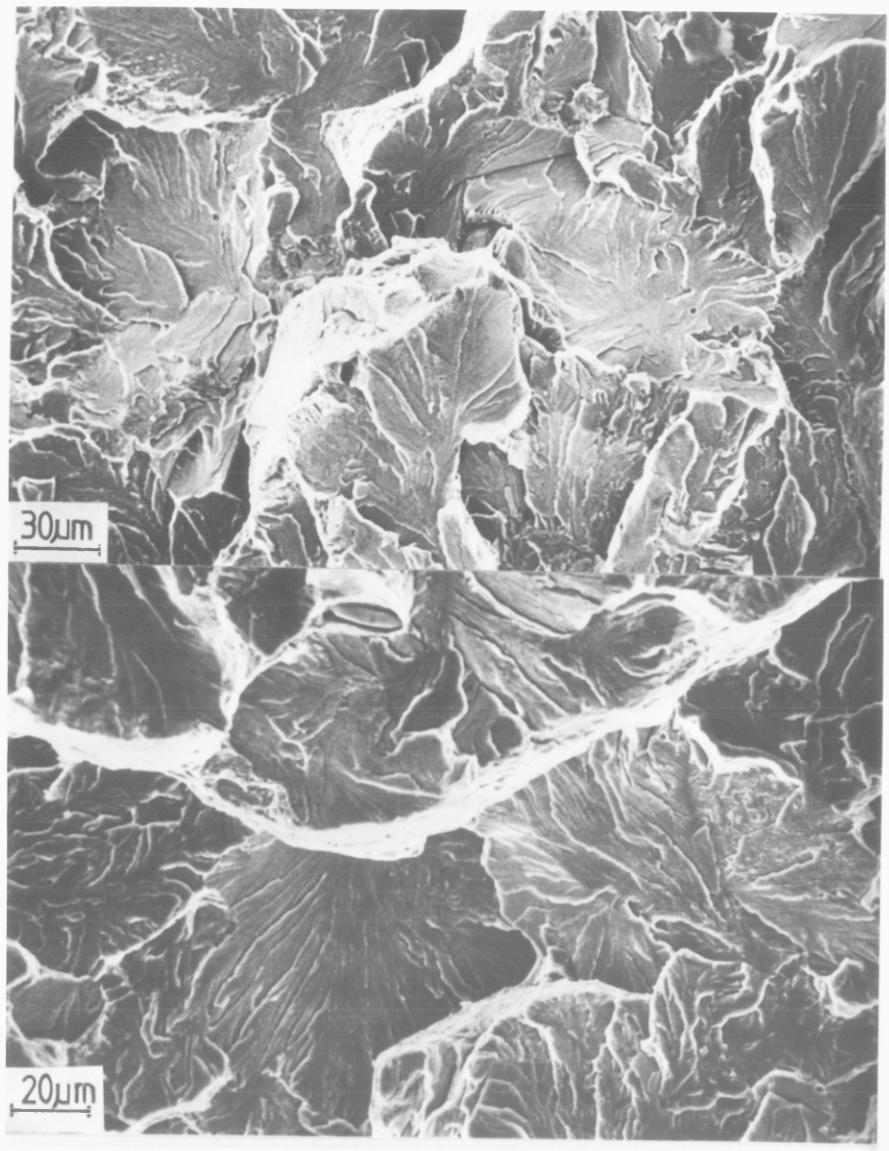



FIGURE 5.13

Transgranular cleavage fracture in the bend specimens.

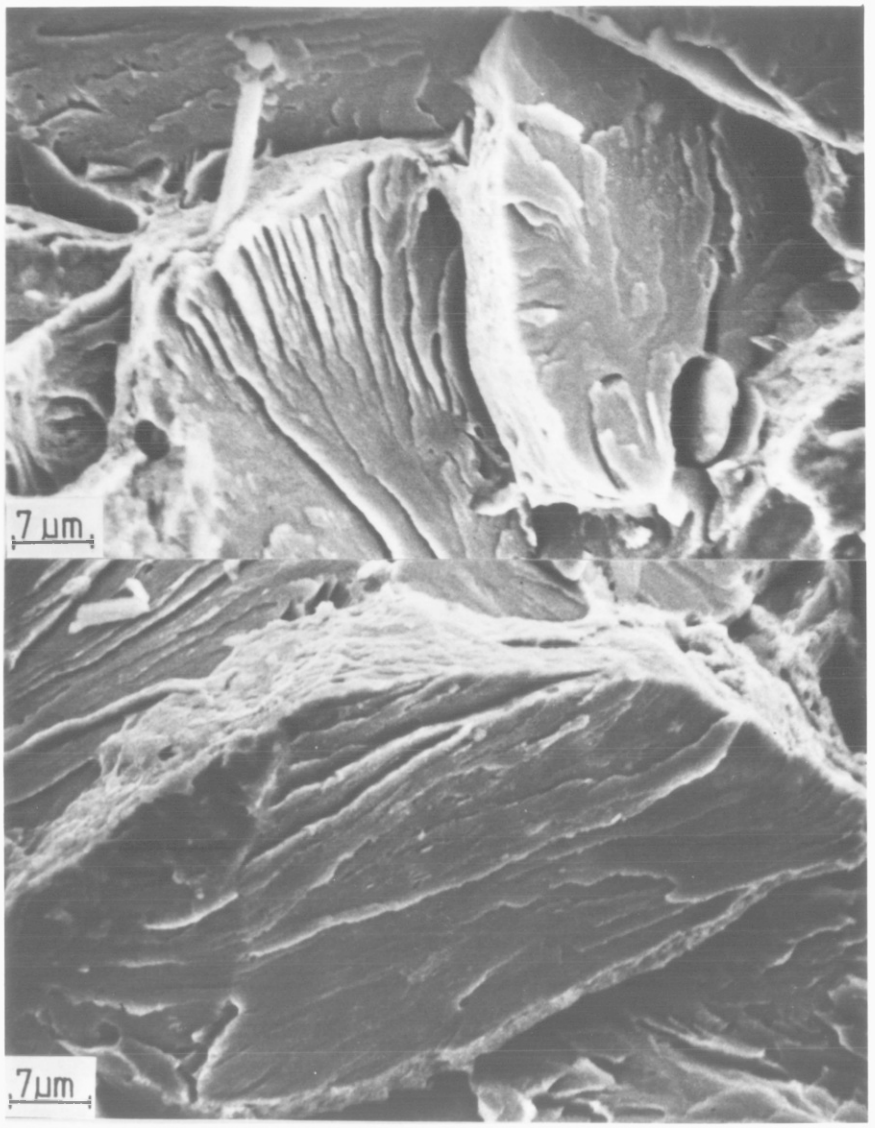



FIGURE 5.14

Localised regions of fibrous fracture where cleavage facets were linked by shear.

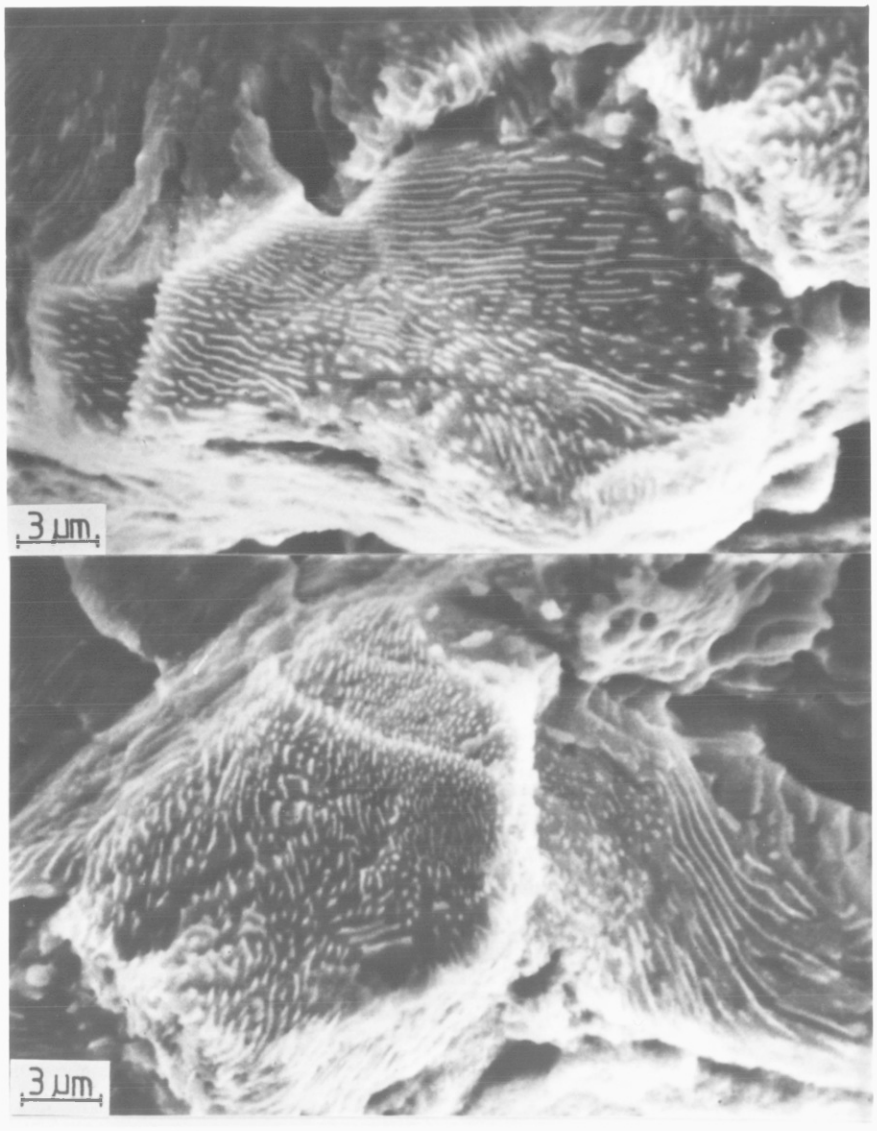



FIGURE 5.15

The pearlitic microstructure is revealed on cleavage facets after etching the fracture surface in nital.

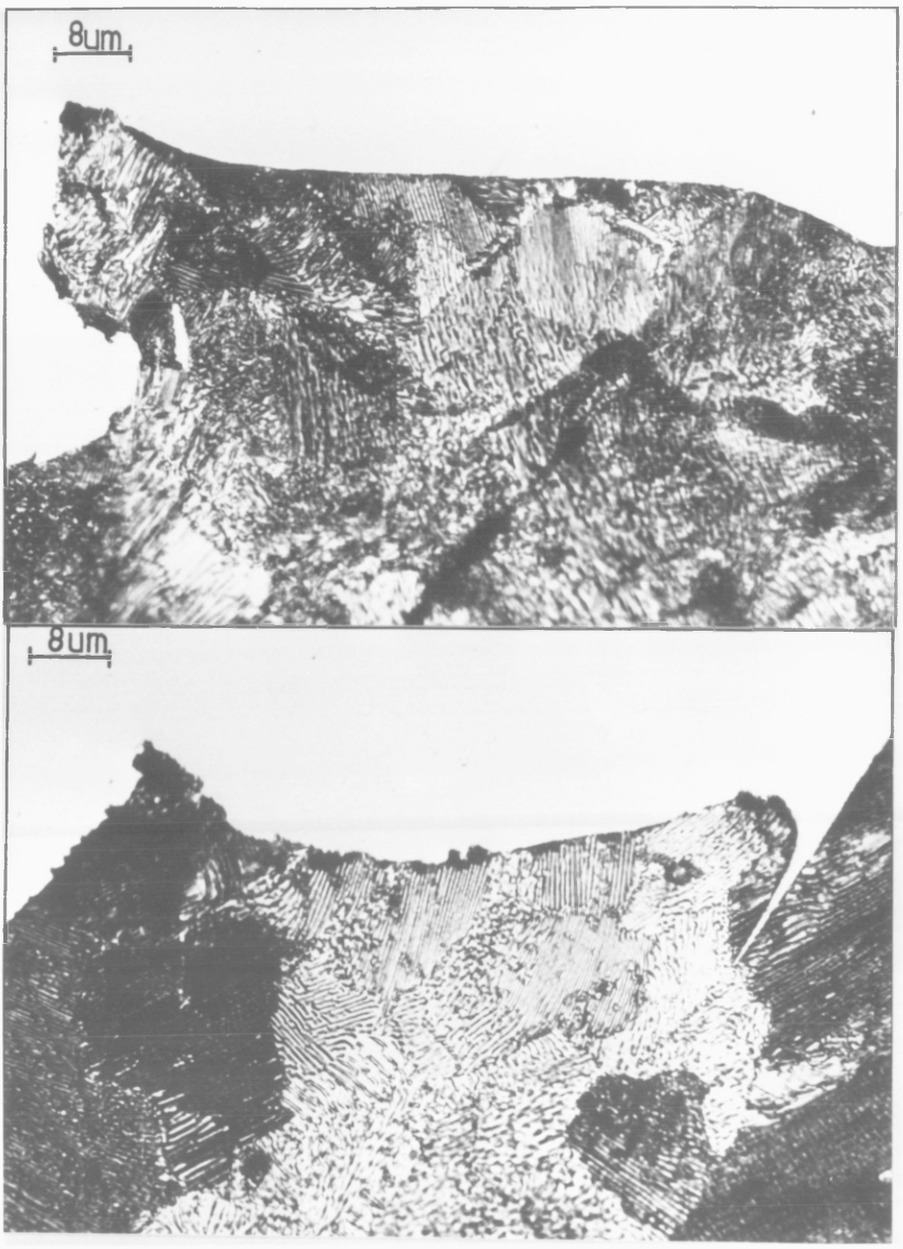



FIGURE 5.16(a)

The fracture path as seen in nickel plated fracture surface of the eutectoid steel.

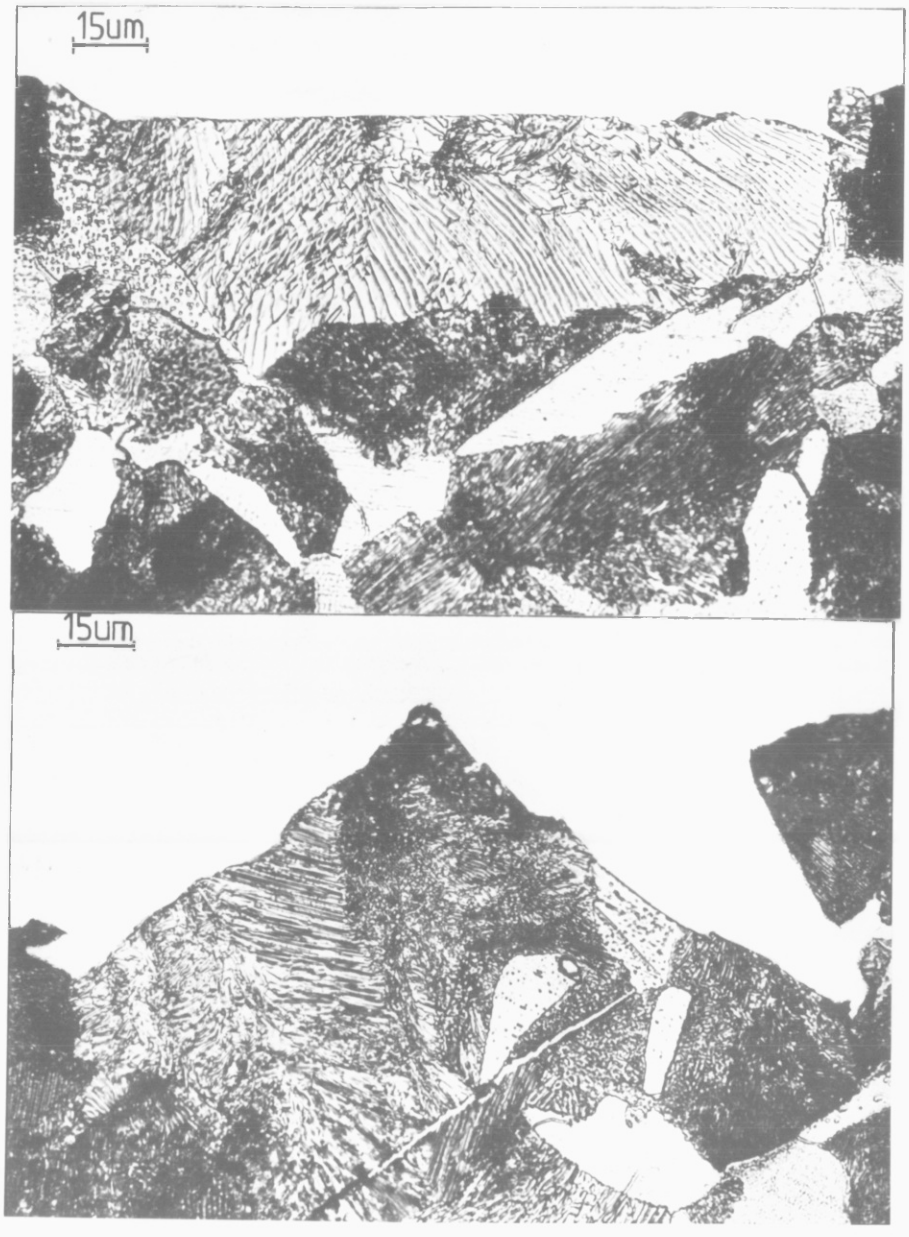



FIGURE 5.16(b)

The fracture path as seen in nickel plated fracture surface of the hypoeutectoid steel.

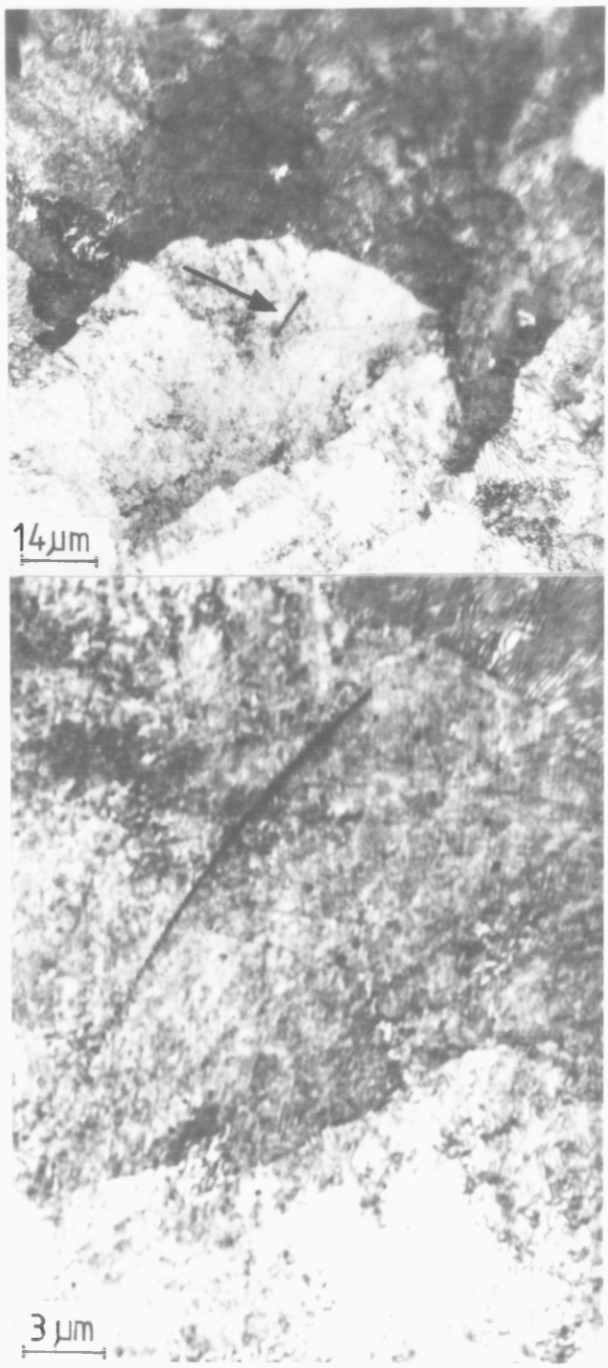



FIGURE 5.17

A colony-sized non-propagating microcrack seen in the double notched bend specimens.

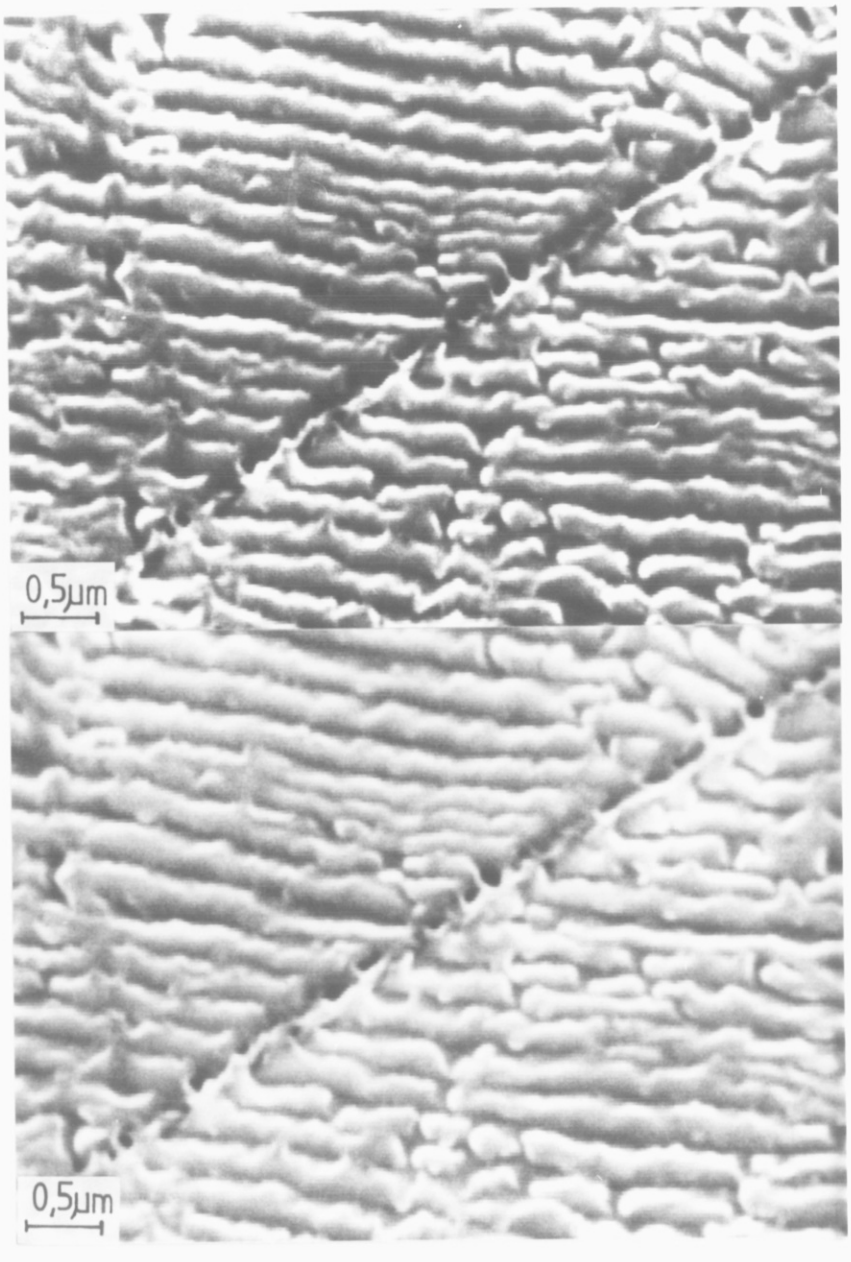



FIGURE 5.18

At high magnifications the non propagating micro-cracks are seen to consist of a series of voids connected by ligaments of plastically deformed ferrite.

# 6. RESULTS FROM THE HYPOEUTECTOID STEEL

## 6.1 The Microstructure.

Figure 6.1 shows the microstructure of the hypoeutectoid steel in the as-received condition. The volume fraction of pearlite is about 92 %. Figures 6.2 and 6.3 show the microstructures of specimens which were austenitised at 800 and 1200 °C respectively before being transformed in a salt bath at 510 °C. The difference in prior austenite grain size is clearly revealed by the proeutectoid ferrite. Figure 6.4 shows the microstructure of specimens which were austenitized at 900 °C and transformed at 510 and 650 °C. The difference in the interlamellar spacing is quite evident. The coarsest spacing was obtained in the furnace cooled specimen whose microstructure is shown in figure 6.5.

Table 6.1 shows the effect of the heat treatments on the microstructural parameters. Specimens H1 to H7 represent the conditions where the prior austenite grain size was the dominant microstructural parameter which varied during the heat treatments. As observed in the eutectoid steel, an increase in prior austenite grain size is accompanied by a corresponding increase in pearlite nodule size. The change in austenite grain size has a small effect on pearlite colony size and pearlite interlamellar spacing. However in the fine grain regime (H1 & H2), an increase in ferrite mean free distance $\lambda_\alpha$ is observed. In specimens H8 to H11, the dominant microstructural variable was the interlamellar spacing which decreased with decreasing transformation temperature. Decreasing the transformation temperature also has the effect of decreasing the pearlite colony size, and to a lesser extent the nodule size. It is of note that there is a significant increase in the ferrite mean free distance $\lambda_\alpha$ as the interlamellar spacing increases. This is due to the increase in the volume fraction of proeutectoid ferrite $V_\alpha$ which raises $\lambda_\alpha$ according to equation 4.6. Thus in specimen H11 which had a ferrite volume fraction of 15% (table 6.1) $\lambda_\alpha$ is 2.1 $\mu$m whilst the corresponding value for a fully pearlitic microstructure ($\lambda$) is only 0.59 $\mu$m.

It is interesting to note that in specimens H1 to H7 the volume fraction of proeutectoid ferrite $V_\alpha$ decreases from about 8 % for an austenite grain size of about 22 $\mu$m to almost 1 % for grain sizes of obout 90 $\mu$m and

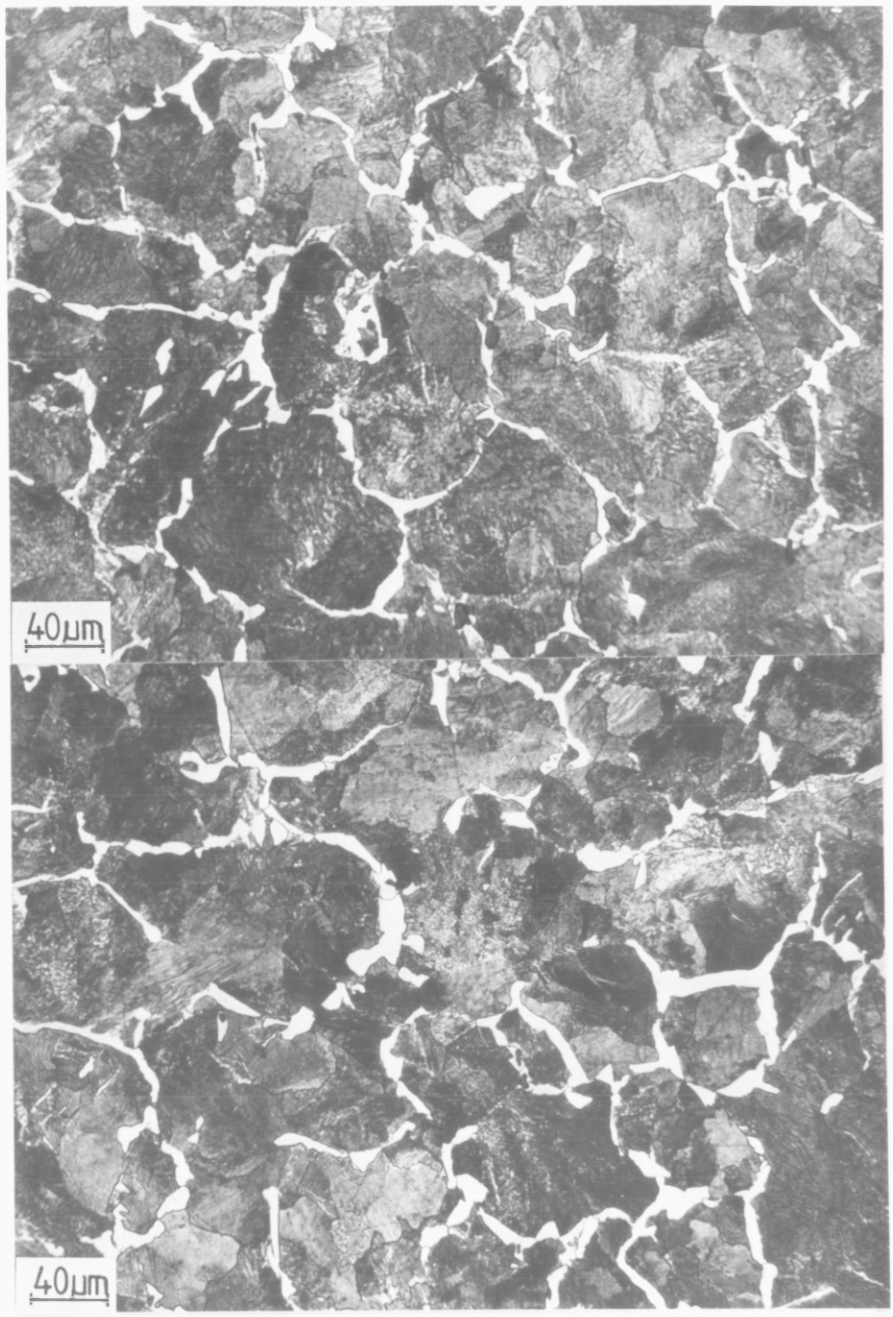



FIGURE 6.1

The microstructure of the hypoeutectoid steel in the as received condition.

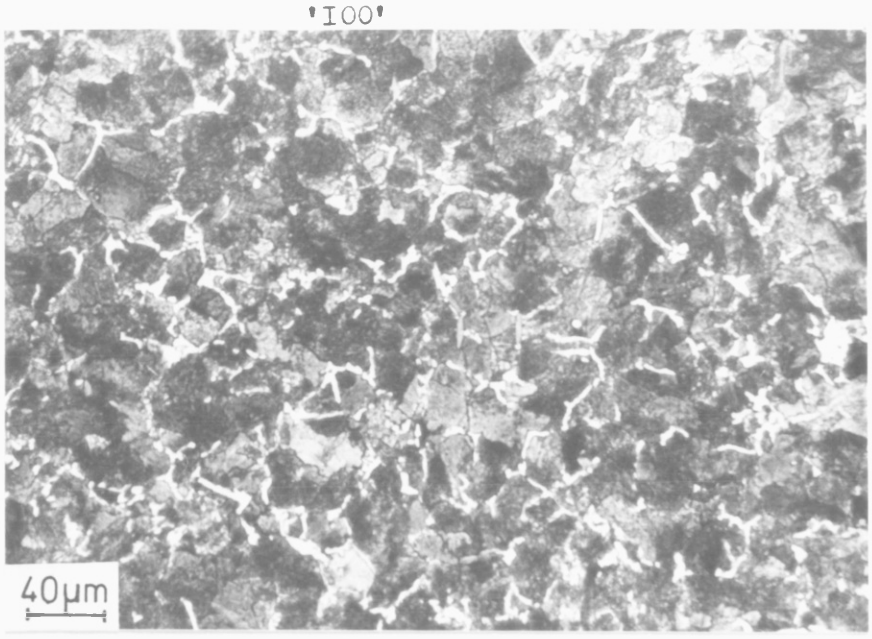



FIGURE 6.2

The microstructure of the specimen which was austenitised for $\frac{1}{4}$ hr at 800 °C and transformed in a salt bath at 510 °C.

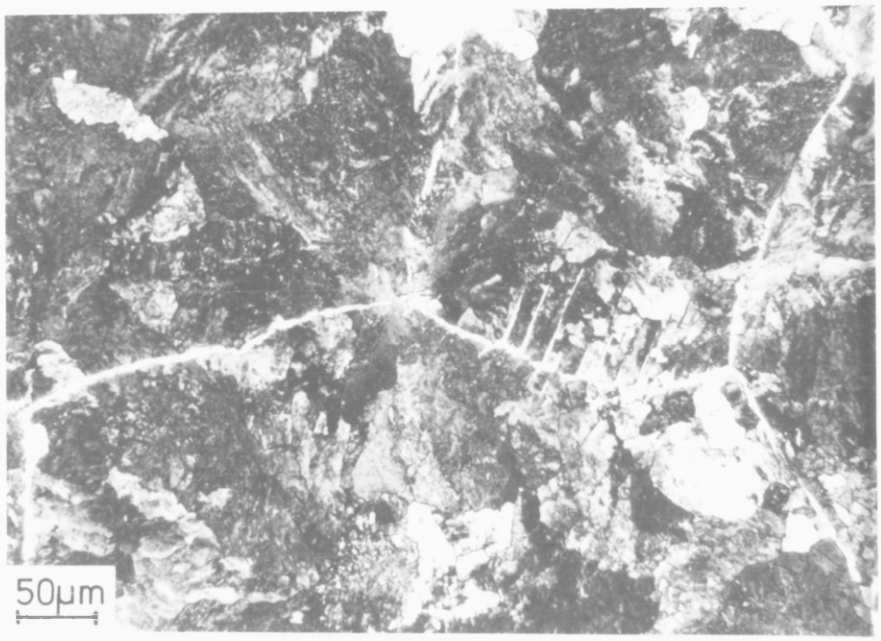



FIGURE 6.3

The microstructure of the specimen which was austenitised for 1 hr at 1200 °C and transformed in a salt bath at 510 °C.

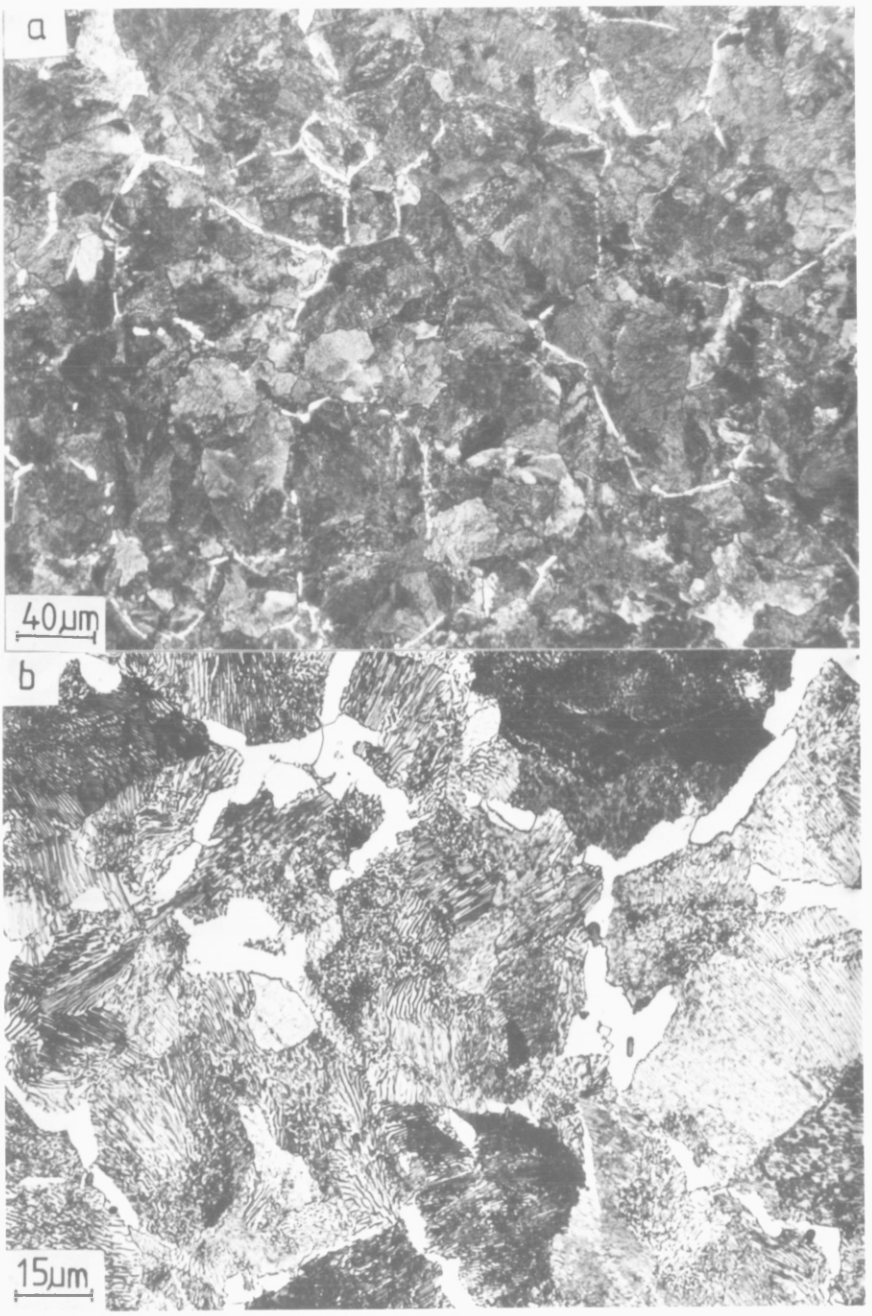



FIGURE 6.4

The microstructure of the specimens which were austenitised at 900 °C and transformed at (a) 510 °C and (b) 650 °C.

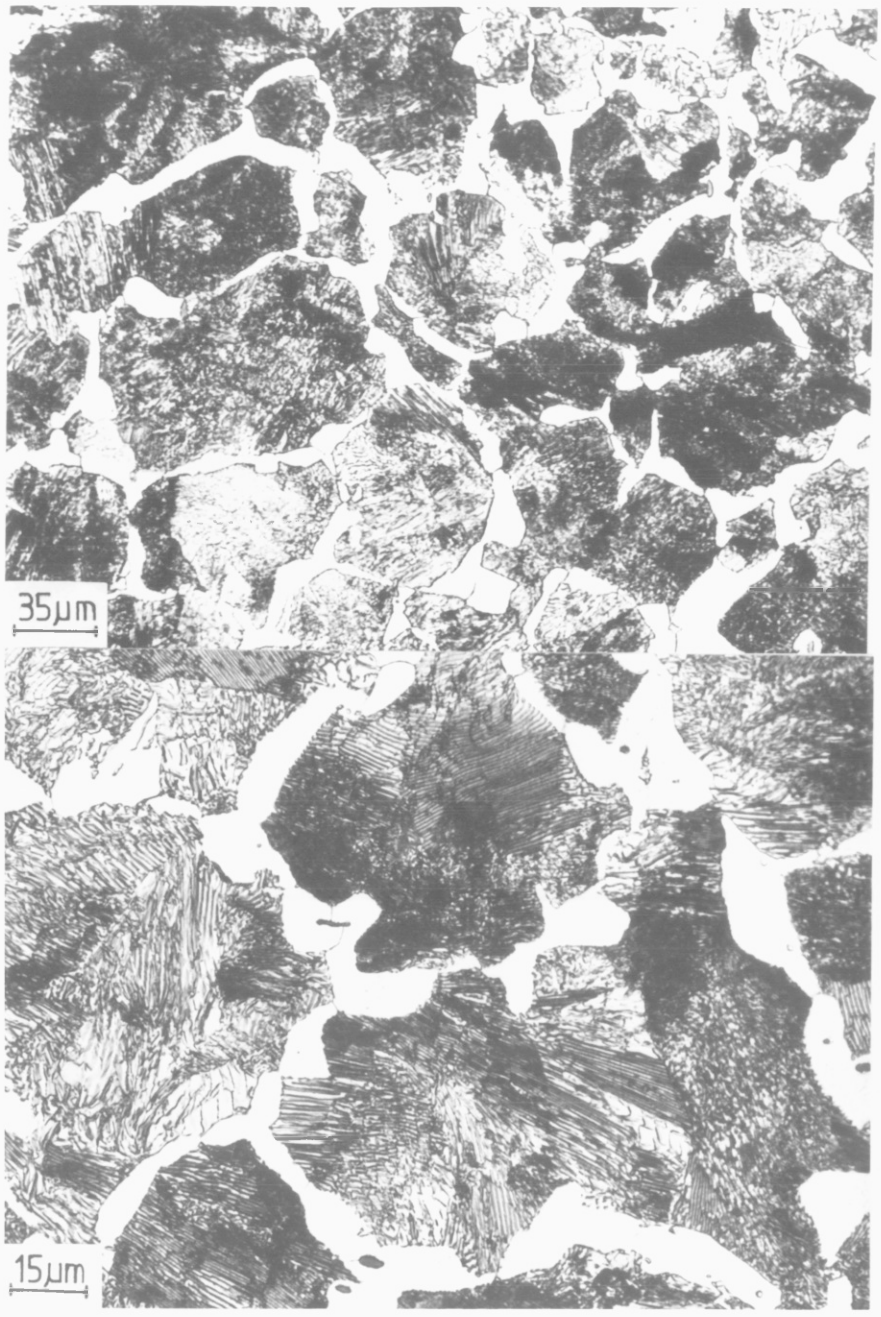



FIGURE 6.5

The microstructure of the specimen which was austenitised at 900 °C and furnace cooled at 1.6 °C/minute.

**Table 6.1** Microstructural parameters measured from the hypoeutectoid steel.

| Specimen | $\gamma$ μm | $S_t$ μm | C μm | N μm | $\lambda_\alpha$ μm | t μm | $V_\alpha$ % | $\lambda$ μm |
|---|---|---|---|---|---|---|---|---|
| H1 | 21.8 | 0.12 | 9.5 | 14 | 0.344 | 0.010 | 8.1 | 0.23 |
| H2 | 36.4 | 0.11 | 8.6 | 20 | 0.274 | 0.010 | 4.9 | 0.21 |
| H3 | 76.6 | 0.10 | 7.7 | 28 | 0.197 | 0.009 | 1.6 | 0.19 |
| H4 | 90.0 | 0.11 | 7.8 | 40 | 0.209 | 0.010 | 1.1 | 0.21 |
| H5 | 166.7 | 0.12 | 8.2 | 56 | 0.234 | 0.010 | 1.0 | 0.23 |
| H6 | 195.7 | 0.13 | 8.0 | 80 | 0.270 | 0.011 | 1.3 | 0.25 |
| H7 | 271.0 | 0.12 | 9.1 | 113 | 0.250 | 0.010 | 1.1 | 0.23 |
| H8 | 90.0 | 0.11 | 7.8 | 40 | 0.209 | 0.010 | 1.1 | 0.21 |
| H9 | 88.2 | 0.19 | 8.9 | 56 | 0.389 | 0.016 | 2.3 | 0.36 |
| H10 | 87.6 | 0.26 | 11.2 | 68 | 0.674 | 0.023 | 7.2 | 0.50 |
| H11 | 82.9 | 0.31 | 13.0 | 80 | 2.100 | 0.026 | 15.1 | 0.59 |
| HR | 62.6 | 0.19 | 10.2 | 28 | 0.440 | 0.016 | 7.8 | 0.36 |

$\gamma$ -prior austenite grain size; $S_t$ -mean true interlamellar spacing; C -pearlite colony size; N -nodule size; $\lambda\alpha$ -ferrite mean free distance in the mixed ferrite/pearlite microstructure; t -thickness of cementite lamellae; Vα -volume fraction of proeutectoid ferrite; $\lambda$ -mean free distance in pearlitic ferrite.

above. This behavior is not unexpected because as the austenite grain size increases, the nose of the TTT curve is shifted to the right, thus reducing the opportunity for ferrite formation. In specimens H8 to H11, $V_\alpha$ increases with increasing interlamellar spacing. This is attributed to the fact that as the transformation temperature increases, the opportunity of forming ferrite also increases.

**6.2 Mechanical properties**

Table 6.2 shows the mechanical properties determined for each heat treatment condition. These data were determined at a temperature of −100 °C because at the temperature of −80 °C where the eutectoid steel was tested, the hypoeutectoid steel would undergo general yield prior to fracture. The values quoted in the table are a mean from duplicate tests.

A large number of the tensile specimens displayed a well defined yield point. But since the yield stress in those specimens corresponded to the 0.2 % proof stress, it was decided to characterize yielding by the proof stress $\sigma_{0.2}$. The $\sigma_f$ tests satisfied the conditions of the Griffiths and Owen (1971) analysis, and the $K_{IC}$ results were valid.

**6.3 The effect of austenitising conditions on mechanical properties.**

As pointed out earlier, the effect of austenitising conditions on mechanical properties was related to changes in prior austenite grain size. Table 6.2 and figure 6.6 show the effect of prior austenite grain size on proof stress $\sigma_{0.2}$, ultimate tensile stress $\sigma_u$, and cleavage fracture stress $\sigma_f$. The data plotted refer to specimens H1 to H7. The proof stress and ultimate tensile stress show almost identical trends. Although there is a slight increase in proof and ultimate tensile strength as the austenite grain size increases from 22 to 75 $\mu$m, followed by a decrease for grain sizes beyond 75 $\mu$m, the overall effect of austenite grain size on proof and ultimate tensile strength is small. The change in strength over the entire grain size range of 22 to 270 $\mu$m was only about 14 % for the proof stress and 10 % for the ultimate tensile stress. The cleavage fracture stress appears to be influenced more strongly by changes in austenitising conditions. A peak in the $\sigma_f$ curve occurs at a

**Table 6.2** Mechanical properties of the hypoeutectoid steel determined at -100 °C.

| Specimen | Parameter varied | $\sigma_{0.2}$ $MN/m^2$ | $\sigma_u$ $MN/m^2$ | $\sigma_f$ $MN/m^2$ | $\delta$ % | $K_{IC}$ $MN/m^{3/2}$ |
|---|---|---|---|---|---|---|
| H1 | $\gamma$ | 656 | 1035 | 1285 | 21.3 | 28.5 |
| H2 | $\gamma$ | 666 | 1042 | 1312 | 20.7 | 29.4 |
| H3 | $\gamma$ | 689 | 1076 | 1378 | 18.8 | 29.0 |
| H4 | $\gamma$ | 665 | 1035 | 1546 | 17.9 | 27.2 |
| H5 | $\gamma$ | 599 | 988 | 1307 | 11.8 | 25.7 |
| H6 | $\gamma$ | 593 | 993 | 1150 | 12.6 | 26.4 |
| H7 | $\gamma$ | 613 | 943 | 1159 | 6.4 | 31.2 |
| H8 | $S_t$ | 665 | 1035 | 1546 | 17.9 | 27.2 |
| H9 | $S_t$ | 601 | 988 | 1321 | 19.1 | 24.9 |
| H10 | $S_t$ | 527 | 887 | 1153 | 20.2 | 32.2 |
| H11 | $S_t$ | 485 | 834 | 1058 | 18.7 | 25.2 |
| HR* | as received | 550 | 920 | 1254 | 16.9 | 43.9 |

$\sigma_{0.2}$ -proof stress; $\sigma_u$ -ultimate tensile stress; $\sigma_f$ -cleavage fracture stress; $\delta$ -elongation at fracture (tensile ductility) $K_{IC}$ -plane strain fracture toughness; $\gamma$ -prior austenite grain size; $S_t$ -interlamellar spacing.

* HR was tested at -80 °C.

Figure 6.6 The effect of prior austenite grain size $\gamma$ on proof stress $\sigma_{0.2}$, ultimate tensile stress $\sigma_u$ and cleavage fracture stress $\sigma_f$ in the hypoeutectoid steel.

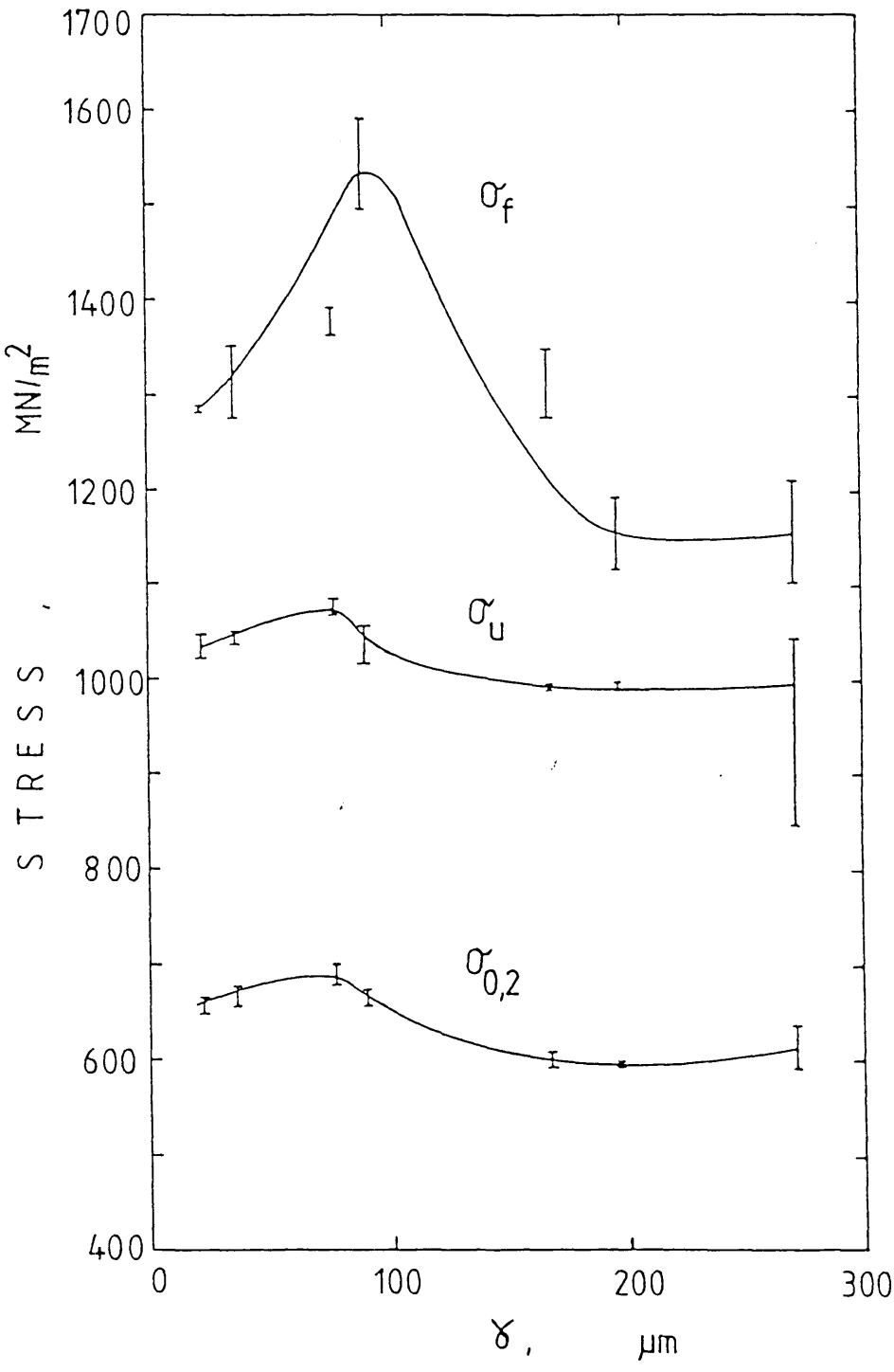
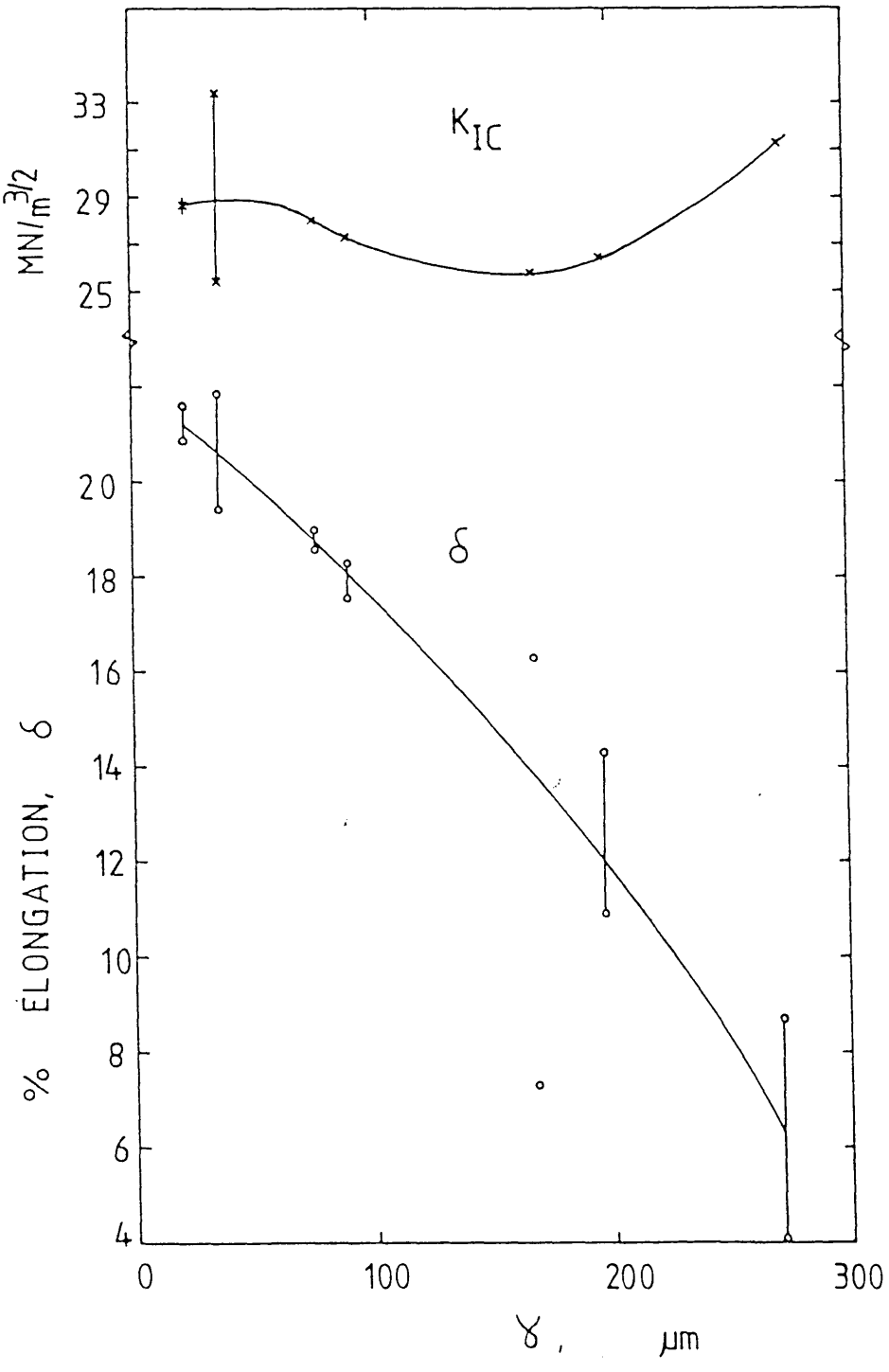


Figure 6.7 The effect of prior austenite grain size $\gamma$ on tensile ductility $\delta$ and plane strain fracture toughness $K_{IC}$ in the hypoeutectoid steel.



grain size of about 90 $\mu m$, corresponding to an austenitizing temperature of 900 °C. The similar trend between cleavage fracture stress and proof stress which was a feature of the eutectoid steel is less strongly depicted in this case.

Figure 6.7 shows the effect of $\gamma$ grain size on tensile ductility and $K_{IC}$. The proof stress data from figure 6.6 are also included. As the austenite grain size increases, the tensile ductility, as measured by the elongation at fracture decreases progressively. By comparison, the variation in the plane strain fracture toughness is small. The overall change in $K_{IC}$ over the entire range of grain sizes is only about 17 %. It is interesting to note that the highest $K_{IC}$ values occur in the coarse grain condition where both tensile and cleavage fracture strengths have their lowest values.

### 6.4 The effect of pearlite interlamellar spacing on mechanical properties

The effect of true interlamellar spacing $S_t$ on the tensile and cleavage fracture strengths is shown in figure 6.8. The data plotted are from specimens H8 to H11 in table 6.2. A similar trend is shown between the proof stress, ultimate tensile stress and cleavage fracture stress which increase progressively as the interlamellar spacing decreases. This behaviour is similar to that observed in the eutectoid steel except for the fine grain regime were the $\sigma_f$ curve appears to deviate slightly from the trend in the $\sigma_{0.2}$ and $\sigma_u$ curves.

Figure 6.9 shows the effect of interlamellar spacing on tensile ductility and $K_{IC}$. For interlamellar spacings ranging from 0.10 to about 0.26 $\mu m$, the tensile ductility progressively increases as the pearlitic spacing increases. This trend reflects the commonly observed inverse relationship between strength and ductility. The specimen with an interlamellar spacing of 0.31 $\mu m$ showed a slight drop in tensile ductility, thus causing the ductility curve to exhibit a peak value at an interlamellar spacing of about 0.26 $\mu m$. The effect of interlamellar spacing on $K_{IC}$ is more complex. As the interlamellar spacing increased, the fracture toughness decreased to a minimum and then started to increase, reaching a peak at a pearlite spacing of about 0.26 $\mu m$. Beyond this spacing, $K_{IC}$ appeared to decrease again. It is interesting to note that

Figure 6.8 The effect of interlamellar spacing $S_t$ on proof stress $\sigma_{0.2}$, ultimate tensile stress $\sigma_u$ and cleavage fracture stress $\sigma_f$ in the hypoeutectoid steel.

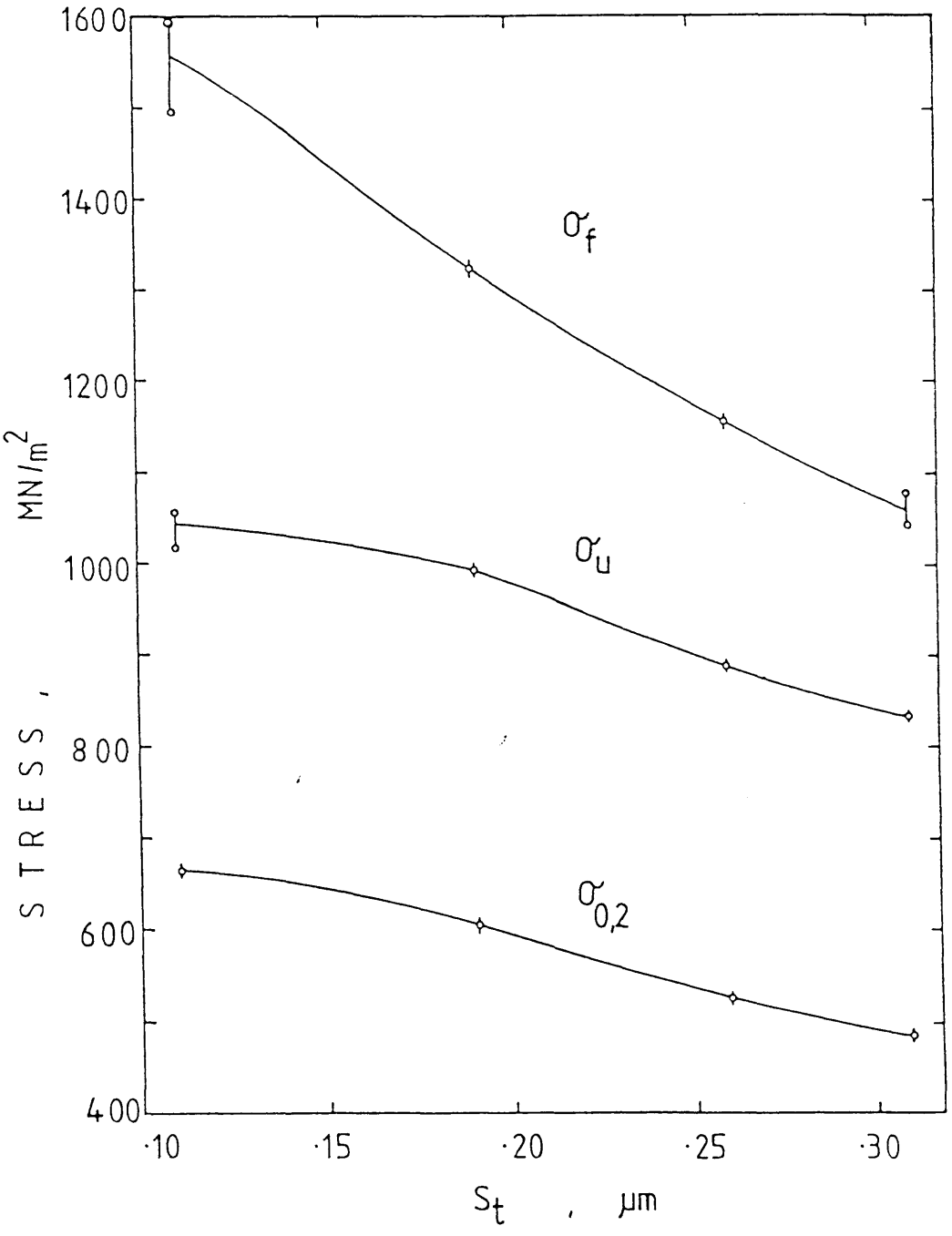
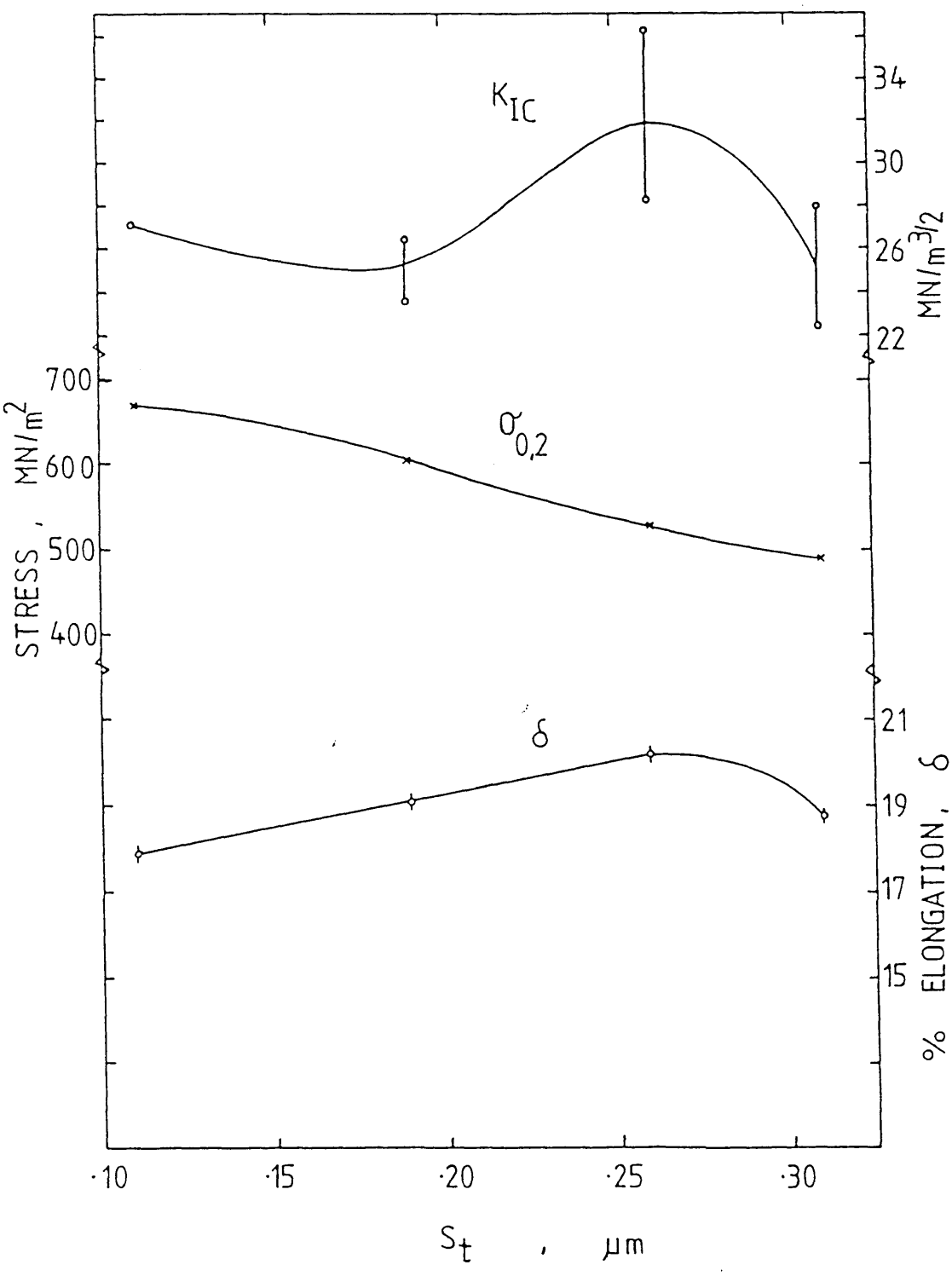


Figure 6.9 The effect of interlamellar spacing $S_t$ on tensile ductility $\delta$ and plane strain fracture toughness $K_{IC}$ in the hypoeutectoid steel.



the effect of interlamellar spacing on $K_{IC}$ and tensile ductility is similar in the two steels studied except in the very coarse pearlitic conditions.

## 6.5 The effect of test temperature on $\sigma_{0.2}$ and $\sigma_f$.

The effect of test temperature on the proof stress and cleavage fracture stress of the hypoeutectoid steel was investigated in the coarse pearlitic condition. Table 6.3 shows the data obtained in the temperature range -50 to -196 °C. As seen, no $\sigma_f$ values were determined at temperatures above -75 °C. This is because at such temperatures the specimens underwent general yield prior to fracture and as such invalidated the Griffiths and Owen (1971) analysis which was used to determine $\sigma_f$.

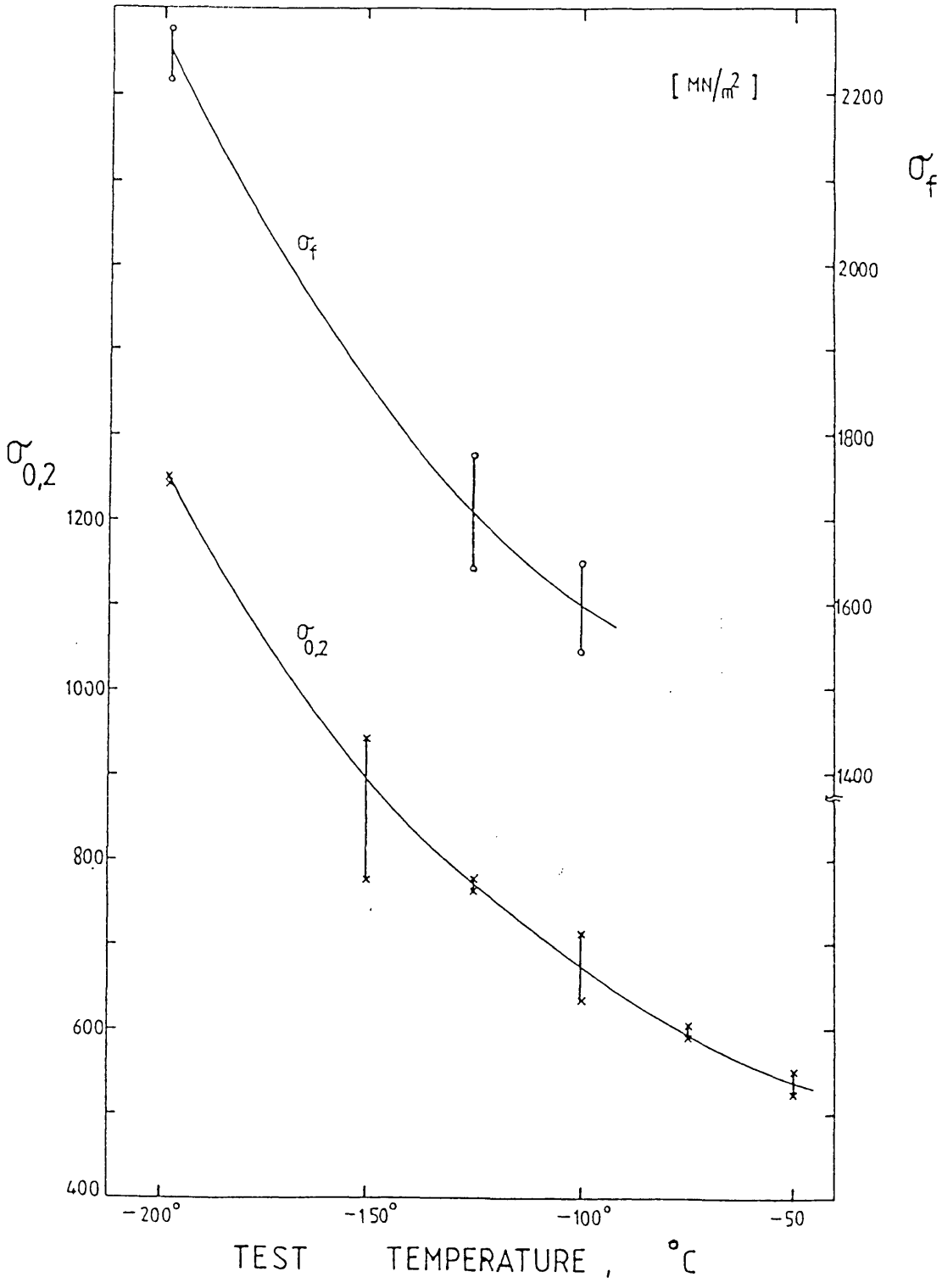
The temperature dependence of $\sigma_{0.2}$ and $\sigma_f$ is plotted in figure 6.10. As expected, the proof stress increases as the test temperature decreases. But the cleavage fracture stress also increases with decreasing test temperature in a manner similar to that observed in the eutectoid steel with a coarse pearlitic microstructure. Since the hypoeutectoid steel was at least 92 % pearlite by volume, it would be expected that the hypoeutectoid and the eutectoid steels would exhibit similar temperature dependencies of $\sigma_{0.2}$ and $\sigma_f$ in both the coarse and fine pearlitic conditions. It was therefore assumed that in the hypoeutectoid steel, $\sigma_f$ would be temperature independent in the fine pearlitic condition.

**Table 6.3** The variation of $\sigma_f$ and $\sigma_{0.2}$ with test temperature for the hypoeutectoid steel in coarse pearlitic condition.

| Specimen | Test Temperature °C | Mean $\sigma_{0.2}$ ($MN/m^2$) (compression) | $\sigma_f$ $MN/m^2$ |
|---|---|---|---|
| HT1 | -50 | 536 | * |
| HT2 | -50 | 536 | * |
| HT3 | -75 | 597 | 1546 |
| HT4 | -75 | 597 | 1510 |
| HT5 | -100 | 672 | 1546 |
| HT6 | -100 | 672 | 1650 |
| HT7 | -125 | 769 | 1776 |
| HT8 | -125 | 769 | 1642 |
| HT9 | -196 | 1250 | 2275 |
| HT10 | -196 | 1250 | 2213 |

* Beyond the validity of the Griffiths & Owen (1971) analysis.

**Figure 6.10 The temperature dependence of $\sigma_{0.2}$ and $\sigma_f$ in the hypoeutectoid steel with a coarse pearlitic microstructure.**



# 7 DISCUSSION OF RESULTS

## 7.1 THE EUTECTOID STEEL

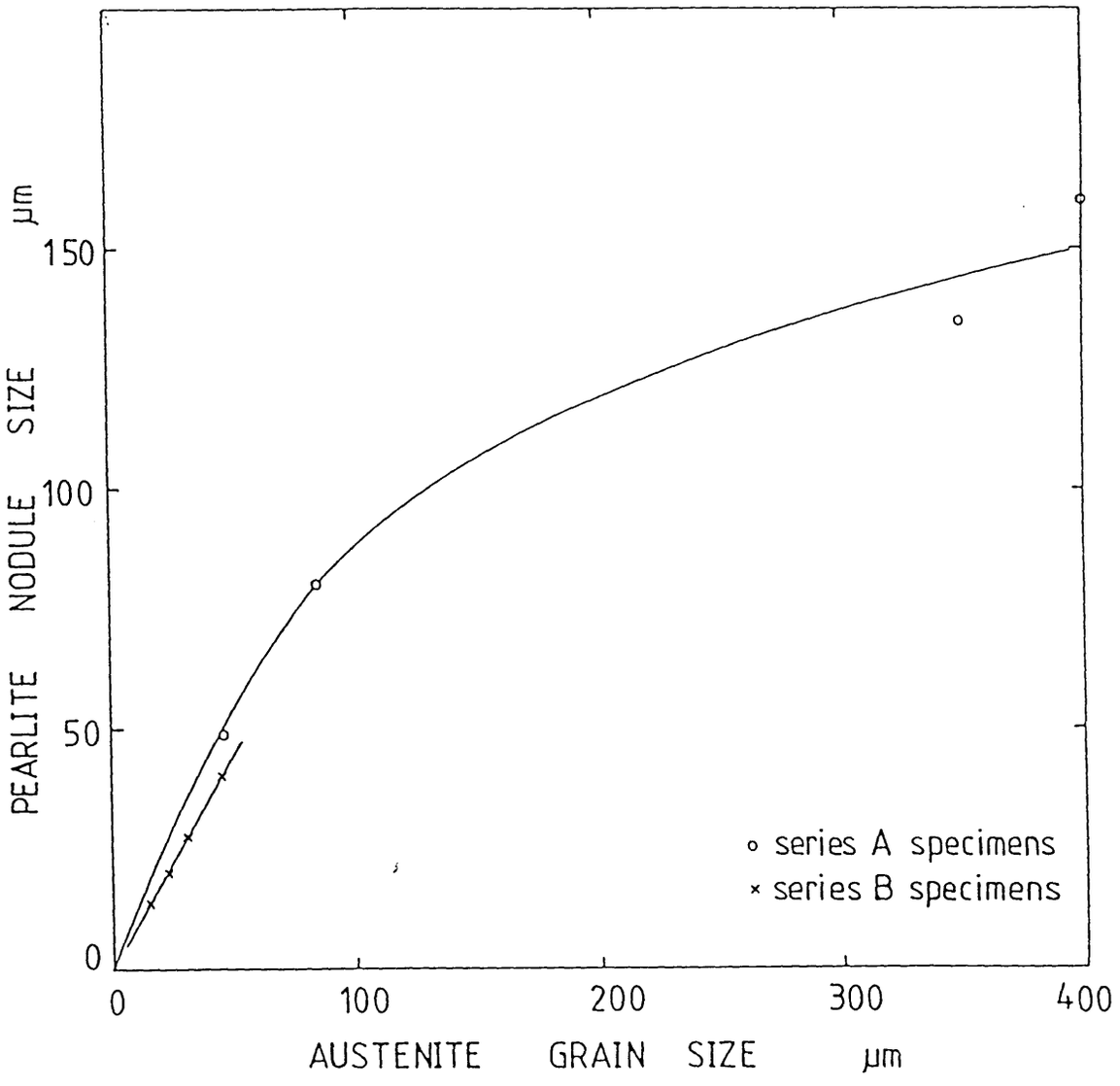
### 7.1.1. The microstructural parameters

The data in table 5.1 show that the prior austenite grain size is the main microstructural parameter which varies with austenitising condition. The pearlite interlamellar spacing is governed by the transformation temperature, and is relatively insensitive to austenitising condition. Increasing the cooling rate, or lowering the isothermal transformation temperature has the same effect of refining the interlamellar spacing.

Little effect of prior austenite grain size on pearlite colony size is observed. This is attributed to the fact that although $\gamma$ grain size controls the initial nucleation rate of pearlite colonies, it has no influence on the rate at which the colonies branch, that is the secondary nucleation rate. The rate at which branching occurs appears to be governed mainly by the transformation temperature. Thus in the series S specimens of table 5.1, we observe that the increase in interlamellar spacing with increasing transformation temperature is accompanied by a corresponding increase in pearlite colony size. A high degree of undercooling is expected to increase the reaction rate so that the rate of secondary nucleation of pearlite colonies increases, resulting in smaller colonies.

The effect of $\gamma$ grain size on pearlite nodule size is shown in figure 7.1. Results from both the A series and B series of specimens have been shown. Each set of data was determined at constant transformation temperature. The data are plotted separately because of the difference in interlamellar spacing between the series A and B specimens. For each set of data, there is a progressive increase in pearlite nodule size as the $\gamma$ grain size increases. The effect is, however, more pronounced in the fine grain regime where the ratio of austenite grain size to pearlite nodule size is approximately 1. The relationship between $\gamma$ grain size and pearlite nodule size would be expected if we appreciate the fact that the rate of pearlite nucleation is governed by the available grain boundary area. Coarse austenite would result in few nucleating sites, and this would provide a larger volume of material over which the secondary

**Figure 7.1** The relationship between the prior austenite grain size and the pearlite nodule size in the fully pearlitic steel.



nucleation of colonies may occur before impingement. Since all the secondary nucleated colonies are related to their primary nucleus, they will constitute a single nodule. When impingement occurs, the resulting nodules will be larger than those generated in fine grain austenite.

It is of note that in figure 7.1 the curve falls off at high values of $\gamma$ grain size. This is attributed to the fact that when the austenite grains are very large there is more time available before the grain-boundary nucleated nodules can impinge. During this time, pearlite may nucleate inside austenite grains and therefore increase the number of pearlite nodules per grain. The result is an increase in the ratio of austenite grain size to pearlite nodule size which is reflected in the falling off of the curve.

### 7.1.2. Proof stress and ultimate tensile stress

#### (i) The effect of interlamellar spacing on proof stress and ultimate tensile stress

The dominant microstructural factor which influences the proof stress and the ultimate tensile stress of pearlitic steels is the interlamellar spacing. A linear relationship is obtained when the proof stress is plotted against $S_t^{-1/2}$, where $S_t$ is the true interlamellar spacing. But as previously observed by Lindbourg (1968), Hyzak and Bernstein (1976), and Bouse et al (1978), the $S_t^{-1/2}$, relationship produces a negative value of friction stress when the usual Hall-Petch yielding equation is assumed. This contradicts the meaning of friction stress as being the stress required to move free dislocations along the slip planes in a crystal. For this reason Marder and Bramfitt (1975) suggested an $S_t^{-1}$ relationship.

The proof stress data obtained in the present work are plotted against $S_t^{-1}$ in figure 7.2. The relationship shown in figure 7.2 suggests that the proof stress of pearlite may be described by the equation :

$$\sigma_{0.2} = \sigma_i + k_y . S_t^{-1} \qquad (7.1)$$

where the friction stress $\sigma_i$ has a value of 400 MN/m$^2$ (at -80 °C) and $k_y$ has a value of 4 x $10^{-5}$ MN/m. Although providing an adequate description of the influence of interlamellar spacing on proof stress, this

equation presents difficulties in physical interpretation. First, the value for the friction stress of 400 $MN/m^2$ at -80 °C which relates to the ferrite constituent of the pearlite is significantly larger than would be expected for a low carbon steel whose microstructure is mainly ferrite. Secondly, there is no obvious physical model that describes the dependence of stress on the inverse of distance.

The mechanism of yielding in pearlite is different to that in most polycrystalline materials due to the lamellar structure. But if we appreciate the fact that the grain size d used in the Hall-Petch equation (eqn. 2.3) is a measure of the mean free slip distance, then it should be possible to describe yielding in pearlite in terms of such a distance. The appropriate microstructural dimension for pearlite should therefore be the mean free distance in the ferrite. This quantity is denoted in table 5.1 by the symbol $\lambda$. In figure 7.3 the present proof stress data have been replotted against $\lambda^{-1/2}$. Again a linear relationship is obtained, but the main difference from that shown in figure 7.2 is that the friction stress at -80 °C is only about 110 $MN/m^2$. This value is now in good agreement with values previously quoted for the friction stress in low carbon steels at similar temperatures (Honeycombe, 1981).

The value of the Hall-Petch constant $k_y$ in figure 7.3 is about 0.30 $MN/m^{3/2}$. This value is in good agreement with that of 0.381 $MN/m^{3/2}$ determined by Bouse et al (1978) from similar microstructures. A typical value of $k_y$ for a low carbon ferritic steel is predicted by figure 2.7 to be about 0.75 $MN/m^{3/2}$. A higher value would be expected in a low carbon ferritic steel if we interpret the quantity $k_y$ as a measure of the local stress intensity which has to be attained at the tip of an arrested slip band in order to nucleate slip in the adjacent grain. In a low carbon steel, dislocations must be generated at the grain boundary before yield can spread from one grain to another. In a fully pearlitic steel, a cementite lamella must be fractured before yield can spread from one ferrite lamella to another. Because cementite is a brittle phase, it is reasonable to assume that it would crack at a lower local stress intensity than that required to spread yielding across a grain boundary in a polycrystalline low carbon steel. This would therefore result in the low value of $k_y$ observed in pearlitic steels.

Figure 7.2 The dependence of the proof stress $\sigma_{0.2}$ on the inverse of true interlamellar spacing ($S_t^{-1}$).

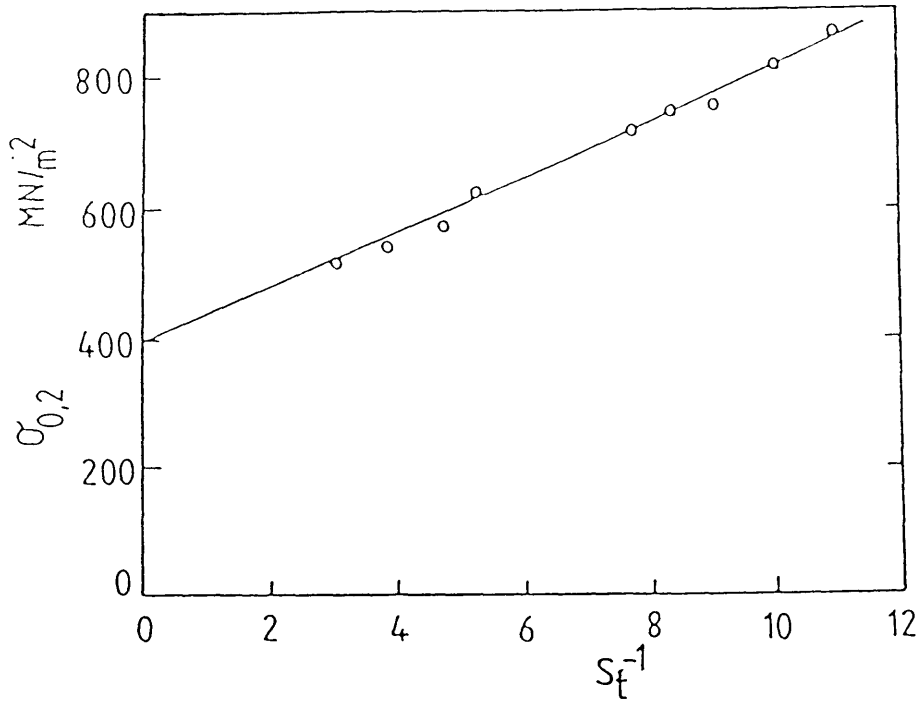
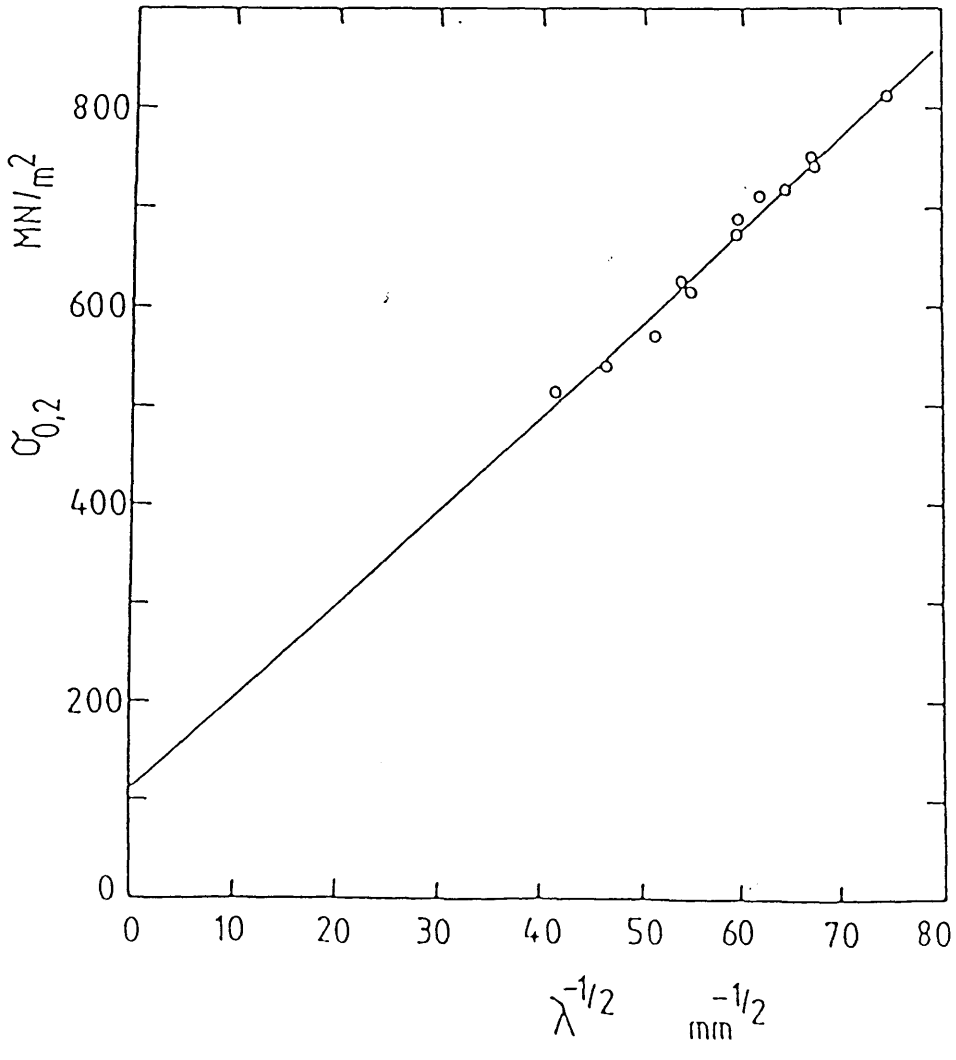



Figure 7.3 The dependence of the proof stress $\sigma_{0.2}$ on the inverse square root of the mean free distance in pearlitic ferrite ($\lambda^{-1/2}$)



Having established the microstructural quantity that controls yielding in pearlite, the proof stress may be expressed by the following Hall-Petch equation:

$$\sigma_{0.2} = \sigma_i + k_y . \lambda^{-1/2} \qquad (7.2)$$

where $\sigma_i$ is the lattice friction stress of ferrite, $k_y$ is the Hall-Petch constant in pearlite, and $\lambda$ is the mean free distance in the pearlitic ferrite.

**(ii) The effect of austenitising conditions on proof stress and ultimate tensile stress**

The prior austenite grain size was used to compare the effects of varying austenitising conditions on proof stress and ultimate tensile stress. The proof stress and ultimate tensile stress data are plotted against $\gamma$ grain size in figure 5.5a for grain sizes in the range 15 to 400 $\mu$m. As the grain size increased from 15 to about 45 $\mu$m, corresponding to austenitizing temperatures of 800 to 900 °C, the proof stress progressively increased to a peak value. As can be seen in table 5.1, the interlamellar spacing decreased slightly over this range of austenitising temperatures, and the associated change in ferrite mfd could account for about 50 % of the observed increase in strength. The decrease in interlamellar spacing is due to the fact that the TTT curve of the steel is shifted to the right as the austenite grain size increases, thus allowing transformation to occur at lower temperatures. The other factor that could contribute to the increase in strength was the progressively increasing degree of homogeneity of the austenite as the austenitising temperature was raised. The specimen which was austenitized at 750 °C for half an hour had the lowest strength as a consequence of the high degree of inhomogeneity that would be expected due to the low temperature and short austenitising time.

The range of austenite grain sizes from 15 to 45 $\mu$m was further studied by the series B specimens. These were heat treated in molten salt baths, rather than in fluidised beds. The strength data of these specimens which are shown in figure 5.6 display a less rapid increase in proof stress and ultimate tensile stress as the austenite grain size

increases. This behaviour led to the conclusion that the strength values of specimen A1 in table 5.2 were anomalously low. This would be consistent with the microstructure of specimen A1 in figure 7.4 which shows a mixed microstructure indicative of incomplete transformation. The series B specimens have higher strength values than the corresponding specimens in the A series because they have finer pearlitic spacings.

For grain sizes above 45 $\mu m$, which corresponds to austenitising temperatures above 900 °C, strength decreases to a minimum value, and then increases again. This variation in strength is associated with the corresponding variation in interlamellar spacing. The increase in strength in the very coarse grain conditions is however consistent with the increase in hardenability observed in steels as the austenite grain size increases. During the pearlite transformation, nucleation occurs mainly on prior austenite grain boundaries. As the grain size increases, the number of nucleating sites per unit volume decreases, and thus the rate of transformation is lowered. This behaviour is normally accompanied by a higher degree of undercooling prior to transformation and a reduction in the amount of heat evolved during the pearlite reaction (see figure 7.5). This implies the temperature at which most transformation would occur is lowered if fixed cooling conditions are assumed. The result is a decrease in interlamellar spacing and an increase in proof stress. In figure 5.5a this effect is most pronounced in the very coarse grain regime, typically 250 to 350 $\mu m$ .

The data in figure 5.5b were intended to show whether the influence of austenitising conditions on strength shown in figure 5.5a would be reproduced under different testing conditions and different test temperatures. Whilst the heat treatment pertaining to the data in figure 5.5a involved isothermal transformation, the data in figure 5.5b were obtained from specimens subjected to continuous cooling transformation. All the specimens had been normalized from the austenitising temperatures shown. The holding time was 1 hour throughout. The specimens were heat treated in their final machined condition in an argon atmosphere. Since the specimens were small (4.54 mm diameter, 16 mm gauge length), they were expected to have a fully homogeneous microstructure. The strength data which were obtained at room temperature are plotted against the austenitising temperatures. As in figure 5.5a, we observe a similar trend where strength increases to a

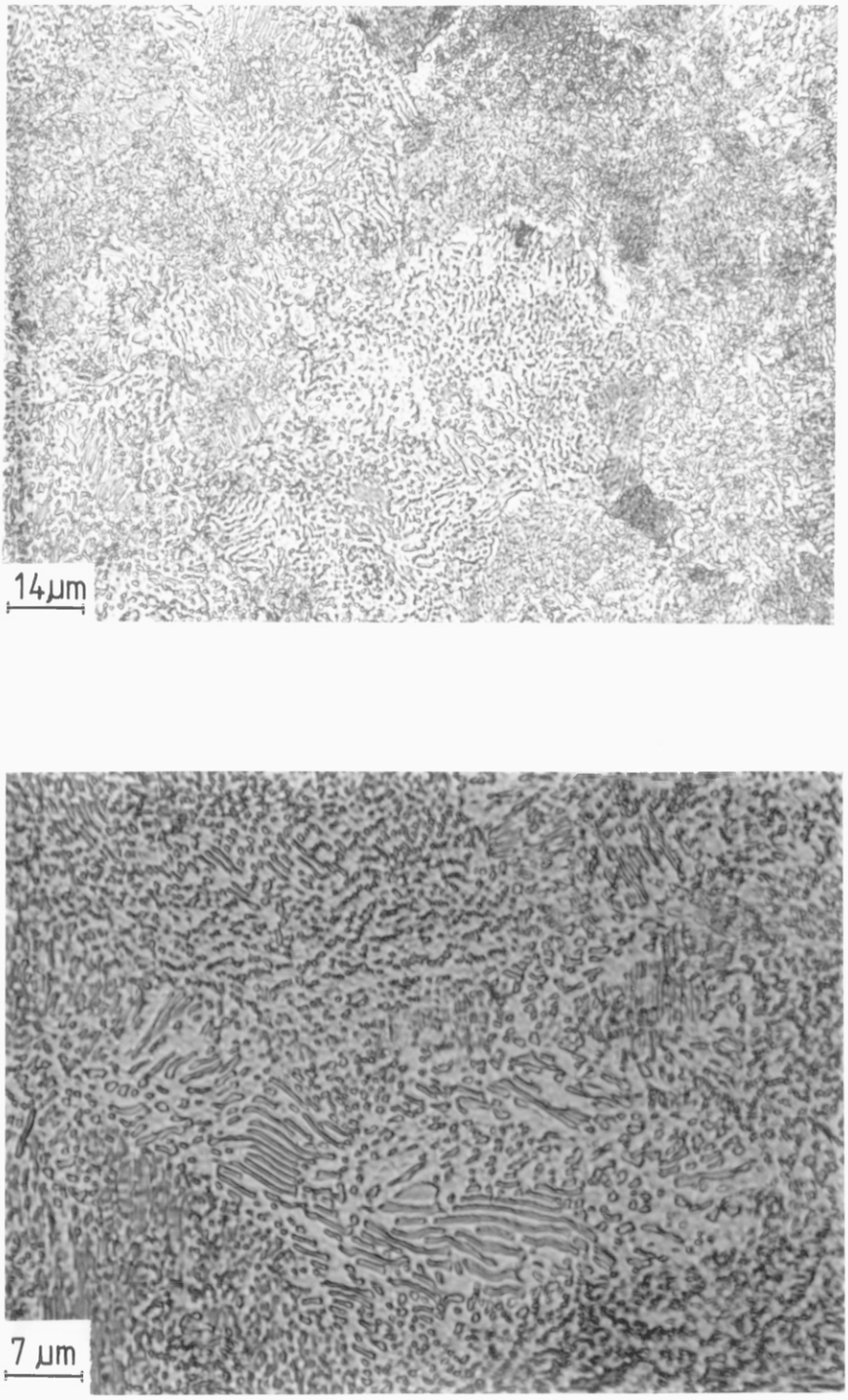
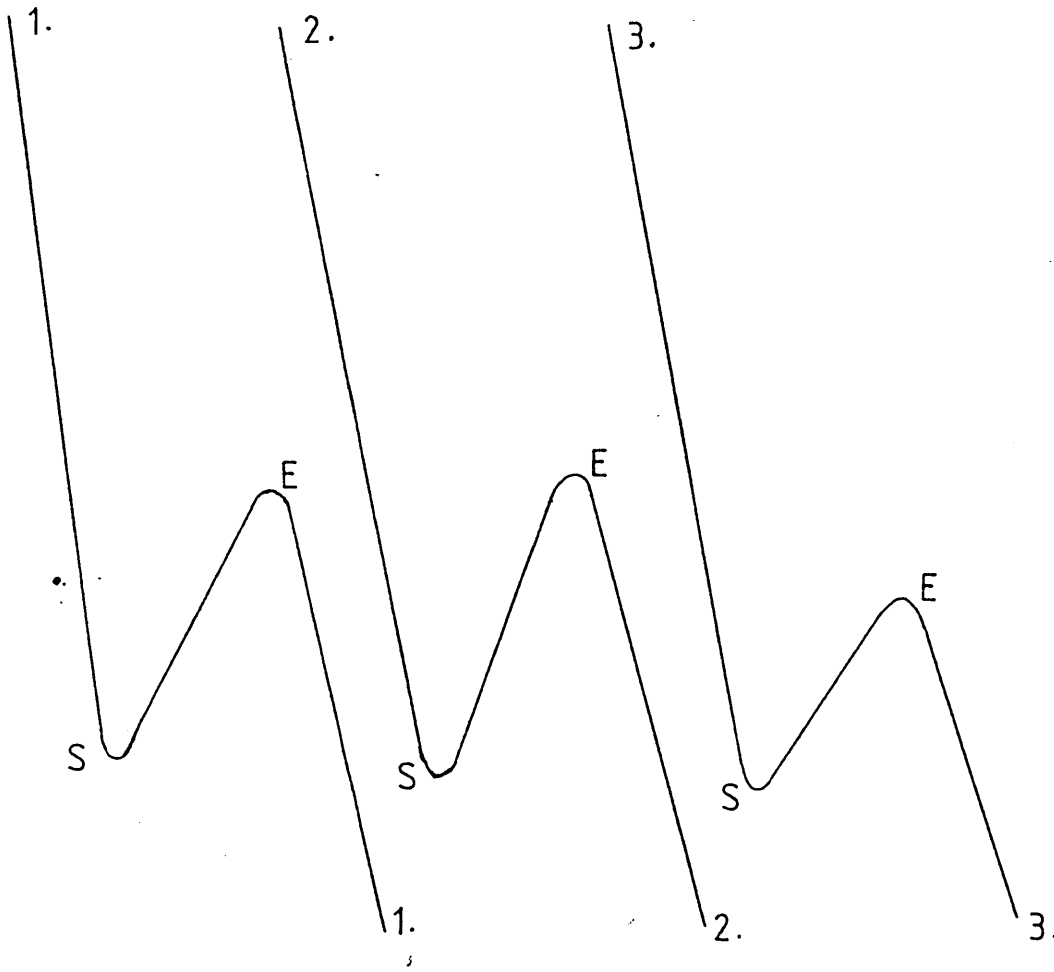



FIGURE 7.4

The microstructure of specimen A1 showing a mixture of spheroidised and lamellar pearlite

**Figure 7.5 Cooling curves of 25 mm specimens austenitised at different temperatures and then quenched into a fluidised bed at 640 °C (± 5°).**




| | Austenitising Temp. °C | Transformation-Start Temp. °C (S) | Transformation-End Temp. °C (E) | ΔT °C |
|---|---|---|---|---|
| 1. | 900 | 642 | 659 | 17 |
| 2. | 1000 | 640 | 661 | 21 |
| 3. | 1200 | 638 | 654 | 16 |

peak value as the temperature is raised from 750 to 850 °C. Beyond this temperature, strength decreases to a minimum at an austenitising temperature of about 1100 °C. After this, strength increases again. It appears therefore, that the observed relationship in figure 5.5a is reproducible.

### 7.1.3 The cleavage fracture stress $\sigma_f$

#### (i) Microstructural dependence of $\sigma_f$

The cleavage fracture stress is a measure of the local stress required to produce unstable cleavage fracture at a particular fracture sensitive location in a microstructure. Since yielding must precede cleavage in steels, the cleavage fracture stress is always greater than, or equal to the uniaxial yield stress of the material. In addition, whereas yielding may occur under either tensile of compressive stresses, cleavage fracture can only be caused by tensile stresses. Cleavage fracture involves the nucleation and subsequent propagation of a microcrack. Propagation can occur only if the tip of the microcrack is loaded in an opening mode, i.e. in tension.

Figures 5.5a, 5.6 and 5.8 show the dependence of $\sigma_f$ on prior austenite grain size and pearlite interlamellar spacing. The most noticeable feature of these data is that the cleavage fracture stress parallels the 0.2% proof stress for all of the conditions tested. This would suggest that in pearlite, $\sigma_f$ and $\sigma_{0.2}$ are controlled by the same microstructural features. However, before a firm conclusion can be made, it is necessary to explore other testing conditions that may influence $\sigma_f$ and $\sigma_{0.2}$. It should be remembered that in low carbon mild steels $\sigma_f$ and $\sigma_{0.2}$ appear to be controlled by the same microstructural parameter, i.e. ferrite grain size. But in fact they are controlled by different parameters (carbide size and grain size respectively) which happen to be related as shown by Curry and Knott (1976). The difference between $\sigma_{0.2}$ and $\sigma_f$ becomes apparent in low carbon mild steels when the test temperature is varied. The shear stress controlled proof stress increases with decreasing test temperature because of the temperature dependence of the friction stress. The tensile-stress-controlled cleavage fracture stress, on the other hand, is mainly temperature independent. The cleavage fracture stress is then

interpreted as a Griffith fracture stress where the initiating microcrack is a cracked carbide particle. Although the carbide crack is nucleated by a shear mechanism, involving dislocation pile-ups in the neighbouring ferrite, the cleavage fracture stress is controlled by the unstable propagation of the crack, which is determined by the magnitude of the tensile stress. In order to obtain a better understanding of the relationship between $\sigma_{0.2}$ and $\sigma_f$ in pearlitic steels, it is necessary to consider the effect of test temperature.

**(ii) The temperature dependence of $\sigma_f$ and $\sigma_{0.2}$**

Table 5.3 and figures 5.10 and 5.11 show the effect of test temperature on $\sigma_f$ and $\sigma_{0.2}$ for coarse and fine pearlitic microstructures. The two microstructures were studied separately because there was strong evidence from the literature (Langford, 1977; Porter et al, 1978; Lewandowski and Thompson, 1984) that coarse and fine pearlite may behave differently as far as cleavage fracture is concerned.

The present data show that in coarse pearlite, where the interlamellar spacing is more than about 0.15$\mu$m, both $\sigma_{0.2}$ and $\sigma_f$ increase with decreasing test temperature. The correlation between $\sigma_{0.2}$ and $\sigma_f$ given in figure 5.12 suggests that up to a cleavage fracture stress of about 2100 MN/m$^2$, $\sigma_f$ is directly proportional to $\sigma_{0.2}$, the constant of proportionality being about 2.4. Since yielding is a temperature-dependent shear process, it can be assumed that cleavage fracture in these microstructures also involves a shear process. This strongly suggests that microstructural features which control $\sigma_{0.2}$ in coarse pearlite also control $\sigma_f$.

In fine pearlite, $\sigma_f$ appears to be unrelated to $\sigma_{0.2}$. As the test temperature decreases, the proof stress $\sigma_{0.2}$ increases, but the cleavage fracture stress $\sigma_f$ remains constant. The temperature independence of $\sigma_f$ in fine pearlite suggests that cleavage fracture is tensile stress controlled. This means a critical value of tensile stress must be attained before cleavage propagation can occur, although the nucleation stage may involve a shear process.

The observed effects of temperature on $\sigma_f$ suggest that there is a fundamental difference in the micromechanism of cleavage fracture in coarse and fine pearlite. It should be noted however that whatever the micromechanism involved, the final fracture in these microstructures is always transgranular cleavage. For this reason, the appearance of the fracture surfaces does not indicate any obvious effect of interlamellar spacing on the cleavage fracture process. The micromechanisms of cleavage fracture in pearlite are discussed in detail in the next section.

### 7.1.4 The micromechanisms of cleavage fracture in pearlite.

#### (i) Coarse pearlite

Langford (1977) and Porter et al (1978) suggested that the dominant deformation mechanism in coarse pearlite is the formation of localised slip bands which may traverse complete pearlite colonies. Dislocation pile-ups in the ferrite lamellae impinge on the adjacent cementite lamellae and cause them to crack. This deformation is similar to the inhomogeneous slip which causes carbide cracking and the nucleation of cleavage fracture in mild steels as proposed by Smith (1966). The difference between mild steel and coarse pearlite is that in the former the cleavage fracture stress is independent of test temperature, whereas in the latter $\sigma_f$ increases with decreasing test temperature.

The temperature independence of the cleavage fracture stress in low carbon steels suggests a propagation-controlled cleavage process. A critical tensile stress is required to cause the carbide-initiated crack nucleus to propagate into the neighbouring ferrite matrix. The cleavage fracture stress can then be related to the carbide size by the Griffith equation for a plate-like carbide as follows:

$$\sigma_f = \left[\frac{4E.\gamma_p}{\pi(1-\nu^2)Co}\right]^{1/2} \qquad (7.3)$$

where E is Young's modulus, $\gamma_p$ the effective surface energy of ferrite, $\nu$ Poisson's ratio and $C_o$ is the carbide thickness. This equation is similar to equation 3.4b. Each of the quantities in this equation is relatively

insensitive to temperature, and thus $\sigma_f$ is also temperature insensitive. The fact that $\sigma_f$ is temperature dependent in coarse pearlite is indicative of a different micromechanism of cleavage fracture.

A cleavage fracture stress in pearlite may be calculated from equation 7.3 using the known values of the constants and measured values of carbide thickness. The iron carbide lamellae in pearlite are significantly thinner than the carbides found in low carbon mild steels. The average thickness of cementite lamellae in the coarse pearlitic condition was found to be about 0.03 $\mu$m. If this value is inserted in equation 7.3, together with typical values of 207 x $10^3$ MN/m$^2$ for E, 14 J/m$^2$ for $\gamma_p$, and 0.3 for $\nu$, the calculated value of $\sigma_f$ is about 11,600 MN/m$^2$. This is much larger than the measured values of $\sigma_f$ for coarse pearlite which were in the range 1507 to 2315 MN/m$^2$. It follows that if an individual lamellar carbide, or even an array of lamellae was to crack under the influence of an impinging slip band, the resultant microcracks would be too small to cause unstable propagation. The cracks would blunt in the ferrite and remain as a stable array of microcracks. The existence of such an array of stable microcracks prior to the onset of cleavage fracture has been verified and demonstrated using the double notched specimens (figures 5.17 and 5.18)

The presence of the cracked carbide lamellae as shown in figure 5.18 encourages plastic deformation to remain concentrated in the original shear band. As a result, the carbide-initiated microvoids can undergo ductile shear linking to form a larger microcrack. This process is the same as that referred to as shear cracking of pearlite (figure 3.12) by Miller and Smith (1970). When the microcrack attains a critical size, it can then propagate as an unstable cleavage crack. This mechanism implies that cleavage fracture in coarse pearlite is caused by a crack nucleus which is formed by a predominantly fibrous process. This was confirmed when fracture surfaces were studied in the scanning electron microscope. As shown in figure 7.6a, a fibrous fracture facet was found to be located adjacent to the tip of a fatigue pre-cracked specimen. All of the surrounding facets are fully cleavage. The fibrous facet is shown in more detail in figure 7.6b where the carbide-nucleated microvoids are better revealed.

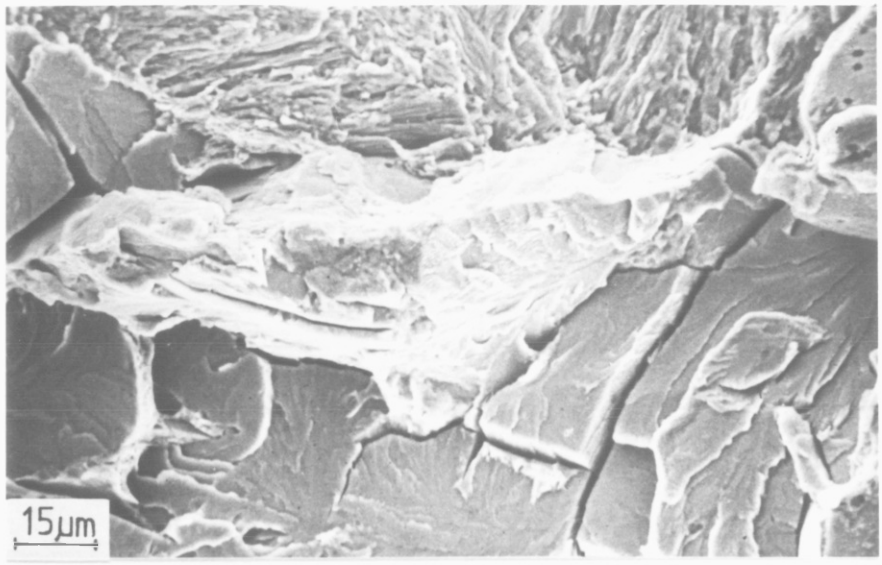



FIGURE 7.6a

A fibrous fracture facet located below the tip of a fatigue crack in the eutectoid steel.




FIGURE 7.6b

The fibrous fracture facet in Figure 7.6a reveals the carbide-nucleated microcracks at high magnifications.

An essential requirement for a propagation-controlled cleavage mechanism is that crack nucleation should be easier than crack propagation. This situation usually exists in the case of mild steels because the surface energy of the brittle carbide is significantly lower than the effective surface energy of the ferrite. If, as is suggested for coarse pearlite, the initial carbide crack is stable, then the subsequent formation of the critical crack nucleus must involve plastic deformation of the ferrite. Under these circumstances crack nucleation is more difficult than the subsequent propagation and fracture becomes nucleation-controlled. A triaxial state of stress ahead of the notch root is however still necessary in order to provide the high value of tensile stress necessary for crack propagation. Because of the need for continued plastic deformation to develop the enlarged ferrite plus carbide crack nucleus, the tensile stress ahead of the notch root is expected to approach the maximum constrained value for yielding before unstable cleavage can occur. This is borne out by the observation that the measured values of cleavage fracture stress for coarse pearlite are all about 2.4 times the uniaxial proof stress.

**(ii) Coarse pearlite tested at -196 °C**

The $\sigma_f$ values obtained at -196 °C from specimens with a coarse pearlitic microstructure no longer maintained the same relationship with the proof stress as was observed at higher test temperatures. The $\sigma_f$ values were about 2300 $MN/m^2$ which is only about 1.6 times the proof stress. This difference in the degree of constraint from the near constant value of 2.4 at higher temperatures implies a change in the micromechanism of cleavage fracture and may suggest that with the higher stresses available at -196 °C, cleavage becomes propagation-controlled. The measured $\sigma_f$ value is still less than the calculated value of 11,600 $MN/m^2$ for propagation from a single lamellar carbide. This suggests either that propagation occurs preferentially from a particularly large carbide or more probably that the stress fields from a number of adjacent cracked carbides interact to form a larger effective crack size. The important difference from the fracture mechanism proposed for the higher temperature regime is that the crack nucleus is now confined to the carbide particles and hence cleavage can be propagation-controlled.

**(iii) Fine pearlite**

Fine pearlite exhibited $\sigma_f$ values which were independent of test temperature. As in the case of mild steel, this is indicative of a propagation-controlled cleavage mechanism. Since the thickness of the carbide lamellae in fine pearlite is even smaller than in coarse pearlite, a single cracked carbide lamella cannot be expected to initiate cleavage fracture. However, the mechanism of plastic deformation and carbide cracking in fine pearlite is different from that in coarse pearlite and may be responsible for the observed difference in cleavage behaviour.

Langford (1977) and Porter et al (1978) observed that fine pearlite does not exhibit inhomogeneous deformation and does not undergo shear cracking as is predominant in coarse pearlite. They observed that the ferrite deformed by fine scale slip and that the cementite appeared to fail by a fibre loading mechanism. Under these circumstances crack nucleation is expected to occur in a pearlite colony which is aligned parallel to the direction of the maximum principal stress. When a carbide particle fails by a fibre loading mechanism the elastic strain energy in the fibre is released over a distance equal to half the critical fibre length on either side of the fracture (Lindley et al, 1970).

Calculation shows that the elastic energy released is at least 10 times greater than the energy required to form the fracture surface in the carbide. The excess energy is then available to drive the carbide-nucleated microcrack into the ferrite on either side of the carbide lamella. In this way, a crack nucleus can be generated which may be much larger than the thickness of the cracked carbide. An individual crack formed in this way may be of sufficient size to cause unstable fracture under the influence of the triaxial stress state ahead of the notch root. Alternatively, the cracking of one cementite lamella may trigger the failure of the similarly stressed cementite lamellae on either side. Such cracking of adjacent carbides in fine pearlite is evident in the work of Porter et al (1978). If a number of lamellae were to break simultaneously, the resultant microcrack would be sufficient to permit unstable propagation, and the cleavage fracture stress would then be consistent with that determined experimentally.

The mechanism proposed for the cleavage fracture of fine pearlite involves a strain-controlled nucleation event, but the critical stage is the propagation of the nucleus which depends on the magnitude of the tensile stress. It follows that cleavage fracture in fine pearlite is propagation-controlled. The cleavage fracture stress is therefore not expected to show a significant variation with testing temperature. This is borne out experimentally both in the present work and in the work of Lewandowski and Thompson (1984).

The two micromechanisms of cleavage fracture discussed above imply that as the interlamellar spacing is refined, there should be a transition from nucleation-controlled to propagation-controlled cleavage. A similar transition is observed with coarse pearlite when the testing temperature is lowered. Figure 5.12 shows that the transition from nucleation-controlled to propagation-controlled cleavage fracture occurs at a $\sigma_f$ value of about 2100 $MN/m^2$.

It may be concluded from the above observations that the micromechanisms of cleavage fracture in pearlite depend on strength. For $\sigma_f$ values less than about 2100 $MN/m^2$, the stress required to satisfy the Griffith crack propagation criterion for a single carbide is much larger than the constrained yield stress $m\sigma_{0.2}$ where the constraint factor m is shown in figure 5.12 to be about 2.4. Since the maximum stress available is limited to the constrained yield stress, the first-formed carbide microcrack is stable and must continue to grow by the failure of both ferrite and cementite lamellae until the critical size is attained to allow propagation. Cleavage fracture under these conditions is therefore nucleation-controlled. For $\sigma_f$ values greater than or equal to 2100 $MN/m^2$, the Griffith propagation stress is less than or equal to 2.4 times the proof stress since unstable propagation occurs from adjacent carbide microcracks. This then allows for the normal propagation-controlled cleavage fracture.

### 7.1.5 Plane strain fracture toughness $K_{IC}$

Apart from the cleavage fracture stress, two other fracture parameters were studied in the present work. These are the plane strain fracture toughness and the tensile ductility, measured as the % elongation at fracture. In pearlitic steels, all three fracture parameters refer to the same mode of fracture, namely cleavage. However, they refer to different features of the fracture process. As noted previously, the cleavage fracture stress is a measure of the local stress required to produce unstable cleavage fracture at a particular fracture sensitive location in a microstructure. The plane strain fracture toughness is a macroscopic criterion for the unstable propagation of a pre-existing crack in an elastically loaded test piece. The tensile ductility is a measure of the susceptibility to fracture in an initially defect-free test piece which fails after general yield. Whilst these parameters may be related to each other, the relationship is sometimes very complex, and as it will be seen in section 7.1.6 where the tensile ductility is discussed, the plane strain fracture toughness and the tensile ductility exhibit opposite effects with respect to changes in interlamellar spacing.

#### (i) The effect of austenitising conditions on $K_{IC}$

It can be seen in figure 5.7 that the plane strain fracture toughness showed very little variation with $\gamma$ grain size over the range of grain sizes studied. The present observations are contrary to previous reports of a significant effect of austenite grain size on Charpy impact toughness and dynamic fracture toughness $K_{ID}$ (Hyzak and Bernstein, 1976; Bouse et al, 1978). However, consideration of the extent of the crack tip stress field demonstrates that it is unlikely the austenite grain boundaries could influence the fracture process in sharply cracked test pieces. Table 7.1 shows the size of the crack tip plastic zone calculated from the relationship:

$$r_p = \frac{1}{6\pi}\left[\frac{K_{IC}}{\sigma_{0.2}}\right]^2 \qquad (7.4)$$

In the A series of specimens, the plastic zone size varied from about 90 to 170 $\mu$m. But the fracture process in a sharp notch situation would take place in a much smaller process zone, typically about one tenth of the

plastic zone size (Rice and Johnson, 1970). For the series of tests under consideration this process zone lies in the range 9 to 17 $\mu$m. If this dimension is compared with the austenite grain size which had a minimum value of 15 $\mu$m and a maximum value of 400 $\mu$m, it can be seen that the austenite grain boundaries can hardly interact with the crack tip process zone. Hence prior austenite grain size is unlikely to have a direct influence on $K_{IC}$.

**(ii) The effect of interlamellar spacing on $K_{IC}$**

Figure 5.9 shows the effect of interlamellar spacing on fracture toughness. As the interlamellar spacing decreases, the fracture toughness first decreases and then increases for the finest spacing . The minimum value of $K_{IC}$ occurs at an interlamellar spacing of about 16 $\mu$m. Preston (1980) observed a similar relationship between $K_{IC}$ and interlamellar spacing, with the minimum $K_{IC}$ occuring at about the same value of interlamellar spacing. This behaviour reflects the effect of interlamellar spacing on slip behaviour and cleavage fracture stress already discussed in the last section, and would appear to be related to the change in the micromechanism of cleavage fracture nucleation.

It has been postulated that in order for cleavage fracture to occur, the cleavage fracture stress must be attained over a characteristic distance X, ahead of the crack tip (Ritchie et al, 1973). This suggests that $K_{IC}$ should be dependent on both the cleavage fracture stress $\sigma_f$ and the distance X. This distance can therefore be calculated from measured values of $K_{IC}$ and $\sigma_f$. Figure 7.7 shows the relationship between the stress intensification R and the dimensionless quantity $X/(K/\sigma_o)^2$, where $\sigma_o$ is the flow stress and K is the stress intensity factor. Values of X which were calculated from the measured values of $\sigma_f$, $\sigma_{0.2}$ and $K_{IC}$ are shown in table 7.1.

Ritchie et al suggested that the characteristic distance in mild steels was of the order of two ferrite grain diameters. But further work by Curry and Knott (1976) showed that the proportionality constant between X and grain size changes as the grain size is varied. They attributed this to the distribution of carbides in their material, and concluded that no physical significance could be placed on the characteristic distance. The present

data suggest that the characteristic distance in pearlite varies with pearlite nodule size (table 7.1). The variation is however, not a simple one, since X varies from about a half to two and a half nodule diameters. A notable feature of the characteristic distance, however, is that it is proportional to the plastic zone size, the proportionality constant being about a half.

### 7.1.6 Tensile Ductility

Whereas prior austenite grain size has small influence on $K_{IC}$ and the cleavage fracture stress, it does have a very pronounced effect on the tensile ductility (figure 5.7). These observations demonstrate that the prior austenite grain size has no effect on either the micromechanism of cleavage fracture, or the macroscopic fracture instability condition. The notable feature of the fracture process, however, is an inverse relationship between tensile ductility and cleavage facet size. The cleavage facet size, F is recorded in table 7.1 where it can be seen that the facet size increases in proportion to the austenite grain size and the pearlite nodule size.

When uniaxial tensile tests were performed, it was observed that most specimens failed without passing through a necking instability. The fracture process consisted of a regime of uniform plastic strain which was interrupted by sudden cleavage fracture. This suggests that in a tensile test, the steel undergoes post-yield quasi-brittle instability. As discussed earlier, except in the case of fine pearlite, deformation of the steel is associated with slip in localized bands which cause the multiple shear cracking of the cementite lamellae in a pearlite colony. Miller and Smith (1970) showed that continued plastic strain in a tensile test causes this array of carbide cracks to join by a ductile coalescence mechanism and form larger cracks which may then act as cleavage nuclei. To obtain an indication of the size of such a crack which would be necessary to initiate a brittle fracture in the tensile test, it is necessary to follow a post-yield approach to brittle fracture such as crack opening displacement (Harrison, 1980).

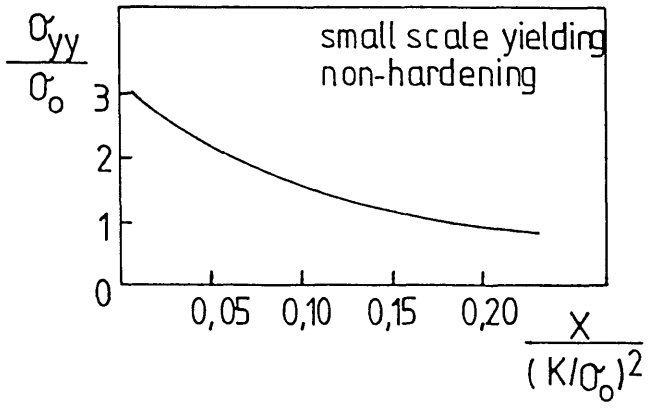
Where, as in the present case, the fracture strain $\epsilon_f$ exceeds the yield strain $\epsilon_y$, the following relationship has been proposed to relate the

**Table 7.1 Calculated values of the plastic zone size $r_p$ and the characteristic distance for fracture X in the eutectoid steel. Values of the cleavage facet size, F are also included.**

| Specimen | γ-grain size(μm) | Nodule size(μm) | $\sigma_{o.z}$ MN/m² | $K_{IC}$ MN/m$^{3/2}$ | $\frac{\sigma_f}{\sigma_{o.z}}$ | $r_p$ μm | X μm | F μm |
|---|---|---|---|---|---|---|---|---|
| A1 | 15 | * | 494 | 27.9 | 2.44 | 169 | 96 | * |
| A2 | 45 | 48 | 676 | 27.7 | 2.33 | 89 | 59 | 46 |
| A3 | 84 | 80 | 618 | 30.3 | 2.39 | 127 | 72 | 84 |
| A4 | 350 | 135 | 717 | 30.6 | 2.31 | 97 | 63 | 150 |
| A5 | 400 | 160 | 694 | 30.4 | 2.20 | 102 | 77 | 171 |
| B1 | 15 | 14 | 721 | 29.1 | 2.50 | 86 | 37 | 11 |
| B2 | 22 | 20 | 748 | 27.6 | 2.55 | 72 | 27 | 25 |
| B3 | 31 | 28 | 754 | 34.9 | 2.50 | 114 | 49 | 33 |
| B4 | 45 | 40 | 818 | 28.9 | 2.39 | 66 | 31 | 37 |
| S0 | 45 | 40 | 818 | 28.9 | 2.39 | 66 | 31 | 37 |
| S1 | 45 | 40 | 630 | 25.1 | 2.36 | 84 | 43 | 43 |
| S2 | 45 | 56 | 546 | 29.8 | 2.43 | 158 | 71 | 70 |
| S3 | 45 | 80 | 519 | 34.5 | 2.41 | 234 | 108 | 86 |
| AR | 48 | 40 | 573 | 26.5 | 2.45 | 113 | 51 | 33 |

* not determined.

**Figure 7.7 The variation of the stress intensification R ($\sigma_{yy}/\sigma_o$) with the dimensionless quantity $X/(K/\sigma_o)^2$, where X is the characteristic distance for fracture.**



crack opening displacement toughness $\delta_c$ and the nominal fracture strain to the maximum tolerable defect size, $a_t$:

$$\frac{\delta_c}{2\pi . \epsilon_y . a_t} = \frac{\epsilon_f}{\epsilon_y} - 0.25 \qquad (7.5)$$

In the case of a tensile test on a pearlitic steel, the fracture strain is much larger than the yield strain, and as such the quantity 0.25 can be neglected.

The C.O.D. toughness $\delta_c$ may be estimated from the $K_{IC}$ results using the relationship :

$$K_{IC}^2 = E\ \sigma_y\ \delta_c \qquad (7.6)$$

The tolerable defect size is then given by:

$$2a_t = \frac{K_{IC}^2}{\pi . E . \sigma_y . \epsilon_f} \qquad (7.7)$$

The quantity $a_t$ relates to an idealised through-crack in an infinite plate. Assuming that the internal crack in a tensile specimen can be considered as a penny-shaped crack, then the appropriate LEFM shape factor can be incorporated to give the following expression for the real tolerable defect size 2a:

$$2a = \frac{\pi K_{IC}^2}{4E . \sigma_y . \epsilon_f} \qquad (7.8)$$

It should be noted that equation (7.5) was developed primarily for the purpose of design and defect assessment in steel structures. As such, it is a lower bound to the experimental data, and the calculated tolerable defect sizes are quite conservative. The actual critical defect size at failure is found to be 2 to 3 times greater than the calculated tolerable values (Harrison 1980).

Table 7.2 shows calculated values of 2a for the series A specimens. Values of prior austenite grain size, pearlite colony size and pearlite nodule size are included for comparison. Bearing in mind that the actual defect size may be 2 to 3 times greater than the calculated values, it

can be seen that there is broad agreement between the nodule size and/or the austenite grain size and the size of defect necessary to initiate a quasi-brittle fracture in the tensile test. By comparison, the pearlite colony size is much too small to contain the initial defect, and does not show any systematic variation with the tensile ductility. As discussed earlier, all the pearlite colonies in a single nodule have the same crystallographic orientation, and hence it is reasonable that a slip-nucleated microcrack could extend through the full width of the nodule rather than being restricted to a single colony. This is borne out by the fracture appearance where the cleavage facet size is found to be similar to the pearlite nodule size. It is concluded that the ductility in the tensile test can be interpreted as the strain necessary to develop a nodule-size microcrack and cause it to propagate as an unstable cleavage crack.

**Table 7.2 Calculated values of the critical crack size (2a) for cleavage fracture in the tensile specimens**

| Specimen | $\sigma_y$ MN/m$^2$ | $K_{IC}$ MN/m$^{3/2}$ | $\epsilon_f$ ln(1+δ) | 2a μm | C μm | N μm | $\gamma$ μm |
|---|---|---|---|---|---|---|---|
| A2 | 676 | 27.7 | .146 | 28 | 10.0 | 48 | 45 |
| A3 | 618 | 30.3 | .113 | 50 | 11.0 | 80 | 84 |
| A4 | 717 | 30.6 | .046 | 106 | 9.5 | 135 | 350 |
| A5 | 694 | 30.4 | .035 | 141 | 10.5 | 160 | 400 |

## 7.2 THE HYPOEUTECTOID STEEL

### 7.2.1 The microstructural parameters

The effect of austenitising conditions and transformation temperature on the prior austenite grain size and pearlite interlamellar spacing of the hypoeutectoid steel (table 6.1) is similar to that observed in the eutectoid steel. Again the pearlite nodule size is seen to increase with increasing austenite grain size whilst the pearlite colony size remains fairly constant. The increase in interlamellar spacing with increasing transformation temperature is accompanied by an increase in both colony size and nodule size as observed in the eutectoid steel.

Table 6.1 shows that the volume fraction of proeutectoid ferrite ($V_\alpha$) increases with both decreasing austenitising temperature and time, and with increasing transformation temperature. The effect of austenitising conditions on $V_\alpha$ is attributed to the fact that the corresponding decrease in austenite grain size shifts the TTT curve of the steel to the left, i.e. towards decreasing transformation time. Therefore a cooling curve from the austenitising temperature to the isothermal transformation temperature has more likelihood of traversing the TTT curve in that portion where proeutectoid ferrite is formed. On the other hand, increasing the transformation temperature favours the formation of proeutectoid ferrite because the higher isotherms traverse the TTT curve in the ferrite forming area. Although the transformation condition was intended to be isothermal, transformation began before the isothermal temperature was reached so that significant transformation occured under continuous cooling conditions.

### 7.2.2 Proof stress ($\sigma_{0.2}$) and ultimate tensile stress ($\sigma_u$)

#### (i) The effect of interlamellar spacing on $\sigma_{0.2}$ and $\sigma_u$

The proof stress and ultimate tensile stress of the hypoeutectoid steel again appear to be strongly dependent on the interlamellar spacing (figure 6.8). In low carbon mild steels, the proof stress is determined by the ferrite grain size. However, in medium-high carbon steels

containing a mixture of proeutectoid ferrite and pearlite, the ferrite tends to influence the strength of the steels mainly when present as a continuous grain boundary network (Gladman et al, 1972). When such steels contain small amounts of discontinous ferrite, it appears that the pearlite interlamellar spacing is the dominant microstructural parameter controlling the proof stress.

As in the case of the eutectoid steel, the proof stress data of the hypoeutectoid steel have been plotted against the inverse square root of the ferrite mean free distance (figure 7.8a). The ferrite mean free distance $\lambda_\alpha$ was calculated using equation 4.6. This equation gives a mean free distance which is an average between the proeutectoid ferrite and the pearlitic ferrite. However, as seen in figure 7.8a, the averaging of the mfd between the two phases is not justified by the experimental results. A linear relationship is obtained between the proof stress and the inverse square root of $\lambda_\alpha$ such that the friction stress $\sigma_i$ is 400 MN/m$^2$ and the Hall-Petch constant $k_y$ is 0.12 MN/m$^{3/2}$. The value of $\sigma_i$ is significantly larger than would be expected at a testing temperature of -100 °C. In addition, $k_y$ is much smaller than the value of 0.30 MN/m$^{3/2}$ obtained in the eutectoid steel.

When a hypoeutectoid steel contains small amounts of proeutectoid ferrite as an extended phase, yielding of the less strong proeutectoid ferrite is constrained by the pearlite which has a higher yield strength. The constraint introduced by the pearlite raises the yield strength of the ferrite to a value very close to the yield strength of the pearlite. This implies that the yield strength of the hypoeutectoid steel is mainly controlled by the mean free distance in the pearlitic ferrite. Thus we observe that the proof stress of the hypoeutectoid steel at 550 MN/m$^2$ in the as-received condition (8.7 vol. % ferrite) is only slightly lower than the proof stress of the eutectoid steel at 573 MN/m$^2$. The interlamellar spacings were 0.19 and 0.21 $\mu$m respectively.

The proof stress data of the hypoeutectoid steel have been replotted against the inverse square root of the mean free distance in pearlitic ferrite ($\lambda$) in figure 7.8b. This plot gives a friction stress of about 200 MN/m$^2$ at -100 °C which agrees reasonably well with the value of 110 MN/m$^2$ at -80 °C obtained in the eutectoid steel (figure 7.3). The Hall-Petch constant of 0.22 MN/m$^{3/2}$ is however still lower than that

Figure 7.8a The dependence of the proof stress $\sigma_{0.2}$ on the inverse square root of the ferrite mean free distance ($\lambda_\alpha$) in the hypoeutectoid steel.

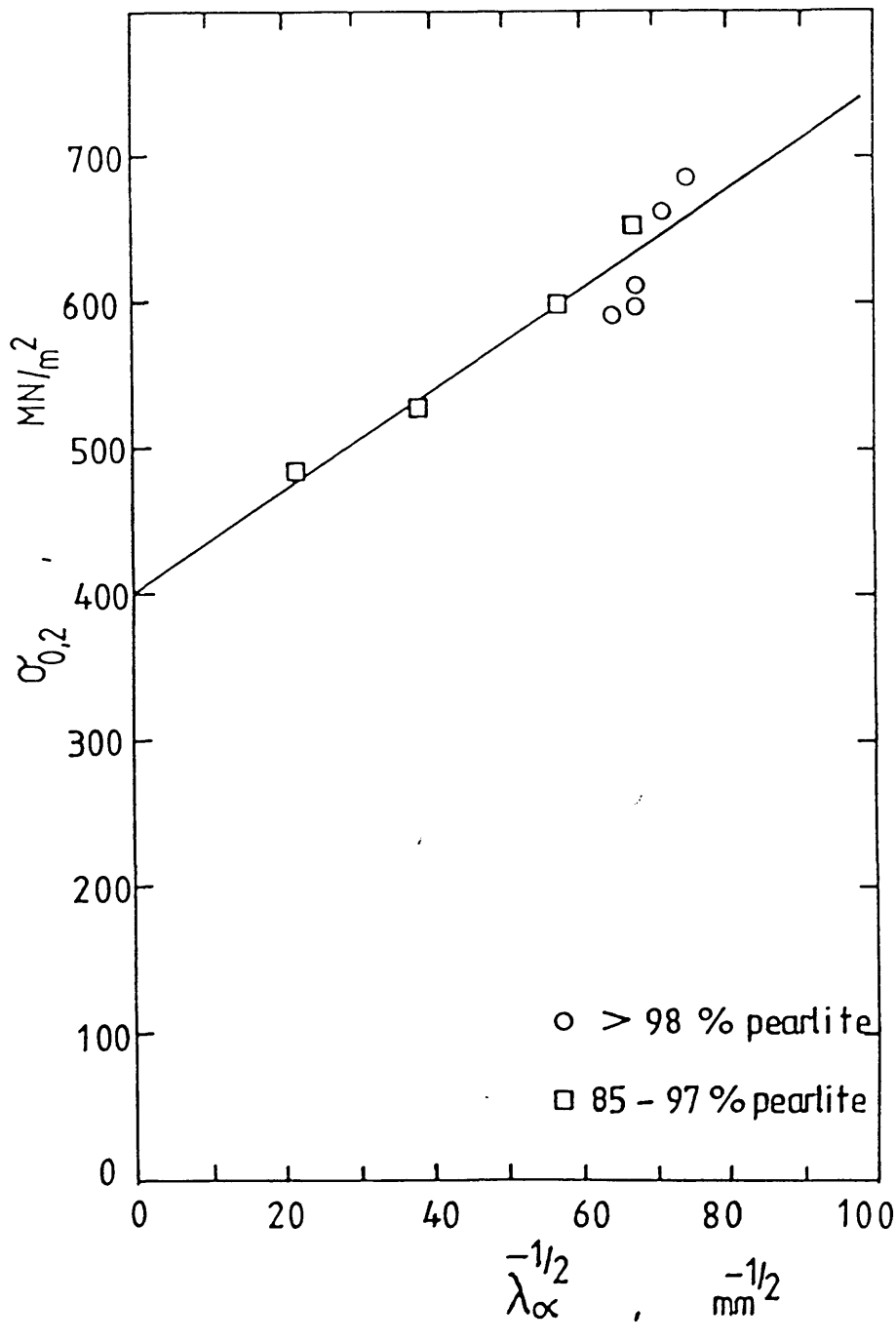
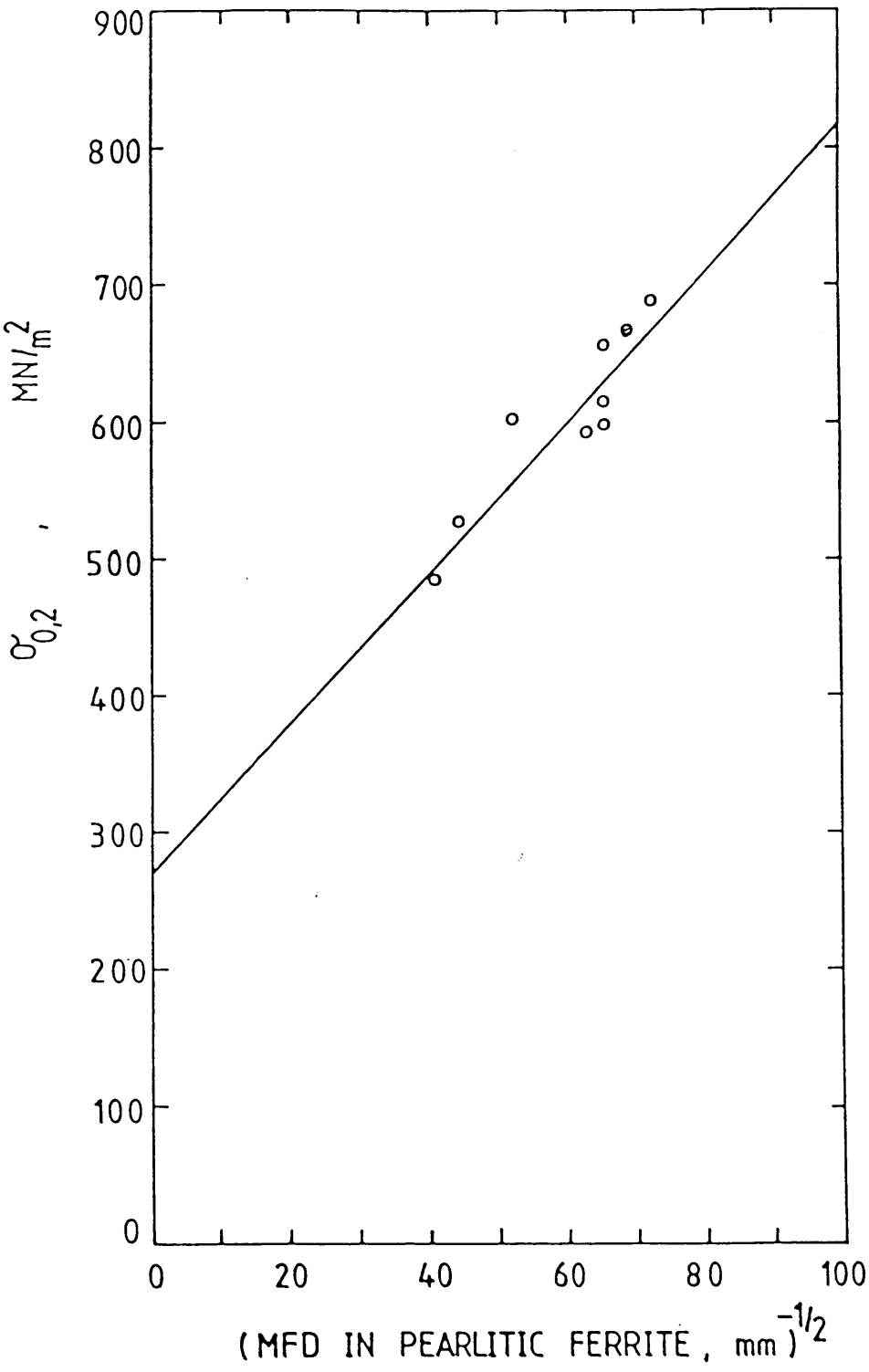


Figure 7.8b The dependence of the proof stress $\sigma_{0.2}$ of the hypoeutectoid steel on the inverse square root of the mean free distance (mfd) in pearlitic ferrite.



obtained in the eutectoid steel. Figure 7.9 shows the proof stress data of the hypoeutectoid steel from figure 7.8b and that of the eutectoid steel from figure 7.3 plotted together. A number of the data points from the hypoeutectoid steel do not lie on the line predicted by the eutectoid steel. It was thought that this behaviour was not due to the presence of the proeutectoid ferrite because some of the data points representing the high volume fractions of ferrite did lie on the line. Those points which do not fall on the line imply that the Hall-Petch constant in the hypoeutectoid steel is lower than that in the eutectoid steel if the same value of friction stress is assumed.

**(ii) The effect of austenitising conditions on proof stress and ultimate tensile stress.**

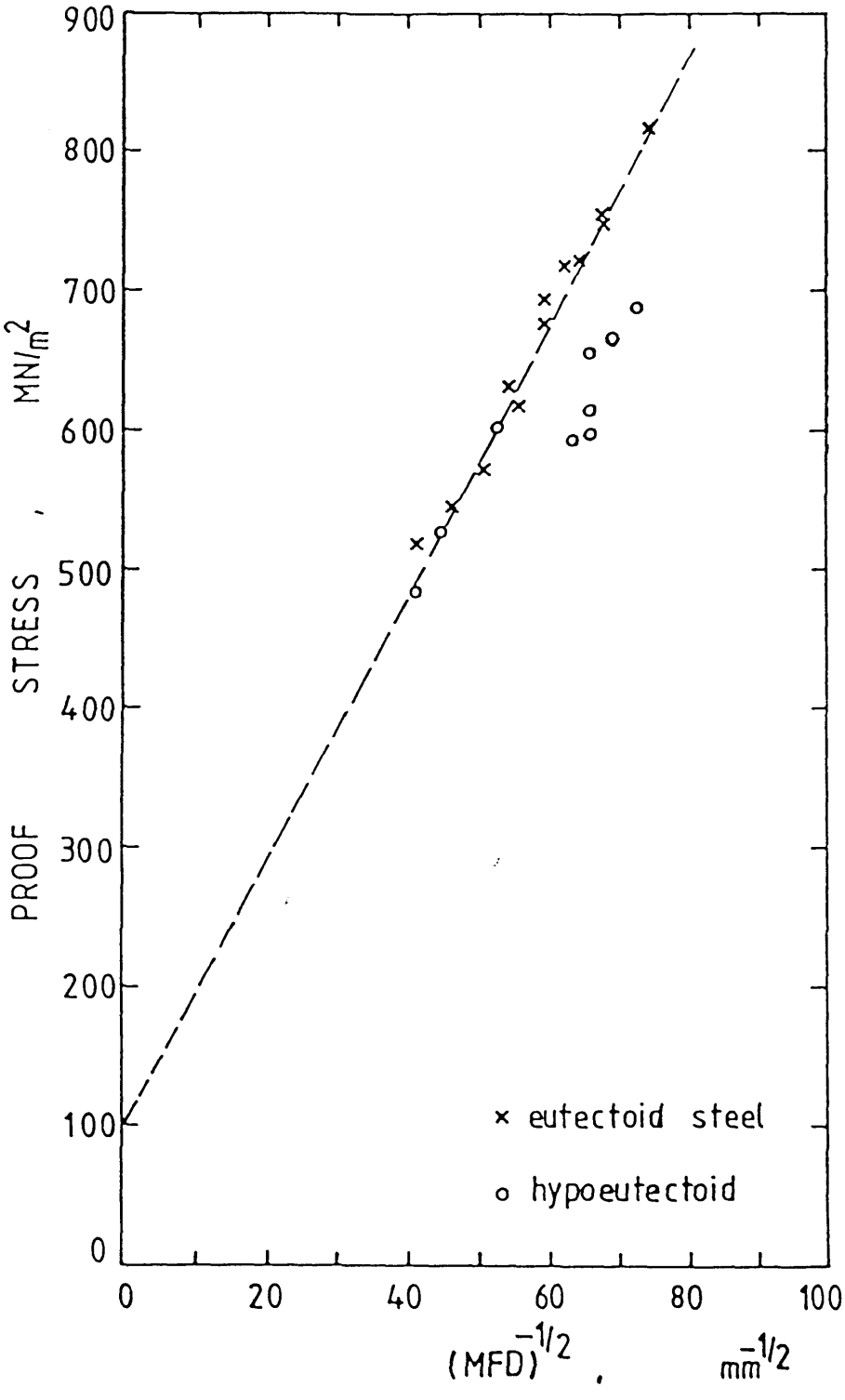
As seen in figure 6.6, the effect of austenitising conditions on the proof stress and ultimate tensile stress of the hypoeutectoid steel is similar to that of the eutectoid steel, although not as pronounced. As the austenite grain size increases, the strength increases to a peak value, then decreases, and again increases in the very coarse grain condition. This behaviour is partly attributed to the corresponding change in interlamellar spacing as the austenitising conditions were varied (table 6.1). Although the volume fraction of proeutectoid ferrite decreases from about 8 % to 1 % as the austenite grain size progressively increases, there is no obvious evidence that the proeutectoid ferrite is affecting the trend in the strength.

### 7.2.3 The cleavage fracture stress $\sigma_f$

The effect of austenitising conditions and pearlite interlamellar spacing on the cleavage fracture stress of the hypoeutectoid steel (figures 6.6 and 6.8) is similar to that in the eutectoid steel. Again the cleavage fracture stress follows the trend in the proof stress as the microstructural parameters vary.

Table 6.3 and figure 6.10 show the influence of test temperature on $\sigma_f$ and $\sigma_{0.2}$ for the coarse pearlitic microstructure. Both $\sigma_f$ and $\sigma_{0.2}$ are strongly temperature dependent and show very similar behaviour to that

Figure 7.9 The dependence of the proof stress $\sigma_{0.2}$ of the eutectoid and hypoeutectoid steels on the mean free distance (mfd) in pearlitic ferrite.



of the eutectoid steel in the coarse pearlitic condition. Figure 7.10 shows the relationship between the proof stress and the cleavage fracture stress of the hypoeutectoid steel for all test conditions. These data are similar to those of the eutectoid steel. It is of note that in the lower strength regime where the cleavage fracture stress is directly proportional to the proof stress, the constant of proportionality is about 2.25. This value is less than that of 2.4 obtained in the eutectoid steel. The $\sigma_f$ versus $\sigma_{0.2}$ data of the two steels have been plotted together in figure 7.11. It can be seen that the relationship between $\sigma_f$ and $\sigma_{0.2}$ in the two steels is essentially similar. It may be concluded therefore that the micromechanisms of cleavage fracture in the hypoeutectoid steel are similar to those proposed for the eutectoid steel.

### 7.2.4 Plane strain fracture toughness and tensile ductility

The effect of austenitising conditions on $K_{IC}$ and tensile ductility is shown in figure 6.7 where the data have been plotted against the prior austenite grain size. As in the eutectoid steel, there is little influence of $\gamma$ grain size on $K_{IC}$ although the tensile ductility decreases with increasing austenite grain size, and therefore pearlite nodule size. Table 7.3 shows the calculated values of the plastic zone size for the hypoeutectoid steel. The values are in the range 88 to 198 $\mu$m which imply that the fracture process zone in the $K_{IC}$ test ranges from about 8 to 20 $\mu$m. This is much smaller than the corresponding range of austenite grains from about 22 to 270 $\mu$m. This was the same feature of the eutectoid steel.

Figure 6.9 shows that the effect of interlamellar spacing on $K_{IC}$ and tensile ductility in the hypoeutectoid steel is similar to that in the eutectoid steel for interlamellar spacings up to about 0.27 $\mu$m. The specimen which had an interlamellar spacing of 0.31 $\mu$m (H11, table 6.1) had $K_{IC}$ values which fell short of the trend in the rest of the data. This specimen had a relatively high volume fraction of proeutectoid ferrite (15 %). Since all the other specimens had volume fractions of proeutectoid ferrite less than 8 %, the low $K_{IC}$ values for specimen H11 were attributed to the high proportion of proeutectoid ferrite.

Figure 7.10 The relationship between the proof stress $\sigma_{0.2}$ and the cleavage fracture stress $\sigma_f$ of the hypoeutectoid steel for all test conditions.

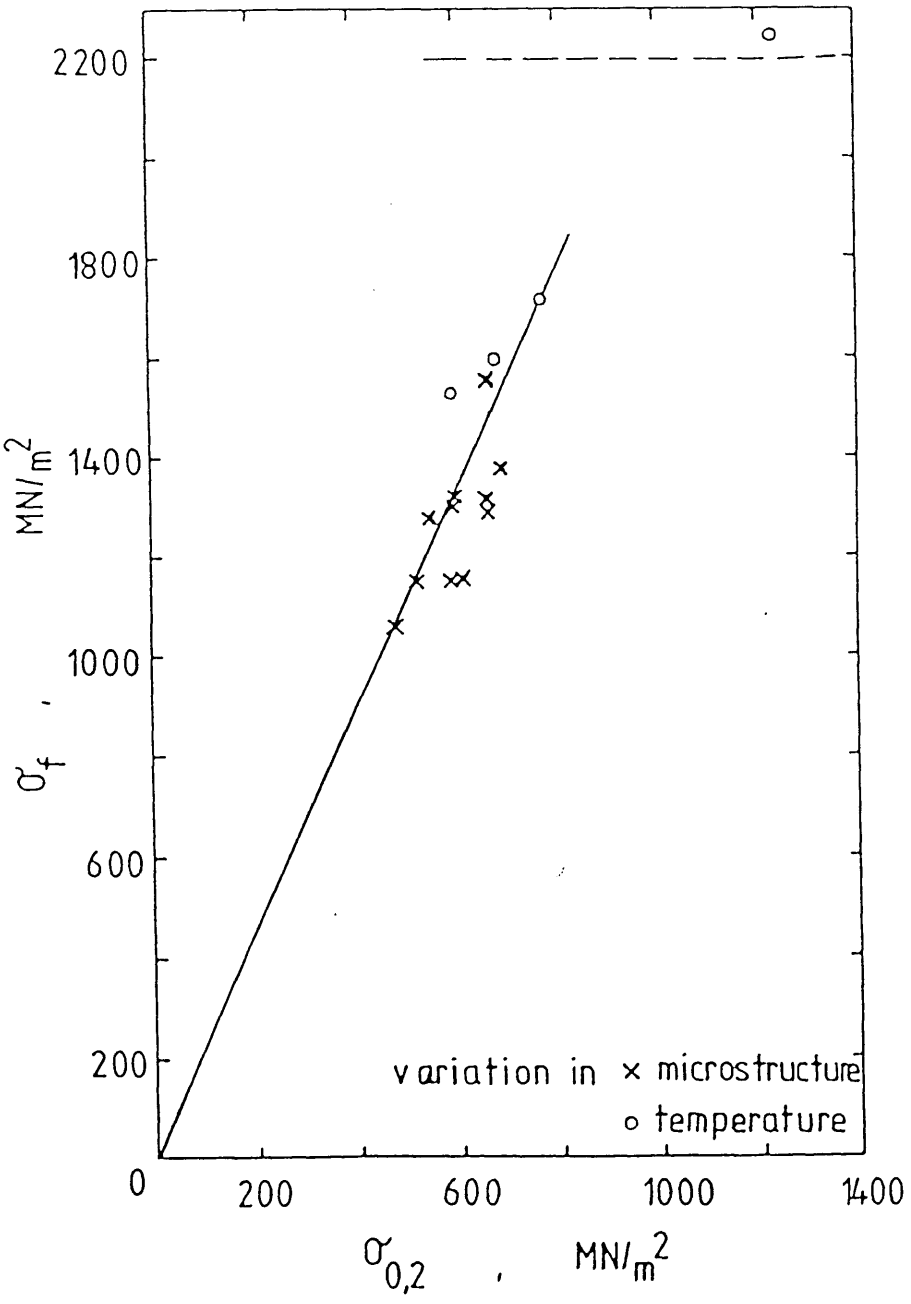


Figure 7.11 The relationship between the proof stress $\sigma_{0.2}$ and the cleavage fracture stress $\sigma_f$ in the eutectoid and hypoeutectoid steels.

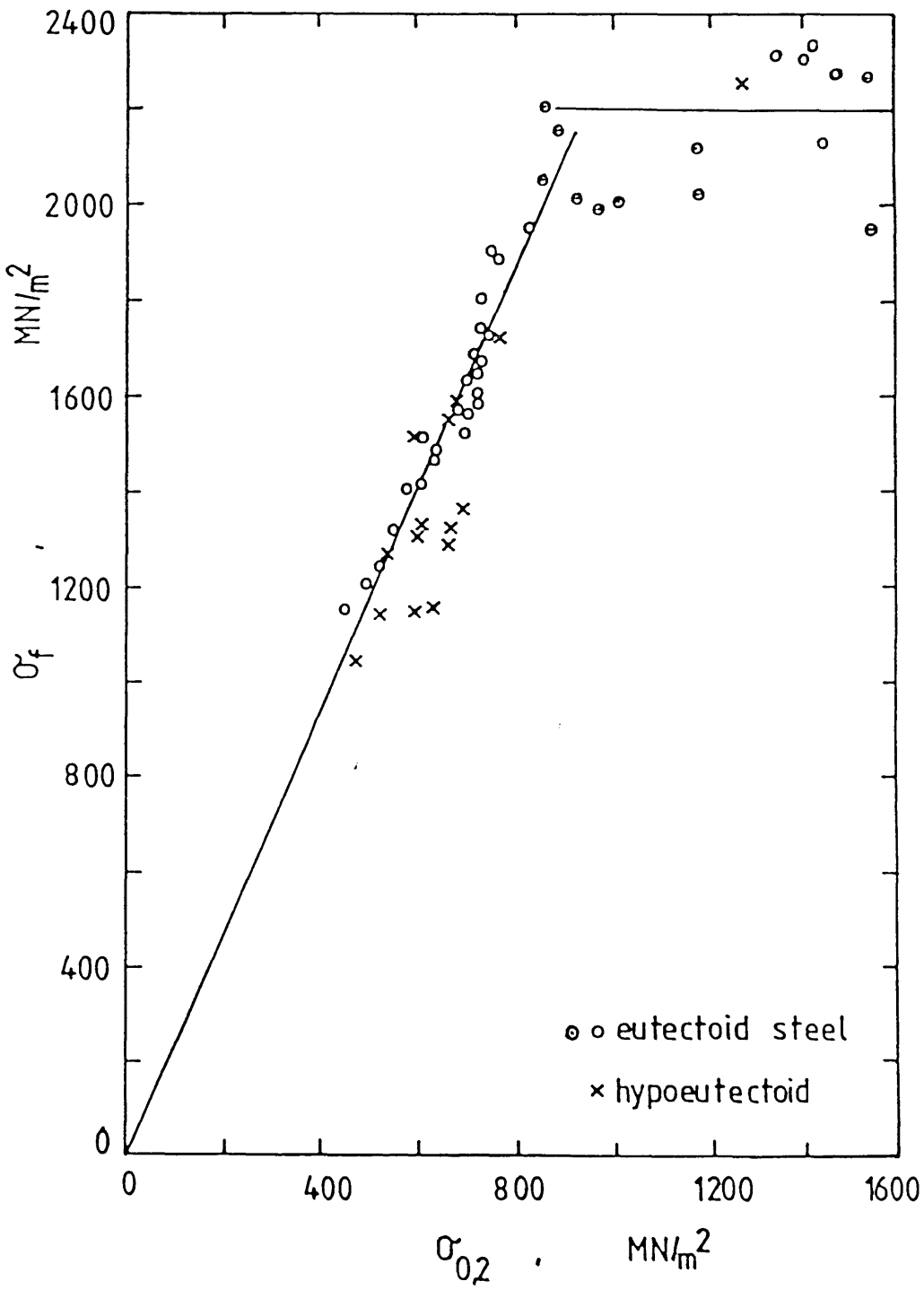


**Table 7.3 Calculated values of the plastic zone size $r_p$ and the characteristic distance for fracture X in the hypoeutectoid steel**

| Specimen | $\sigma_{0.2}$ MN/m$^2$ | $K_{IC}$ MN/m$^{3/2}$ | $\gamma$ μm | N μm | $\frac{\sigma_f}{\sigma_{0.2}}$ | $r_p$ μm | X μm |
|---|---|---|---|---|---|---|---|
| H1 | 666 | 28.6 | 21.8 | 14 | 1.93 | 97.8 | 111 |
| H2 | 666 | 29.4 | 36.4 | 20 | 1.97 | 103.4 | 116 |
| H3 | 689 | 29.0 | 76.6 | 28 | 2.00 | 94.0 | 91 |
| H4 | 667 | 27.2 | 90.0 | 40 | 2.25 | 88.2 | 67 |
| H5 | 599 | 25.7 | 166.7 | 56 | 2.18 | 97.7 | 83 |
| H6 | 593 | 26.4 | 195.7 | 80 | 1.94 | 105.1 | 119 |
| H7 | 613 | 31.2 | 271.0 | 113 | 1.89 | 137.4 | 181 |
| H8 | 667 | 27.2 | 90.0 | 40 | 2.25 | 88.2 | 67 |
| H9 | 601 | 24.9 | 88.2 | 56 | 2.20 | 91.1 | 72 |
| H10 | 527 | 32.2 | 87.6 | 68 | 2.19 | 198.1 | 160 |
| H11 | 485 | 25.2 | 82.9 | 80 | 2.18 | 143.2 | 118 |

# 8. CONCLUSIONS AND RECOMMENDATIONS

## 8.1 Conclusions drawn from the present research

1. The proof stress, ultimate tensile strength and cleavage fracture stress of pearlitic steels increase with decreasing interlamellar spacing.

2. The proof stress of pearlitic steels is related to the ferrite mean free distance by the Hall-Petch equation.

3. No simple relationship exists between the prior austenite grain size and either tensile strength or cleavage fracture stress.

4. The proof stress and cleavage fracture stress show similar microstructural dependence.

5. In coarse pearlite the cleavage fracture stress increases with decreasing test temperature. In fine pearlite the cleavage fracture stress is temperature independent.

6. The micromechanisms of cleavage fracture in pearlitic steels are dependent on the strength of the steels.

7. In lower strength pearlite ($\sigma_f \lesssim 2100$ MN/m$^2$), the cleavage fracture stress is proportional to the proof stress. Cleavage fracture is nucleation-controlled and involves the nucleation of a microcrack by shear-stress-controlled fibrous cracking of the pearlite. The microcrack extends to a critical size due to the failure of successive ferrite and cementite lamellae

8. In higher strength pearlite ($\sigma_f \gtrsim 2100$ MN/m$^2$), cleavage fracture is propagation-controlled. The available stress is sufficient to cause unstable propagation once a carbide microcrack is nucleated. The crack nucleus is formed by fibre-loading of the cementite lamellae, and is probably an array of carbide microcracks which form simultaneously prior to propagation.

9. The effect of prior austenite grain size on the plane strain fracture toughness $K_{IC}$ is very small in pearlitic steels. The fracture process zone in a $K_{IC}$ test is much smaller than the austenite grain size, and as such the grain boundaries are unlikely to influence the fracture process.

10. The change in the micromechanism of cleavage fracture over the range of pearlitic spacings studied is reflected in the $K_{IC}$ values. In the eutectoid steel, $K_{IC}$ first decreases, and then increases as the interlamellar spacing decreases. The hypoeutectoid steel follows the same trend as that of the eutectoid steel for volume fractions of proeutectoid ferrite less than about 10 %.

11. The tensile ductility decreases progressively as the austenite grain size, and therefore the pearlite nodule size increases. The tensile ductility represents the strain necessary to develop a nodule-size microcrack which initiates unstable cleavage fracture propagation in the tensile test.

12. The heat treatment for optimum strength and fracture toughness in these steels appears to be an austenitising (finishing) temperature of 900 °C followed by fast cooling to produce the finest pearlite spacings possible, typically about 0.1 $\mu$m. This corresponds to an isothermal transformation temperature no higher than 550 °C.

## 8.2 Recommendations

(i) The present research has demonstrated that the micromechanisms of cleavage fracture in pearlitic steels are different from those in low carbon mild steels. It is recommended that the micromechanisms of cleavage fracture in plain carbon steels with carbon contents from about 0.3 to 0.6 % be investigated since little is known about the cleavage behaviour of these steels.

(ii) Since a transition from propagation-controlled to nucleation-controlled cleavage fracture is observed as one changes from mild steels to pearlitic steels, it should be of interest to establish the carbon content at which the transition occurs.

(ii) Although the cleavage behaviour of lath microstructures like bainite and martensite has been studied by a number of workers, there is as yet no clear understanding of the micromechanism of cleavage fracture. It is suggested that further studies be made to investigate the micromechanisms of fracture in these structures in the light of the mechanisms proposed for pearlite. It is likely that there will be similarities in the cleavage behaviour of these microstructures since the morphology of carbides in lath microstructures has similarities to that in lamellar pearlite.

(iv) Since the mode of cleavage fracture in pearlitic steels depends on strength, it is suggested that the effect of strengthening the proeutectoid ferrite on the mode of fracture be investigated. It is likely that a transition in the mode of fracture will occur at coarser pearlitic spacings when the ferrite is strengthened.

# R E F E R E N C E S

Alexander D. J. and Bernstein I. M. (1982), Metall. Trans., Vol. 13A, P. 1865.

Asundi M. K. and West D. R. F. (1966), J.Inst. Metals, Vol 94, P.19.

Bouse G. K., Bernstein I.M. and Stone D. H. (1978), ASTM STP 644, P.145, (Ed. by D. H. Stone and G. G. Knupp), Philadelphia, PA.

Bowen P. (1985), PhD Thesis, University of Cambridge.

Bowen P. and Knott J. F. (1984) Metal Science, Vol. 18, P.225.

Brown D. and Ridley N. (1966), J. Iron and Steel Institute, (August), P.811.

Cottrell A. H. (1958), Trans. AIME, Vol. 212, P.192.

Curry D. A. and Knott J.F. (1978), Metal Science, (November), P.511.

Curry D. A. and Knott J. F. (1979) Metal Science, (June), P.341.

Curry D. A. (1980), Metal Science, (Aug-Sept), P.319.

Curry D. A. (1984), Metal Science, Vol 18, P.67.

Dippenaar R. J. and Honeycombe R. W. K. (1973), Proc. Roy. Soc. London, Vol. A333, P.455.

Gensamer et al. (1942), Trans. ASM, Vol 30, P.983.

Gensamer M., Pearsal E. B., Pellini W. S. and Low (Jr) J. R. (1942), Trans ASM, Vol 30, P. 983.

Gladman T., McIvor I. D. and Pickering F. B. (1972), J. Iron and Steel Institute, Vol.210, Part 12, P. 916.

Goods S. H. and Brown L. M. (1979), Acta Metall., Vol. 27, P.1.

Grange R. A. (1971), Metall. Trans. Vol. 2, P.65.

Gray III G. T., Thompson A. W., Williams J. C., and Stone D. H. (1982), Canadian Metallurgical Quarterly, Vol. 21, No.1, P.73.

Griffiths J. R. and Owen D. R. J. (1971), J. Mech. Phys. Solids, Vol. 19, P.419.

Hahn G. T. (1984) Metall. Trans. A, Vol 15A, (June) P.947.

Hahn G. T. and Rosenfield A. (1975), Mettal. Trans., Vol 6A, P.653.

Harrison J.D. (1980), Metal Construction, (November), P.600

Honeycombe R. W. K. (1981), Steels, Microstructure and Properties, Edward Arnold Publs., London.

Hyzak J. M. and Berstein I. M. (1976), Metall. Trans., Vol. 7A, P.1217.

Kamada A., Koshizuka N. and Funakoshi T. (1976), Trans Iron and Steel Inst. of Japan, Vol. 16, P407.

Karlson B. and Linden G. (1975), Materials Science and Engineering, Vol. 17, P 153.

Kennon N. F. and Kaye N. A. (1982), Metall. Trans. A, Vol 13A, (June) P.975.

Kennon N. F. (1978), Metall. Trans. A, Vol. 9A, (January), P.57.

Knott J. F. (1976), Mechanics and Physics of Fracture, Metals Society, London.

Knott J. F. (1973), Fundamentals of Fracture Mechanics, Butterworths, London.

Knott J. F. (1977), Fracture 1977, Vol.1 ICF 4, Waterloo, P.61.

Knott J. F. (1966), J. Iron and Steel Inst., Vol. 204, P.104.

Knott J. F. (1980), Metal Science, (Aug-Sept), P.327.

Knupp G. G., Chidley W. H., Grove J. L., Hartman H. H., Morris G. F. and Taylor C. W. (1978), ASTM STP 644, P.7, (Ed. by D. H. Stone and G. G. Knupp), Philadelphia, PA.

Kotilainen H. (1982), In Proc. 4th European Conf. on Fracture, (Ed. K. L. Maurer and F. E. Metzer), Vol. 1, P255.

Kotilainen H., Torronen K. and Neonen P. (1982), Advances in Fracture Research, (Ed. D.Francois), Pergamon Press, Vol. 2, P.723.

Langford G. (1977), Mettal. Trans., Vol. 8A, P.861.

Lewandowski J. J. and Thompson A. W. (1984), Proc. 6th Int. Conf. on Fracture, New Delhi, (Ed. by S. R. Valluri et. al.), P.1515.

Lindbourg U. (1968), Trans. ASM, Vol. 61, P.500.

Lindley T. C., Oates G. and Richards C. E. (1970), Acta. Metall., Vol. 18, P.1127.

Low J. R. (1954), Symp. On Relation of Properties to Microstructure, Trans. ASM, Vol. 46A, P.163.

Marder A. R. and Bramfitt B. L. (1975), Mettal. Trans., Vol. 6A, P.2009.

Marder A. R. and Bramfitt B. L. (1976), Mettal. Trans., Vol. 7A, P.365.

Mehl R. F. and Hagel W. C. (1956), Prog. Met. Phys., Vol.6, P.74.

Miller L. E. and Smith G. C. (1970), J. Iron and Steel Inst., Vol.208, P.998

Naylor J. P. (1979), Metall. Trans., Vol. 10A, P.861.

O'Donnelly B. E., Reuben R. L. and Baker T. N. (1984), Metals Technology, Vol.11, (Feb.), P.45.

Oates G. (1969), J. Iron and Steel Inst., Vol. 207, P.353.

Park Y. J. and Berstein I. M. (1978), ASTM STP 644, P. 287, (Ed. by D. H. Stone and G. G. Knupp), Philadelphia, PA.

Park Y.J. and Berstein I.M.(1979), Metall. Trans., Vol.10A, P. 1653.

Pickering F. B. (1978), Physical Metallurgy and the Design of Steels, London, Applied Science Publs. Ltd.

Porter D., Easterling K. and Smith G. (1978), Acta Metall., Vol. 26, P.1405.

Preston R. R. (1980), Wear Resistant Materials in the Steel Industry, The Metallurgist and Materials Technologist, (Dec.), P.687.

Puls M. P. and Kirkaldy J. S. (1972), Metall. Trans., Vol.3, P.2777.

Rathenau G. W. and Baas G. (1954), Acta Met., Vol. 2, P.875.

Rice J. R. and Johnson M. A. (1970), in "Inelastic behaviour of solids", ed. by M.F. Kanninen et al, McGraw-Hill, N.Y., P.641-672.

Rice J. R. and Tracey D. M. (1969), J. Mech. Phys. Solids, Vol. 17, P.201.

Ridley N. (1984), Metall. Trans. A, Vol. 15A, (June), P.1019.

Ritchie R. O., Knott J. F. and Rice J. R. (1973), J. Mech. Phys. Solids, Vol. 21, P.395.

Roberts M. J. (1970), Metall. Trans., Vol. 1, P.3287.

Roosz A. and Gacsi Z. (1981), Metallography 14, P.129.

Roosz A., Gacsi Z. and Baan M. K. (1980), Metallography 13, P.299.

Smith E. (1966), Proc. Conf. Physical Basis of Yield and Fracture, P.36, Inst. Phys. and Phys. Soc., Oxford.

Smith C. S. (1953), Trans ASM, Vol. 45, P.533.

Stroh A. N. (1954), Proc. Roy. Soc., Vol.A 223, P.404.

Takahashi T. and Nagumo M. (1970), Trans. Japan Inst. of Metals, Vol. 11, P.113.

Tetelman A. S. and McEvily Jr. A. J. (1967), Fracture of Structural Materials, John Wiley and Sons, New York.

Tomita Y. and Okabayashi K. (1985), Mettal. Trans., Vol. 16A, P.73.

Underwood E. E. (1970), Quantitative Steriology, Addison-Wesley Publ. Co., Reading, Massachusetts, P.73.

Vander Voort G. F. and Roosz A. (1984), Metallography, Vol. 17, P.1.

Wallin K. Saario T. and Torronen K. (1984), Metal Science, Vol. 18, P.13.

Young J. D. (1978), ASTM STP 644, P.256, (Ed. by D. H. Stone and G. G. Knupp), Philadelphia, PA.

Zener C. (1946), Trans AIME, Vol. 167, P.550.

Zener C. (1948), Trans ASM, Vol. 40A, P.3.

# APPENDIX 1

VALUES OF $Y$ AGAINST $a/W$ FOR BEND TEST PIECE THREE-POINT LOADED OVERALL SPAN TO TEST PIECE WIDTH RATIO 4 : 1

| $a/W$ | $Y$ stress intensity coefficient | | | | |
|---|---|---|---|---|---|
| | 0.0000 | 0.002 | 0.004 | 0.006 | 0.008 |
| 0.260 | 5.34 | 5.37 | 5.39 | 5.42 | 5.45 |
| 0.260 | 5.48 | 5.51 | 5.54 | 5.56 | 5.59 |
| 0.270 | 5.62 | 5.65 | 5.68 | 5.71 | 5.74 |
| 0.280 | 5.77 | 5.80 | 5.83 | 5.86 | 5.89 |
| 0.290 | 5.92 | 5.95 | 5.98 | 6.01 | 6.04 |
| 0.300 | 6.07 | 6.10 | 6.13 | 6.17 | 6.20 |
| 0.310 | 6.23 | 6.26 | 6.29 | 6.33 | 6.36 |
| 0.320 | 6.39 | 6.42 | 6.46 | 6.49 | 6.52 |
| 0.330 | 6.56 | 6.59 | 6.63 | 6.66 | 6.70 |
| 0.340 | 6.73 | 6.77 | 6.80 | 6.84 | 6.87 |
| 0.350 | 6.91 | 6.94 | 6.98 | 7.02 | 7.05 |
| 0.360 | 7.09 | 7.13 | 7.12 | 7.20 | 7.24 |
| 0.370 | 7.28 | 7.32 | 7.36 | 7.40 | 7.44 |
| 0.380 | 7.48 | 7.52 | 6.56 | 7.60 | 7.64 |
| 0.390 | 7.68 | 7.72 | 7.77 | 7.81 | 7.85 |
| 0.400 | 7.89 | 7.94 | 7.98 | 8.03 | 8.07 |
| 0.410 | 8.11 | 8.16 | 8.21 | 8.25 | 8.30 |
| 0.420 | 8.35 | 8.39 | 8.44 | 8.49 | 8.54 |
| 0.430 | 8.59 | 8.63 | 8.68 | 8.73 | 8.79 |
| 0.440 | 8.84 | 8.89 | 8.94 | 8.99 | 9.05 |
| 0.450 | 9.10 | 9.15 | 9.21 | 9.26 | 9.32 |
| 0.460 | 9.37 | 9.43 | 9.49 | 9.54 | 9.60 |
| 0.470 | 9.66 | 9.72 | 9.78 | 9.81 | 9.90 |
| 0.480 | 9.96 | 10.03 | 10.09 | 10.15 | 10.22 |
| 0.490 | 10.28 | 10.34 | 10.41 | 10.48 | 10.54 |
| 0.500 | 10.61 | 10.68 | 10.75 | 10.82 | 10.89 |
| 0.510 | 10.96 | 11.03 | 11.11 | 11.18 | 11.25 |
| 0.520 | 11.33 | 11.40 | 11.48 | 11.56 | 11.64 |
| 0.530 | 11.71 | 11.79 | 11.87 | 11.96 | 12.04 |
| 0.540 | 12.12 | 12.20 | 12.29 | 12.37 | 12.46 |
| 0.550 | 12.55 | | | | |

# A P P E N D I X 2

## AN EXPRESSION FOR FRACTURE TOUGHNESS $K_Q$ OF FOUR POINT BEND SPECIMENS WITH L = 2W

F. P. L. KAVISHE

Department of Metallurgy & Materials Science, Imperial College, Prince Consort Road, London SW7 2BP, U.K.

In his recent paper, Fu Dong[1] gave an expression for $K_Q$ of four point bend specimens in the form

$$K_Q B(W)^{3/2}/M = 0.8\sqrt{(a/W)} + 4f(a/W) \qquad (1)$$

and tabulated values of the left hand quantity against a/W. In this paper a simplified expression for $K_Q$ is given in a form similar to that given for the case of three point bending in BS 5447:1977, where for L = 2W,

$$K_Q = \frac{P_Q Y_1}{BW^{\frac{1}{2}}} \qquad (2)$$

Here $P_Q$ is the force, B the specimen thickness, W the width, L half the loading span, and $Y_1$ is a function of a/W given in Table 3 of the above named British standard.

We start by considering a bar subjected to a bending moment M due to some applied stress σ. The bar has a sharp notch of length a, its width is W and its thickness is B (Fig. 1). M and σ are related by

$$\frac{M}{I} = \frac{\sigma}{y} \qquad (3)$$

where the second moment of area I is given by $\frac{1}{12} BW^3$ and where $y = \frac{1}{2}W$.

The stress is therefore given as

$$\sigma = \frac{M.y}{I} = \frac{6M}{BW^2} \qquad (4)$$

The stress intensity factor at the root of the notch is given by $K_o = \sigma\sqrt{\pi a}$, so that

$$K_o = \frac{6M\sqrt{\pi a}}{BW^2} \qquad (5a)$$

Here $M = \frac{P}{2}\cdot W$, where P is the applied force (Fig.2).

$$\text{Thus } K_o = \frac{3P\sqrt{\pi a}}{BW} = \frac{3P\sqrt{\pi}\sqrt{(a/W)}}{B\sqrt{W}} \qquad (5b)$$

Brown and Strawley[2] have given an expression for the stress intensity factor $K_I$ in mode I opening for four point bending as:

$$\frac{K_I}{K_o} = 1.12 - 1.39\,(a/W) + 7.32\,(a/w)^2 - 13.1\,(a/w)^3 + 14.0\,(a/w)^4 \qquad (6)$$

where $a/w \leq 0.6$.

Substituting for $K_o$,

$$K_I = \frac{3P\sqrt{\pi}\sqrt{(a/W)}}{B\sqrt{W}}\,[1.12 - 1.39(a/w) + 7.32(a/w)^2 - 13.1(a/w)^3 + 14.0(a/w)^4]$$

$$= \frac{P}{BW^{\frac{1}{2}}}\,[5.96(a/w)^{\frac{1}{2}} - 7.39(a/w)^{3/2} + 38.92(a/w)^{5/2} - 69.66(a/w)^{7/2} + 74.44(a/w)^{9/2}] \qquad (7)$$

Since the expression in square brackets is a constant for a given value of a/w, it is here referred to as Y. It then follows:

$$K_I = \frac{PY}{BW^{\frac{1}{2}}} \qquad \text{where} \quad Y = f(a/w).$$

Using the normal notation for the provisional value of fracture toughness,

$$K_Q = \frac{P_Q Y}{BW^{\frac{1}{2}}} \tag{8}$$

Values of the compliance Y are given against a/w in Table 1 for the range $0.3 \leq a/w \leq 0.6$. Both equations (1) and (8) should basically produce the same results.

The author would like to thank Dr T J Baker for his useful discussions.

References

1. Fu Dong, International Journal of Fracture, 24 (1984), R107-R108.
2. W. F. Brown Jr., and J. E. Strawley, Plane Strain Crack Toughness Testing of High Strength Metallic Materials, STP 410, American Society for Testing and Materials, Philadelphia (1966).

FIGURE 1 A notched bar in bending

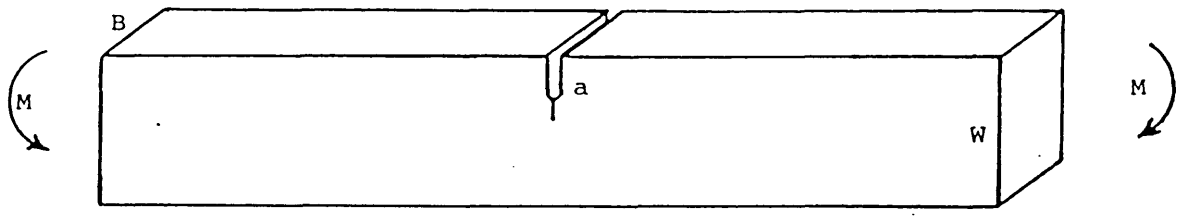



FIGURE 2 Loading geometry considered

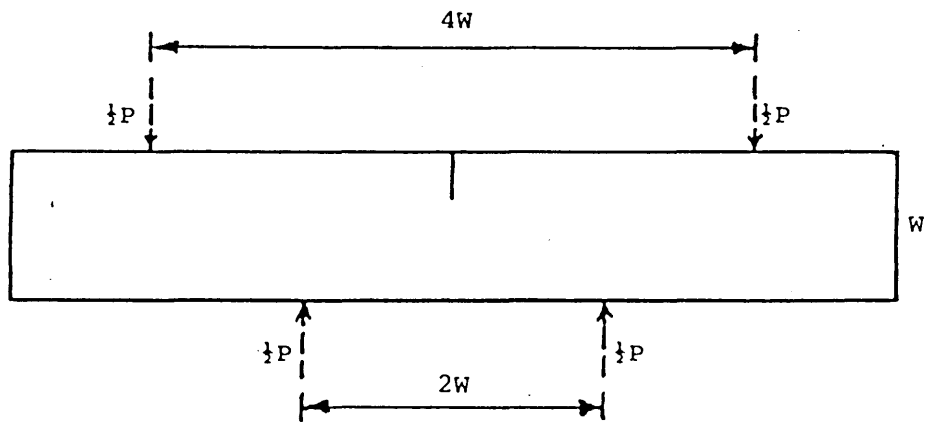


TABLE 1 - VALUES OF Y AGAINST a/W FOR FOUR-POINT BENDING WHERE HALF-LOADING SPAN, L = 2W

| a/W | .000 | .001 | .002 | .003 | .004 | .005 | .006 | .007 | .008 | .009 |
|---|---|---|---|---|---|---|---|---|---|---|
| .30 | 3.28 | 3.28 | 3.29 | 3.30 | 3.31 | 3.32 | 3.33 | 3.33 | 3.34 | 3.35 |
| .31 | 3.36 | 3.37 | 3.38 | 3.38 | 3.39 | 3.40 | 3.41 | 3.42 | 3.43 | 3.44 |
| .32 | 3.45 | 3.45 | 3.46 | 3.47 | 3.48 | 3.49 | 3.50 | 3.51 | 3.52 | 3.52 |
| .33 | 3.53 | 3.54 | 3.55 | 3.56 | 3.57 | 3.58 | 3.59 | 3.60 | 3.61 | 3.62 |
| .34 | 3.62 | 3.63 | 3.64 | 3.65 | 3.66 | 3.67 | 3.68 | 3.69 | 3.70 | 3.71 |
| .35 | 3.72 | 3.73 | 3.74 | 3.75 | 3.76 | 3.77 | 3.77 | 3.78 | 3.79 | 3.80 |
| .36 | 3.81 | 3.82 | 3.83 | 3.84 | 3.85 | 3.86 | 3.87 | 3.88 | 3.89 | 3.90 |
| .37 | 3.91 | 3.92 | 3.93 | 3.94 | 3.95 | 3.96 | 3.97 | 3.98 | 3.99 | 4.00 |
| .38 | 4.02 | 4.03 | 4.04 | 4.05 | 4.06 | 4.07 | 4.08 | 4.09 | 4.10 | 4.11 |
| .39 | 4.12 | 4.13 | 4.14 | 4.15 | 4.17 | 4.18 | 4.19 | 4.20 | 4.21 | 4.22 |
| .40 | 4.23 | 4.24 | 4.25 | 4.27 | 4.28 | 4.29 | 4.30 | 4.31 | 4.32 | 4.33 |
| .41 | 4.35 | 4.36 | 4.37 | 4.38 | 4.39 | 4.40 | 4.42 | 4.43 | 4.44 | 4.45 |
| .42 | 4.46 | 4.48 | 4.49 | 4.50 | 4.51 | 4.53 | 4.54 | 4.55 | 4.56 | 4.58 |
| .43 | 4.59 | 4.60 | 4.61 | 4.63 | 4.64 | 4.65 | 4.67 | 4.68 | 4.69 | 4.70 |
| .44 | 4.72 | 4.73 | 4.74 | 4.76 | 4.77 | 4.78 | 4.80 | 4.81 | 4.82 | 4.84 |
| .45 | 4.85 | 4.87 | 4.88 | 4.89 | 4.91 | 4.92 | 4.94 | 4.95 | 4.96 | 4.98 |
| .46 | 4.99 | 5.01 | 5.02 | 5.04 | 5.05 | 5.06 | 5.08 | 5.09 | 5.11 | 5.12 |
| .47 | 5.14 | 5.15 | 5.17 | 5.18 | 5.20 | 5.22 | 5.23 | 5.25 | 5.26 | 5.28 |
| .48 | 5.29 | 5.31 | 5.32 | 5.34 | 5.36 | 5.37 | 5.39 | 5.40 | 5.42 | 5.44 |
| .49 | 5.45 | 5.47 | 5.49 | 5.50 | 5.52 | 5.54 | 5.55 | 5.57 | 5.59 | 5.61 |
| .50 | 5.62 | 5.64 | 5.66 | 5.68 | 5.69 | 5.71 | 5.73 | 5.75 | 5.76 | 5.78 |
| .51 | 5.80 | 5.82 | 5.84 | 5.85 | 5.87 | 5.89 | 5.91 | 5.93 | 5.95 | 5.97 |
| .52 | 5.99 | 6.00 | 6.02 | 6.04 | 6.06 | 6.08 | 6.10 | 6.12 | 6.14 | 6.16 |
| .53 | 6.18 | 6.20 | 6.22 | 6.24 | 6.26 | 6.28 | 6.30 | 6.32 | 6.34 | 6.37 |
| .54 | 6.39 | 6.41 | 6.43 | 6.45 | 6.47 | 6.49 | 6.51 | 6.54 | 6.56 | 6.58 |
| .55 | 6.60 | 6.62 | 6.65 | 6.67 | 6.69 | 6.71 | 6.74 | 6.76 | 6.78 | 6.81 |
| .56 | 6.83 | 6.85 | 6.88 | 6.90 | 6.92 | 6.95 | 6.97 | 6.99 | 7.02 | 7.04 |
| .57 | 7.07 | 7.09 | 7.12 | 7.14 | 7.17 | 7.19 | 7.22 | 7.24 | 7.27 | 7.29 |
| .58 | 7.32 | 7.34 | 7.37 | 7.40 | 7.42 | 7.45 | 7.48 | 7.50 | 7.53 | 7.56 |
| .59 | 7.58 | 7.61 | 7.64 | 7.67 | 7.69 | 7.72 | 7.75 | 7.78 | 7.80 | 7.83 |
| .60 | 7.86 | | | | | | | | | |